Study on Coulomb explosion induced by laser-matter interaction and application to ion acceleration

Benedetta Peiretti Paradisi
* * * * * *

Supervisor
Prof. Gianni COPPA., Politecnico di Torino, Supervisor

Doctoral Examination Committee:

Prof. Antonio D'ANGOLA, Università degli Studi della Basilicata
Prof. Gianni LAPENTA, Katholieke Universiteit Leuven
Prof. Renato ORTA, Politecnico di Torino
Prof. Paolo RICCI, Ecole Polytechnique Federale Lausanne
Prof. Lamberto RONDONI, Politecnico di Torino

Politecnico di Torino
2019

I hereby declare that, the contents and organisation of this dissertation constitute my own original work and does not compromise in any way the rights of third parties, including those relating to the security of personal data.

………………………….....
Benedetta Peiretti Paradisi
Torino, 2019

Abstract

Recent studies on laser-matter interaction have been demonstrated the possibility to expel all the electrons, leaving an ion cloud which can expand due to the Coulomb explosion phenomenon. In order to exploit this mechanism in different fields as hadron-therapy or fusion research, the quality and the small spread of energy of the ion beam spectrum are essential. However, to achieve properly peak energy of the ions, different laser targets can be tested, changing their geometry and composition. In this thesis, two different type of targets have been examined: spherical nano-clusters or cylindrical targets, composed by one or two ion species. In case of spherical symmetry a semi-analytical model is presented, to describe the dynamics of an expanding heterogeneous cluster, coupled with a numerical model, the so-called shell method, useful when the hypothesis of the theoretical model are not still valid. In order to describe cylindrical targets three different numerical models were developed:

1. the Soft-Spheres method, a $3D$ N-Body algorithm, without hypothesis on the symmetry of the system

2. the EXPICYL method, a $2D$ axial symmetric PIC code, without a fixed computational grid to follow properly expansion phenomena

3. the ring method, a gridless $2D$ model, where the computational particle is schematized as a circular torus.

All the numerical models were validated in referring geometries, generally where the analytical comparison is available. Several different configurations were tested, varying the characteristic parameters of heterogeneous mixtures, as the fraction of the two species on the total and the mass-to-charge ratio of the ions, or the initial density distribution of the ions, with the aim of finding the suitable conditions for the hardening of the energy spectrum and the increase of the energy peak. In future, it could be interesting a more accurate study on the quality of the ion beams in terms of efficiency of the acceleration mechanism and stability, tailored for the demanded applications.

Contents

Chapter 1

Introduction

Intense laser pulses interacting with matter may induce the formation of plasma and a consequent rapid expansion into the vacuum, as studied since 1962 by J. Dawson (Dawson, 1962). Depending on different laser and target characteristics, a lot of phenomena could take place, starting from a quasi-neutral plasma expansion (Krainov and Roshchupkin, 2001) or reaching the Coulomb explosion condition (Boella et al., 2016; Peano et al., 2006). In case of very intense laser pulses (pulse $t < 1$ ps and intensity $I > 10^{16}$ W/cm^2), the energy driven on the matter is sufficient to expel all the electrons from their respective atoms, leaving behind an ion cloud lacking of all the inter-molecular chemical bonds, and quite instantly the strong positive force between the ions induces a rapid explosion at high velocities (Ditmire et al., 1996). This process of acceleration is a well known phenomenon called Coulomb explosion (Ditmire et al., 1997), with many potential applications ranging from fusion research (Last and Jortner, 2001a; Ditmire et al., 1999) to biomolecular imaging (Neutze et al., 2000) and hadron therapy in oncology (Karsch et al., 2017; Bulanov et al., 2009, 2002), depending on the energies reached by the ions of the target. The study of the Coulomb explosion mechanism is relatively simple when the time scales of the ionization processes are some order of magnitude shorter than the time scale of the expansion: the conditions of the so-called cluster vertical ionization (CVI) are verified. Typically, the CVI phenomenon prevails in case of high laser intensities ($10^{18} < I < 10^{20}$ W/cm^2) and in this case cluster Coulomb expansion can be assimilated as a system consisting only of ions, which are initially located with the same distribution of the atoms in the neutral cluster. Moreover, the direct effect of the laser electric field on ion dynamics is negligible, simplifying the theoretical treatment of the Coulomb explosion significantly. Ion acceleration to high energies is conventionally realized by accelerators as synchrotron or cyclotron, while laser-driven ion acceleration could be an exciting alternative to realize compact devices with the clear advantage of exploiting the strong electric field generated by the break of quasi-neutrality of the target. On the contrary, several issues need to be overcome to consider this technology exploitable in practical terms: the efficiency

of acceleration mechanism and its stability, the quality of the ion beam produced and the spread of the energy spectrum. In particular, almost all the above mentioned applications require an ion beam with a small energy spread $\Delta\mathcal{E}/\mathcal{E} \leq 2\%$. On the one hand, if we consider hadrontherapy, this condition is essential to save healthy tissues and deliver high doses to the tumor; on the other hand in case of fast-ignition, the proton spectra needed is quasi-monoenergetic (Roth et al., 2001). Those are the reasons why laser-matter interaction is an essential field of research and several theoretical, numerical and experimental essays have been succeeded in order to understand the physics behind this ions acceleration mechanism.

The first type of targets tested were low-density gases ($\rho < 10^{19}$ atoms/cm^3), but the fraction of laser energy absorbed in this case is very low ($< 1\%$). Considering solid targets ($\rho \cong 10^{23}$ atoms/cm^3), the deposition rate of the laser energy is quite high, close to 80%. Then spherical atomic nanoclusters were examined: macro-aggregate of atoms bonded by Van der Waals forces and composed of a variable number of atoms ($10^2 < N < 10^9$). In particular, those targets are interesting because they combine properties typical of solid matter and gases and a simple adiabatic expansion of a dense gas flux in the vacuum is sufficient to produce them. A progressively cooling process due to the conversion of the thermal energy in kinetic energy is able to assemble solid droplets at high densities. The resulting nanocluster is capable of collecting almost entirely the laser radiation and can be accelerated up to energies some order of magnitude higher than the one achieved during the explosion of small molecules (Ditmire et al., 1997). Initially, only homogeneous clusters made by one ion species were studied and it has been verified that the energy spectrum produced has a very broad shape (Last and Jortner, 2001a; Krainov and Roshchupkin, 2001). Recently, it has been demonstrated that the presence of ion mixtures can lead to a quasi-monoenergetic distribution of the species with the larger charge-to-mass ratio (Last and Jortner, 2001b, 2005; Hohenberger et al., 2005; Murakami and Tanaka, 2008; Andreev et al., 2010), under particular conditions of interest. The increasing potential due to the multicharged ions presence boosts the energy of the light ions inside the cluster. Different initial densities have been tested, connecting the distribution of the ions with the ion energy spectrum (Bychenkov and Kovalev, 2005b). Moreover, a strong relationship between the presence of overtakings in the fast species and a narrow profile of the energy spectrum has been verified with numerical simulations (Boella et al., 2016). Therefore, the mechanism of formation of shock shells during the expansion of the cluster takes an essential role in the investigation of the energy spectra (Popov et al., 2010; Li et al., 2007).

Also other types of targets have been studied, such as double-layer targets (Esirkepov et al., 2002; Bychenkov et al., 2004), made by the superposition of two thin foils of different materials, in order to achieve higher peak energies and a longer acceleration of the fast species, (Morita et al., 2012). In the interaction between laser pulses and a thin solid slab, the electrons of the foil could be heated up to

MeV energies, spreading out in a broad halo near the ion core: this vacuum region triggers plasma expansion. With the ability to improve the intensity contrast ratio of laser pulses and advancing technologies available in the production of high-quality ultrathin plane targets (thickness $100 - 1000$ Å), a very strong laser field is even capable of laying out all the electrons from a thin target, causing a Coulomb explosion (Bychenkov and Kovalev, 2005a). Therefore, two possible regimes of expansion can rise, depending on the electron temperature. In particular, if the electron Debye length, λ_{DE}, is comparable with the thickness of the slab, the Coulomb explosion limit is reached; on the contrary, if the target foil is thicker than λ_{DE}, a quasi-neutral expansion with charge separation effects can occur (Mora, 2003). In case of very high intensities of the laser, not only can the ultra-short pulse expel all the electrons from the correspondent irradiated area of the foil, but it also pushes the remaining ions, with a direction of propagation parallel to the laser one. In this regime of expansion both direct Coulomb explosion and the radiation pressure phenomena are dominant (Esirkepov et al., 2004). In case of very thin targets, the laser is only able to knock out all the electrons from the focal spot, without accelerating the foil and the only mechanism of acceleration is the Coulomb explosion. When we consider thicker targets, the light of the laser is reflected inside their thickness and the radiation pressure regime is achieved, as a sum of the incident, transmitted and reflected electromagnetic wave momentum fluxes. Numerical simulations confirm that the radiation pressure regime remains dominant in the ultra-relativistic case (Bulanov et al., 2008), while in some range of ion energies both regimes can coexist. Only when the radiation pressure of the laser is present, in a first phase ions are pushed by a strong one-dimensional electric field in the laser direction of propagation, but as the expansion evolves 3D effects become predominant and are not negligible. On the other hand, in case of pure Coulomb explosion in the first stages too, of the expansion both species of ions propagate in 2D (or 3D). Another crucial question is the dynamics of the slower species, with the lower charge to mass ratio. If the difference between the two masses is large enough, in the first transient of acceleration slow ions can be considered at rest, with the result of a time-independent electric field and a stationary, but inhomogeneous in space, acceleration of the fast species. In reality, it has been shown that the fast species dynamic is quite long and the propagation of the slow ions make the electric field time-dependent (Fourkal et al., 2005).

1.1 Structure of the thesis

This thesis investigates the phenomenon of pure Coulomb explosion in different geometries, with homogeneous or heterogeneous targets. In case of the presence of two species, the dynamic of both fast and slow ions is considered. Chapter 2 analyses the expansion of spherical nanoclusters from a theoretical point of view;

starting from a homogeneous target we demonstrate numerically how the shape of the energy spectrum is poor of quality, with a considerable energy spread around the peak. Consequently, an analytical model to study the expansion of composite cluster is proposed, connecting the rise of shock shells with a narrow behavior of the kinetic energy spectrum of the fast species. The existence of a limit value on one of the mixture parameters is retrieved and rigorously demonstrated to determine the presence of overtakings between fast ions. In this case, the theoretical model is no longer valid and a numerical method is developed to study the spherical explosion, the so-called shell method. The problem is essentially one dimensional, computational particles are in the shape of spherical shells and by using the Gauss's formula, the electric field is readily evaluated. Different results are presented in Chapter 4 in case of spherical clusters made by two ion species, varying the charge-to-mass ratio and the composition of the mixture. Then, cylindrical targets are considered, firstly using gridless particle techniques (Dawson, 1962; Eldridge and Feix, 1962) and then introducing an in-house two-dimensional PIC code. Numerical methods without a computational grid are useful in situations, in which the physical domain occupied by the particles increases rapidly in time (as for plasma expansion and explosion). In this framework, in general situations one could employ a set of computational particles and directly calculate the electric field acting on each of them, as the sum of the contribution of the other particles. This requires an extremely high computational effort unless the problem under exam presents some symmetry. The three-dimensional Soft-Spheres method was developed to this purpose, it is an N-body technique useful if a hypothesis on the symmetry of the system cannot be made. Whenever an axial symmetry is present, as in cylindrical targets, the EXPICYL PIC code can be used to simulate the expansion. EXPICYL is a two-dimensional PIC code without a fixed computational domain to follow expansion phenomena correctly.Finally, another tool was developed by the group: the ring method. This is a gridless N-body method and here the particles are modeled as thin circular rings, which are characterized by their radii and their axial coordinates. In this case, the evolution of the force acting on each particle necessarily requires the calculation of the sum of contributions due to the other particles. All the details of the numerical methods are explained in Chapter 3, combined with the validation of the codes in reference cases for which the analytic solution is available. Different results are presented in case of homogeneous cylindrical targets, heterogeneous slab made by two ion species or double layer targets, (Chapter 5). In Chapter 6 a brief overview of the results presented in the thesis is exposed, with some considerations on possible future developments.

The papers published by the author and cited in the thesis are reported in the annexes, at the end of the thesis. Then, the text of a submitted paper on a side activity of the PhD is appended.

Chapter 2

Coulomb explosion of spherical clusters

In this chapter, the dynamic of Coulomb explosion in uniform and composite clusters is analyzed. The first section presents a brief introduction to the expansion of a cluster with an initial uniform charge density and composed by one ion species only. In this case, the analytic solution is available and the aim is the calculation of the kinetic energy spectrum in order to demonstrate that its shape and spread of energy is not suitable for practical applications. Section 2.2 presents a detailed theoretical analysis of the expansion of spherical clusters made by a mixture of two species, investigating the conditions required to harden the energy spectra. The ion dynamic is described in the two concentric regions formed during the evolution of the explosion. In particular, the ions with the largest charge-to-mass ratio take higher velocities and are called fast ions, while the slow ions make the other species. Therefore, when the cluster starts to expand, in the inner region we can find a mixture of slow and fast ions, while in the outer region only fast ions are present, with two different trends of the electric field. Two parameters characterize the dynamics of the mixture expansion: μ, which depends on the masses and charges of the two species, and α, which is the fraction of fast ions on the total. The influence of the value of α on the possible rise of shock shells and the correlation with the hardening of the kinetic energy spectrum is demonstrated rigorously. It has been found numerically that for typical values of α, called α_{crit}, the energy spread in the spectrum is mainly contained, as showed in a previous work (Li et al., 2007). We demonstrate that this value depends only on the charges, and not on the masses, of the ions, and we obtain the expression of α_{crit} theoretically for each type of mixture, starting from the limit case of slow ions with infinite mass, consequently at rest, and then adapting the dissertation also in the case of slow ions with finite mass. Whenever the hypothesis of the theoretical model are supported, the properties of the explosion are deduced analytically; unlikely, the study is completed numerically with the so-called "shell method" (Boella et al., 2011; D'Angola et al., 2014), described in

details in Sec. 2.3. The mentioned method gives extremely precise results by taking advantage of the spherical symmetry of the problem.

Declarations   Part of the work described in this Chapter was also previously published in the following publications, further reported in Appendix of this thesis: 1) E. Boella, B. Peiretti Paradisi, A. D'Angola, L. O. Silva and G. Coppa, Study on Coulomb explosions of ion mixtures, Journal of Plasma Physics 82 (2016) 905820110, 2) B. Peiretti Paradisi, E. Boella, A. D'Angola and G. Coppa, Gridless simulation of collisionless systems with high degree of symmetry, Computer Physics Communications, 2017.

2.1   Expansion of a sphere with uniform density

The Coulomb explosion of a sphere of initial radius R, made by one ion species, is here presented from a theoretical point of view, as a reference. The ions are considered initially at rest and the charge density distribution is uniform inside the sphere, consequently the electric field is linear with the radius inside the initial cluster. The presence of Coulomb repulsive forces between the ions triggers the start of the expansion. The hypothesis of absence of overtakings between ions is proposed: if the charge density remains constant during the expansion and the electric field lasts as a linear function of the radius, inner ions cannot be accelerated more than the outer ones and will not reach them. The motion equation for one ion inside the initial sphere of radius R accelerated by the Coulombian force and written in Gaussian units, is given by

$$\begin{cases} \dfrac{\mathrm{d}^2 r}{\mathrm{d}t^2} = \dfrac{q}{m} E(r,t), \\[2ex] \dfrac{\mathrm{d}r}{\mathrm{d}t}(0, r_0) = 0, \\[2ex] r(0, r_0) = r_0, \end{cases} \tag{2.1}$$

where q is the charge of one ion, m its mass, $E(r,t)$ the electric field at a radius $r < R(t)$ and $r(t, r_0)$ will be the radial position of a particle at time t, which has started its trajectory at radius r_0. The system in Eq. (2.1) is valid for each ion of the cluster during the expansion since overtakings between ions do not occur. The electric field at a radius $r < R(t)$ can be calculated applying Gauss's law as

$$E(r,t) = \frac{Q(r,t)}{r^2} = \frac{4}{3}\pi q n r, \tag{2.2}$$

being $Q(r,t)$ the total charge inside a sphere of radius $r < R(t)$ and n the density inside the sphere, both expressed at time t. Defining the dimensionless variable

$$\xi = \frac{r}{r_0}, \tag{2.3}$$

and the modified charge

$$\tilde{Q} = \frac{qQ(r,t)}{m}, \tag{2.4}$$

the system (2.1) becomes

$$\begin{cases} \dfrac{\mathrm{d}^2\xi}{\mathrm{d}t^2} = \dfrac{\tilde{Q}}{\xi^2 r_0^3}, \\[2ex] \dfrac{\mathrm{d}\xi}{\mathrm{d}t}(0) = 0, \\[2ex] \xi(0) = 1. \end{cases} \tag{2.5}$$

To solve this type of differential equation one of the methods starts integrating one time respect to the time variable t, obtaining

$$\frac{1}{2}\left(\frac{\mathrm{d}\xi}{\mathrm{d}t}\right)^2 + \frac{\tilde{Q}(r,t)}{\xi r_o^3} = \mathcal{K}, \tag{2.6}$$

being $\mathcal{K}$ a constant given by the initial condition inside the cluster. If the hypothesis of no overtakings between ions during the expansion is valid, the term $\tilde{Q}(r,t)$ can be calculated considering that it will remain constant in time since the start of the expansion

$$\tilde{Q}(r,t) = \tilde{Q}_0(r_0,0) = \tilde{Q}_0, \tag{2.7}$$

substituting in (2.6)

$$\frac{1}{2}\left(\frac{d\xi}{dt}\right)^2 + \frac{\tilde{Q}_0}{\xi r_0^3} = \frac{\tilde{Q}_0}{r_0^3}, \tag{2.8}$$

and consequently Eq. (2.8) can be written as

$$\left(\frac{\mathrm{d}\xi}{\mathrm{d}t}\right) = \sqrt{2\frac{\tilde{Q}_0}{r_0^3}\left(1 - \frac{1}{\xi}\right)}; \tag{2.9}$$

splitting the variables and integrating the second member respect to the time variable, we obtain

$$\int_1^\xi \sqrt{\frac{\xi'}{1-\xi'}}\mathrm{d}\xi' = \sqrt{2\frac{\tilde{Q}_0}{r_0^3}}t, \tag{2.10}$$

rewriting and defining the function $F(\xi)$ the first member of the Eq. (2.10) becomes

$$F(\xi) = \int_1^\xi \sqrt{\frac{\xi'}{1-\xi'}}\mathrm{d}\xi' = \sqrt{\xi(\xi-1)} + \log(\sqrt{\xi} + \sqrt{\xi-1}). \qquad (2.11)$$

The evolution of the trajectory is obtained in an implicit expression as

$$F\left(\frac{r(t)}{r_0}\right) = \sqrt{2\frac{\tilde{Q}_0}{r_0^3}}t. \qquad (2.12)$$

From Eq. (2.9) the velocity of the particle is

$$v(r_0, t) = r_0\frac{\mathrm{d}\xi}{\mathrm{d}t} = \sqrt{2\frac{\tilde{Q}_0}{r_0^3}\left(1-\frac{1}{\xi}\right)}, \qquad (2.13)$$

substituting the definition of ξ the expression for the velocity becomes

$$v(r_0, t) = \sqrt{2\tilde{Q}_0}\sqrt{\frac{1}{r_0} - \frac{1}{r(t)}}. \qquad (2.14)$$

Finally, the Eqs. (2.14) and (2.12) describe the velocity and the trajectory of a particle that takes part in a Coulomb explosion of a cluster made by one ion species, with the hypothesis of no overtakings between the ions during the expansion.

Figure 2.1 displays a typical energy spectrum, when only one species is present in the spherical plasma. The energy distribution is spread without favoring one specific interval of values and this configuration is not suitable for practical applications.
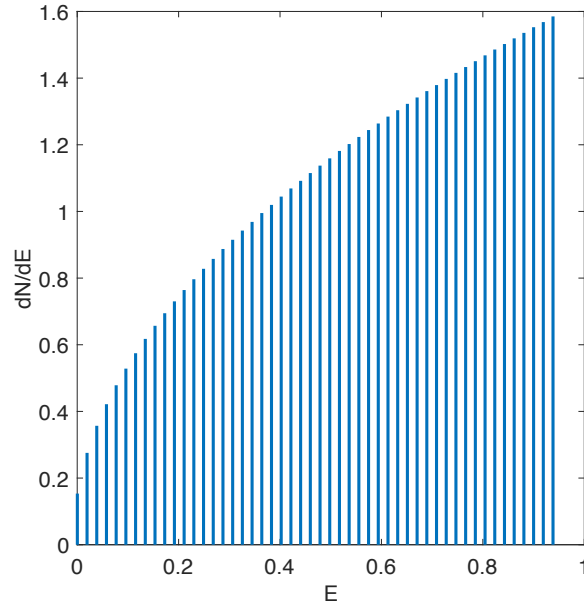
Figure 2.1: Energy spectrum for a uniform spherical plasma, made by one ion species.

2.2 Expansion of a sphere made by an ion mixture of two species

In this section, the expansion of spherical nanoplasmas composed by more than one ion species is examined. In particular, a mixture of two types of ions uniformly distributed is considered; the mixture is characterized by the parameter μ defined as

$$\mu = \frac{q_s/m_s}{q_f/m_f} < 1, \qquad (2.15)$$

where m_s, m_f and s q_s, q_f are, respectively, the masses and the electric charges of the two species of ions. The ions are supposed initially at rest when the influence of their repulsive forces starts to move them. Obviously, the species which moves faster is the one with the higher charge-to-mass ratio; consequently, two regions develop with spherical shape, called S_f and S_s, having radius $R_f(t)$ and $R_s(t)$, with $R_s \leqslant R_f$. The two spheres are concentric. On the one hand, in the sphere S_s fast and slow particles are present and R_s depicts the frontline of the slow ions; on the other hand, only fast particles would be in the spherical shell S_f, outside S_s. The ion dynamics are different in the inner and outer region, and they will be studied in detail in the following section.

2.2.1 Mathematical model of the expansion dynamics

In the beginning, the distribution of all the ions is uniform inside a sphere of radius R. Consequently, the charge density is constant and the radial electric field is linear. The influence of the repulsive forces starts the expansion, and both slow and fast ions begin to move uniformly generating an inner sphere, S_s, where the charge density remains constant, producing a linear behavior of the electric field again.

Then, at any time, the electric field inside S_s remains a linear function of the radius r and can be described as:

$$E(r,t) = A(t)r \quad \text{for} \quad r \leqslant R_s(t). \tag{2.16}$$

Exploiting this hypothesis, the equations of motion for both the fast and the slow ions inside S_s are deduced easily. The uniform expansion can be depicted by introducing two functions, $\xi_s(t)$ and $\xi_f(t)$, describing the dynamics of slow and fast ions: an ion initially at $r = r_0$ at time t will be at $r = r_0\xi_s(t)$ or $r = r_0\xi_f(t)$. In this way, $\xi_s(t)$ and $\xi_f(t)$ do not depend on the initial position of the ions. Besides, we define $n_{s,0}$ and $n_{f,0}$ as the initial densities of the two species and their evolution in time is given by

$$n_s(t) = \frac{n_{s,0}}{\xi_s^3(t)}, \ n_f(t) = \frac{n_{f,0}}{\xi_f^3(t)}. \tag{2.17}$$

Applying Gauss's law, inside the sphere S_s the electric field can be written as:

$$E(r,t) = \frac{4\pi}{3} \left(\frac{q_f n_{f,0}}{\xi_f^3(t)} + \frac{q_s n_{s,0}}{\xi_s^3(t)} \right) r \tag{2.18}$$

which has the same dependence on r hypothesized in Eq. (2.16). In the end, the expression (2.18) is introduced into the equations of the motion for fast and slow ions. Being the electric field linear on r_0 and expressing the acceleration of the ions of the two species as $r_0 d^2\xi_f/dt^2$ and $r_0 d^2\xi_s/dt^2$, we obtain

$$\begin{cases} \dfrac{\mathrm{d}^2\xi_f}{\mathrm{d}t^2} = \dfrac{4\pi}{3}\dfrac{q_f}{m_f} \left(\dfrac{q_f n_{f,0}}{\xi_f^3} + \dfrac{q_s n_{s,0}}{\xi_s^3} \right) \xi_f \ , \\[2em] \dfrac{\mathrm{d}^2\xi_s}{\mathrm{d}t^2} = \dfrac{4\pi}{3}\dfrac{q_s}{m_s} \left(\dfrac{q_f n_{f,0}}{\xi_f^3} + \dfrac{q_s n_{s,0}}{\xi_s^3} \right) \xi_s \ , \end{cases} \tag{2.19}$$

where there is no more dependence on r_0. Equations (2.19) can be reworked in a

more compact way, as

$$
\begin{cases}
\dfrac{\mathrm{d}^2\xi_f}{\mathrm{d}t^2} = \nu^2 \left(\dfrac{\alpha}{\xi_f^3} + \dfrac{\beta(1-\alpha)}{\xi_s^3} \right) \xi_f, & \xi_f(0) = 1, & \dfrac{\mathrm{d}\xi_f}{\mathrm{d}t}(0) = 0 \\[4mm]
\dfrac{\mathrm{d}^2\xi_s}{\mathrm{d}t^2} = \nu^2\mu \left(\dfrac{\alpha}{\xi_f^3} + \dfrac{\beta(1-\alpha)}{\xi_s^3} \right) \xi_s, & \xi_s(0) = 1, & \dfrac{\mathrm{d}\xi_s}{\mathrm{d}t}(0) = 0
\end{cases}
\tag{2.20}
$$

being

$$
\nu = \left[\frac{4\pi q_f^2(n_{f,0} + n_{s,0})}{3m_f} \right]^{1/2}, \quad \alpha = \frac{n_{f,0}}{n_{f,0} + n_{s,0}}, \quad \beta = \frac{q_s}{q_f}.
\tag{2.21}
$$

The variable ν can be interpreted as a characteristic frequency for the fast ion expansion, while α is the number of fast ions on the total number of ions in the cluster.

During the whole explosion, the motion of slow ions is described at any time by the system (2.20). Otherwise, for the dynamics of fast ions the system (2.20) is valid only since they are inside S_s. A fast ion, starting its expansion at $r = r_0 \leq R$, gets to the frontline of the inner region when $r_0\xi_f(t) = R\xi_s(t)$. $\tau(r_0)$ in the following becomes is defined as the time the ion passes over the sphere S_s and it is retrieved by solving the equation

$$
\frac{\xi_s(\tau)}{\xi_f(\tau)} = \frac{r_0}{R}.
\tag{2.22}
$$

If we consider a fast ion originally at r_0, the electric field for $r \geqslant R_s$ can be formulated as $Q(r,t)/r^2$, where $Q(r,t)$ is the charge in the sphere of radius r at time t; since overtakings between fast ions do not take place, $Q(r,t)$ is calculated as the sum of the total charge of the slow ions and the charge of fast ions initially inside a sphere of radius r_0:

$$
Q(r,t) = Q(r_0,t) = \frac{4\pi}{3} \left(q_s n_{s,0} R^3 + q_f n_{f,0} r_0^3 \right).
\tag{2.23}
$$

Therefore, for $t > \tau(r_0)$, for a fast ion outside S_s the equation of motion is

$$
m_f \frac{\mathrm{d}^2 r}{\mathrm{d}t^2} = -\frac{\partial}{\partial r} \left(\frac{q_f Q(r_0)}{r} \right), \quad r(\tau) = \xi_f(\tau)r_0, \quad \frac{\mathrm{d}r}{\mathrm{d}t}(\tau) = \frac{\mathrm{d}\xi_f}{\mathrm{d}t}(\tau)r_0.
\tag{2.24}
$$

If we want to deduce the asymptotic kinetic energy of the fast ions, ϵ_∞, Eq. (2.24) can be integrated as

$$
\epsilon_\infty = \frac{1}{2}m_f \left\{ \frac{\mathrm{d}\xi_f}{\mathrm{d}t}(\tau(r_0)) r_0 \right\}^2 + \frac{q_f Q(r_0)}{\xi_f(\tau)r_0}.
\tag{2.25}
$$

We define the energy spectrum of the fast ions, ρ_ϵ, as

$$
\rho_\epsilon = \frac{1}{N_f} \frac{\mathrm{d}N_f}{\mathrm{d}\epsilon_\infty}
\tag{2.26}
$$

11

where N_f represents the total number of fast ions, while $\mathrm{d}N_f$ is the number of ions taking asymptotic energy in the interval $\mathrm{d}\epsilon_\infty$. Making use of Eqs. (2.22) and (2.25), the spectrum can be made explicit as a parametric function of τ, as:

$$\rho_\epsilon = \frac{4\pi r_0^2 n_{f,0}}{N_f} \frac{\mathrm{d}r_0/\mathrm{d}\tau}{\mathrm{d}\epsilon_\infty/\mathrm{d}\tau}. \tag{2.27}$$

The analysis of the presence of overtakings between fast ions is of crucial importance: in this case, Eq. (2.25) is no longer valid and it is not helpful to deduce the energy spectrum of fast ions, while their dynamics can be depicted only numerically. The presence of shock shells occurs when the fraction of fast ions, α, is smaller than a critical value, α_{crit}. As an example, Fig. 2.2 shows the phase-space of the fast ions at different times, when shock shells are not present. Otherwise, when two fast ions have radii $r_1 < r_2$ and reach velocities $v_1 > v_2$ the formation of shock shells begins, as shown in Fig. 2.3 There is an easy way to understand if shock shells will appear in a Coulomb explosion, without requiring a full numerical simulation of the phenomenon. The derivative of ϵ_∞ is calculated with in relation to r_0, using Eq. (2.25), which is valid only in the absence of shocks. If the condition

$$\frac{\mathrm{d}\epsilon_\infty}{\mathrm{d}r_0} > 0 \tag{2.28}$$

is valid for each $r_0 \in [0, R]$, the ions in the inner zones gain slower velocity compared to outer ones and cannot reach them; in this case, no overtaking occurs. Alternatively, if $\mathrm{d}\epsilon_\infty/\mathrm{d}r_0$ takes negative values for some r_0, overtakings between fast ions will take place. Following this rule, the presence of a limit value for α can be promptly confirmed. Generally, if $\alpha > \alpha_{crit}$ the derivative $\mathrm{d}\epsilon_\infty/\mathrm{d}r_0$ is positive and no shock arises; for $\alpha < \alpha_{crit}$, $\mathrm{d}\epsilon_\infty/\mathrm{d}r_0$ changes its sign, suggesting that the fast particles overtake each other, with the formation of shock shells.

The phenomenon of the formation of shock shells is crucial also because of its strong connection with the monochromaticity of the ion spectrum. This relation has been studied with a detailed analytic analysis, demonstrating that the width of the asymptotic energy spectrum can assume a very narrow profile. In particular, under certain conditions all the ions may have almost the same kinetic energy, indicating a multi-valued ion phase space.
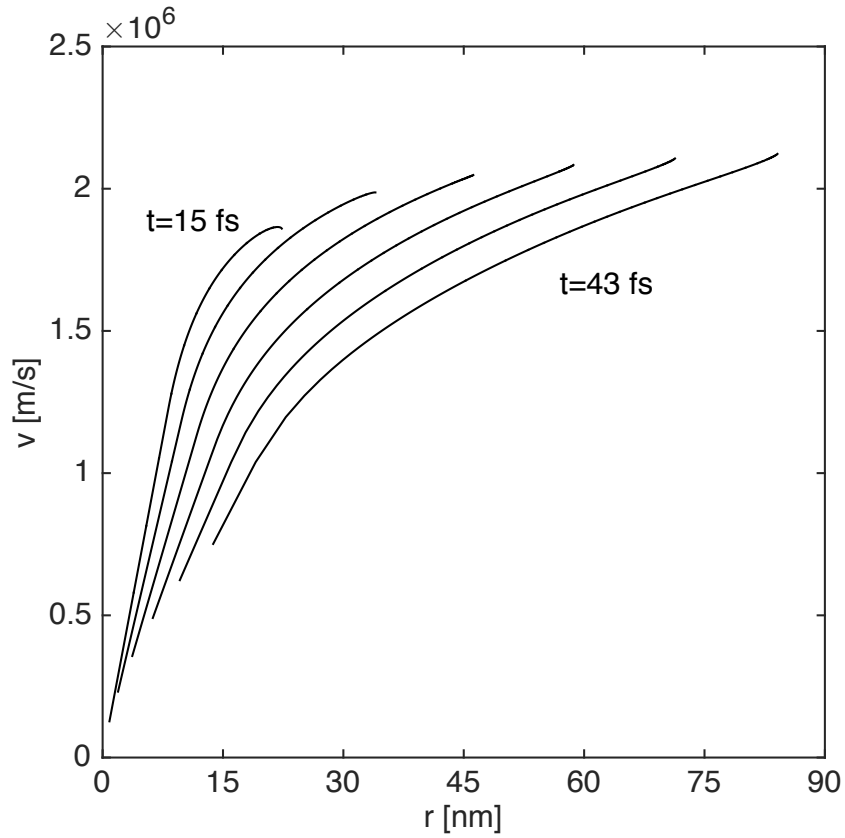
Figure 2.2: Phase space for a mixture C^+H^+ with $\alpha = 0.4 > \alpha_{crit}$, no formation of shock shells. Adapted from: E. Boella, B. Peiretti Paradisi, A. D'Angola, L. O. Silva and G. Coppa, Journal of Plasma Physics 82 (2016).
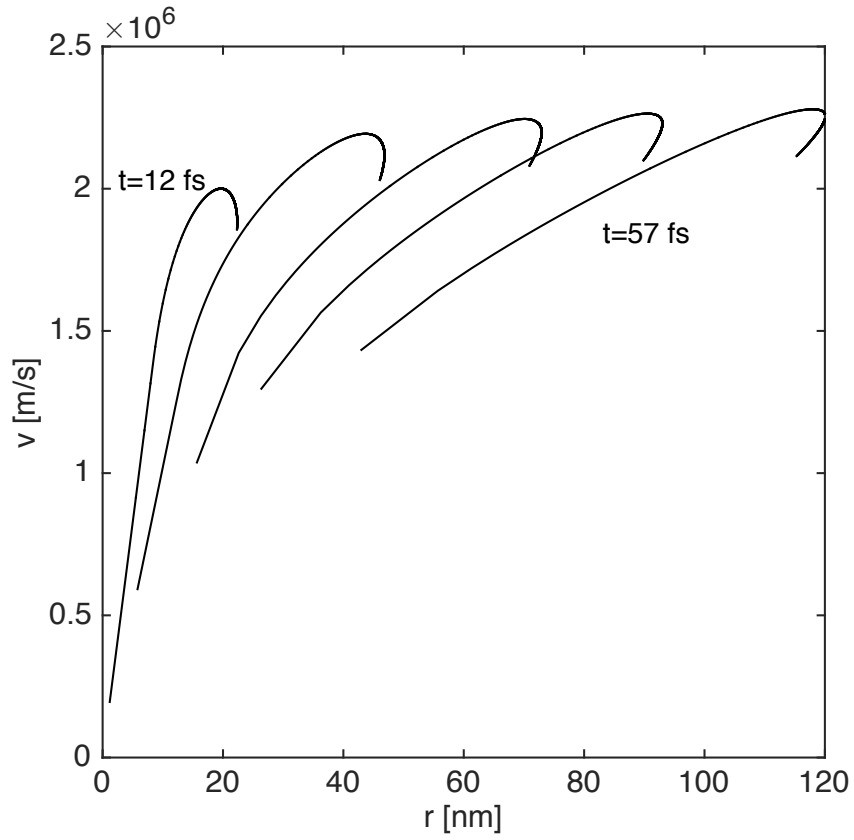
Figure 2.3: Phase space for a mixture C^+H^+ with $\alpha = 0.2 < \alpha_{crit}$, shock shells are present. Adapted from: E. Boella, B. Peiretti Paradisi, A. D'Angola, L. O. Silva and G. Coppa, Journal of Plasma Physics 82 (2016)

2.2.2 The theoretical derivation of α_{crit}

In the following section, the value of α_{crit} is theoretically deduced, starting from the limit case of slow ions at rest $(m_s \to \infty)$ and then generalizing the result for all the other situations when m_s takes a finite value. Finally, it is demonstrated rigorously that the arise of shocks depends only on the ratio between the total charge of the fast ions with respect to the one of the slow ions, and not on their masses. We start defining the two quantities Q_s and Q_f as the total charge of slow and fast ions, and then calculating the Hamiltonian of the fast ions dynamics, in the case of absence of shocks

$$\mathscr{H}(r, p_r; r_0) = \frac{p_r^2}{2m_f} + \frac{q_f Q_f}{r}\left(\frac{r_0}{R}\right)^3 + q_f \Phi_s(r, R_s(t)), \quad (2.29)$$

being r_0 the initial position of a fast ion. $\Phi_s(r, \rho)$ is the electrostatic potential at radius r generated by fixed ions with a uniform charge distribution inside a sphere of radius ρ:

$$\Phi_s(r, \rho) = \begin{cases} \dfrac{3Q_s}{2\rho} - \dfrac{Q_s r^2}{2\rho^3} & \text{for} \quad r \leqslant \rho, \\[3mm] \dfrac{Q_s}{r} & \text{for} \quad r \geqslant \rho. \end{cases} \quad (2.30)$$

In the limit situation with $m_s \to +\infty$, $R_s(t)$ is constant and $R_s = R$; it means that $\mathscr{H}$ has no explicit dependence on time and it is a constant of motion. Consequently, the asymptotic energy ϵ_∞ can be rewritten readily as a function of r_0

$$\epsilon_\infty(r_0) = q_f \left[\frac{Q_f - Q_s/2}{R^3} r_0^2 + \frac{3Q_s}{2R}\right] \quad (2.31)$$

from which the energy spectrum can be easily deduced (Li et al., 2007).

Depending on the sing of the term $Q_f - Q_s/2$, two different situations can take place, as shown in Fig. 2.4. On one hand when $Q_f > Q_s/2$, according to Eq. (2.31), ϵ_∞ is an increasing function of r_0, then there is no presence of overtakings between fast ions and the spectrum deduced analytically is correct (Fig. 2.5 curves a, b, c). On the other hand if $Q_f < Q_s/2$, the ion velocity is a decreasing function of r_0, and this fact suggests that the inner ions of the cluster are headed to overtake the ions close to the fast frontline. Consequently, the hypothesis of no overtakings and Eq. (2.31) are no longer valid. In this case, the spectrum can be deduced numerically, as shown in Fig. 2.5, curves e, f, g, where the energy spectra have been calculated using the shell method, see Sec. 2.3. In the limit case when $Q_f = Q_s/2$ (Fig. 2.5, curve d) Eq. (2.31) can still be used, considering $Q_f - Q_s/2 \to 0^+$. In this abstract configuration, the spectrum is perfectly monoenergetic.
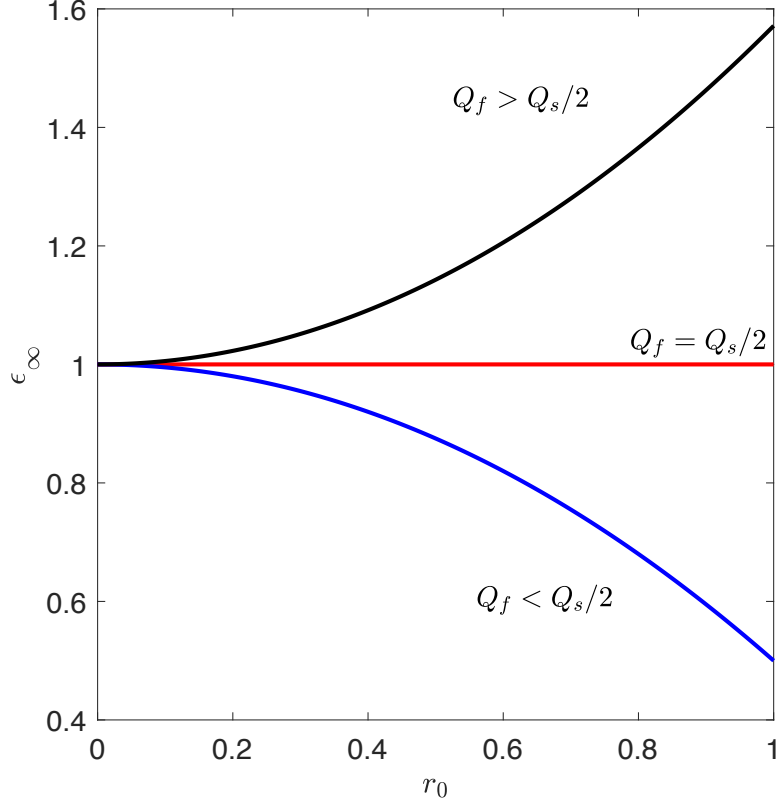
Figure 2.4: Situation with slow ions at rest, ϵ_∞ as a function of r_0: when $Q_f > Q_s/2$ inner fast ions have lower asymptotic energies, on the contrary when $Q_f < Q_s/2$ the outer ions are the less energetic and overtakings can take place.

Generally, the mass of slow ions is finite and in this case their motion must be considered. Then, the potential of the slow ions, Φ_s, present in the Hamiltonian, is a function of time, Eq. (2.29), as the frontline $R_s(t)$ is no more fixed. Finally, $\mathscr{H}$ is not constant in time:

$$\frac{\mathrm{d}\mathscr{H}}{\mathrm{d}t} = \frac{\partial \mathscr{H}}{\partial t} = q_f \frac{\partial \Phi_s}{\partial R_s} \frac{\mathrm{d}R_s}{\mathrm{d}t}. \tag{2.32}$$

Theoretically, the value of the asymptotic energy can be deduced integrating Eq. (2.32) respect to the time t:

$$\epsilon_\infty = \mathscr{H}(t \to +\infty) = \mathscr{H}(t = 0) + q_f \int_0^{\tau(r_0)} \frac{\partial \Phi_s}{\partial R_s}(r(t), R_s(t)) \frac{\mathrm{d}R_s}{\mathrm{d}t} \mathrm{d}t \tag{2.33}$$

where the upper integration limit can be established equal to $\tau(r_0)$, because for a time $t > \tau$ the considered ion will be outside $S_s(t)$ and the term $\partial \Phi_s / \partial R_s$ goes to
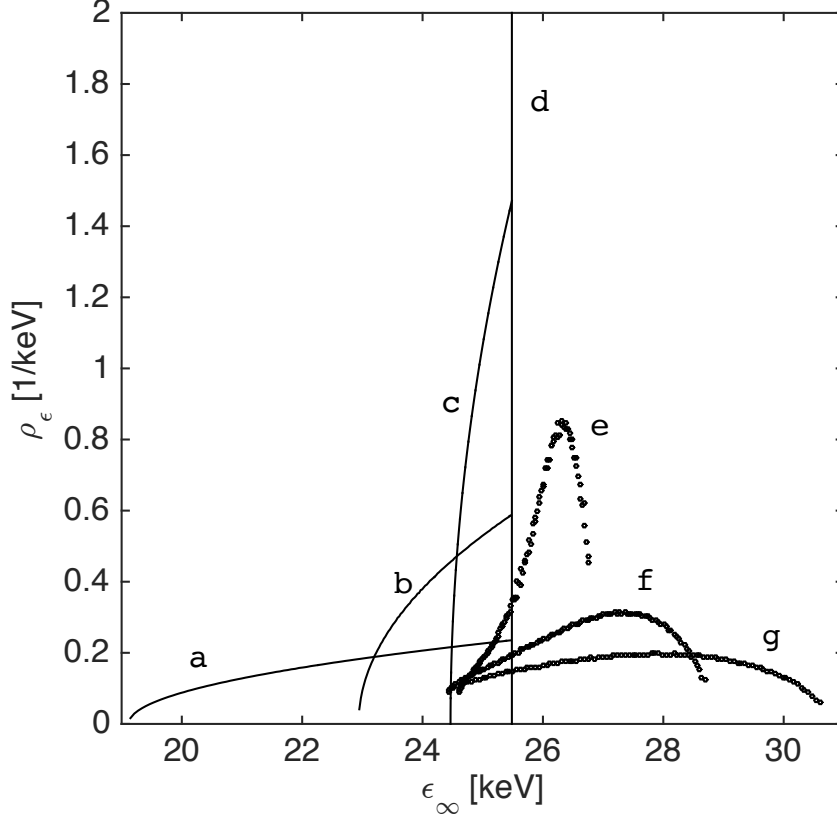
Figure 2.5: Energy spectra of a mixture with slow ions at rest ($m_s \to +\infty$) and Hydrogen fast ions, for different value of α in the range $[0.2, 0.5]$. Curves a, b and c depict mixtures with $\alpha > \alpha_{crit}$; in this case shocks are not present and the numerical spectra are equal to the analytic curve. Curve d shows the limit case of $\alpha = \alpha_{crit}$, where the energy spectrum is singular. Curves e, f and g represent situations with $\alpha > \alpha_{crit}$, for which the spectra have been computed using the shell method, see Sec. 2.3. Adapted from: E. Boella, B. Peiretti Paradisi, A. D'Angola, L. O. Silva and G. Coppa, Journal of Plasma Physics 82 (2016).

zero. We can notice the correspondence between $\mathscr{H}(t = 0)$ and the asymptotic energy for fixed slow ions (Eq. (2.29)), and rewriting $r(t)$ and $R_s(t)$ as functions of ξ_f and ξ_s, we finally obtain

$$\epsilon_\infty = q_f \left[\frac{Q_f - Q_s/2}{R^3} r_0^2 + \frac{3Q_s}{2R} \right] - \frac{3Q_s q_f}{2R} I(r_0) \qquad (2.34)$$

17

where $I(r_0)$ is defined as

$$I(r_0) = \int_0^{\tau(r_0)} \left[1 - \left(\frac{r_0 \xi_f(t)}{R \xi_s(t)} \right)^2 \right] \frac{\xi_s'(t)}{\xi_s^2(t)} \mathrm{d}t. \tag{2.35}$$

It is interesting to highlight that the integral I is always non negative and it is because the motion of slow ions takes some energy away from the fast ones.

Now we can examine the condition $\mathrm{d}\epsilon_\infty/\mathrm{d}r_0 > 0$ for $r_0 \in [0, R]$. Starting from Eq. (2.35), we obtain:

$$\frac{\mathrm{d}I}{\mathrm{d}r_0} = \frac{\xi_s'(\tau)}{\xi_s(\tau)^2} \left(1 - \frac{r_0^2 \xi_f(\tau)^2}{R^2 \xi_s(\tau)^2} \right) \frac{\mathrm{d}\tau}{\mathrm{d}r_0} - \int_0^{\tau(r_0)} \frac{2 r_0 \xi_f^2 \xi_s'}{R^2 \xi_s^4} \mathrm{d}t. \tag{2.36}$$

From this formula, considering that $\mathrm{d}\tau/\mathrm{d}r_0 < 0$, we have

$$\frac{\mathrm{d}I}{\mathrm{d}r_0}(r_0) \leqslant 0 \quad \forall r_0 \in [0, R], \quad \frac{\mathrm{d}I}{\mathrm{d}r_0}(R) = 0; \tag{2.37}$$

being

$$\frac{d\epsilon_\infty}{dr_0} = 2 q_f \frac{Q_f - Q_s/2}{R^3} r_0 - \frac{3 Q_s q_f}{2R} \frac{\mathrm{d}I}{\mathrm{d}r_0}, \tag{2.38}$$

if $Q_f > Q_s/2$ the derivative $\mathrm{d}\epsilon_\infty/\mathrm{d}r_0$ is always positive, as the sum of two non-negative quantities, as shown as an example in Fig. 2.7. Consequently, ϵ_∞ is an increasing function (Fig. 2.6) and no overtakings can occur. Instead, if $Q_f < Q_s/2$ the quantity $\mathrm{d}\epsilon_\infty/\mathrm{d}r_0$ is somewhere negative (Fig. 2.9) and ϵ_∞ has some decreasing region (Fig. 2.8), then shock shells are present.

At the end, we have obtained that the limit value $Q_f = Q_s/2$ can be used in any case to distinguish explosion with or without shocks. In a previous paper (Li et al., 2007) this typical property of the Coulomb explosions of spherical clusters was obtained numerically and here rigorously proofed. From the discriminant on the total charges, the critical value of α is gained:

$$\alpha_{crit} = \frac{\beta}{2 + \beta}. \tag{2.39}$$

It is very interesting to denote the only dependence on the charge ratio of α_{crit}, without any dependence on the ions masses. For example, $\alpha_{crit} = 1/3$ for all the following mixtures HD, HT, DT and HC^+, where the value changes if we consider a mixture with another charge of the carbon as HC^{2+}, HC^{3+}. The expansion of these types of mixtures will be performed and analyzed in Chapter 4 of this thesis.
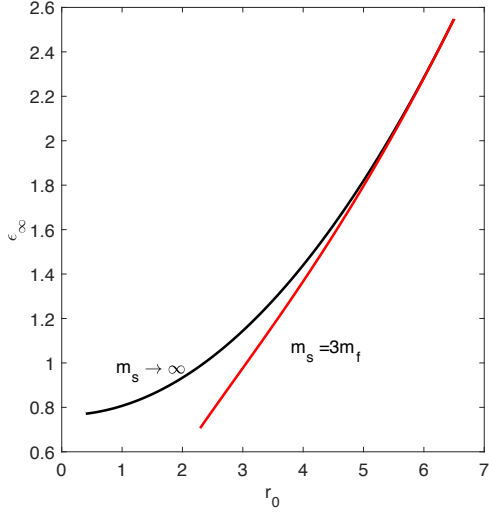
Figure 2.6: ϵ_∞ as a function of r_0, in a mixture with a value of the parameter $\alpha > \alpha_{crit}$. Comparison between the case of $m_s \to \infty$ and finite mass of slow ions. ϵ_∞ is an increasing function in case of slow ions at rest or not.

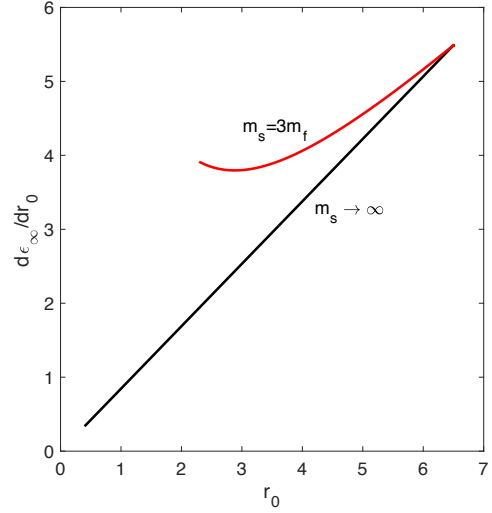Figure 2.7: Derivative of ϵ_∞ as a function of r_0, comparison between the case of $m_s \to \infty$ and finite mass of slow ions, $\alpha > \alpha_{crit}$. The derivative of ϵ_∞ is always positive, no overtakings can occur.
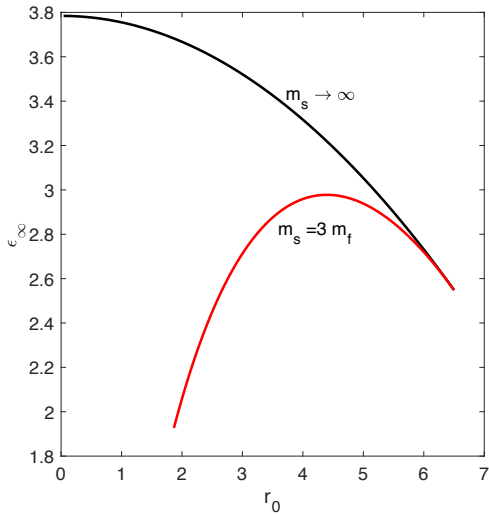
Figure 2.8: Same as Fig. 2.6, but with $\alpha < \alpha_{crit}$. In both cases there is a region where the function is decreasing and overtakings can occur.
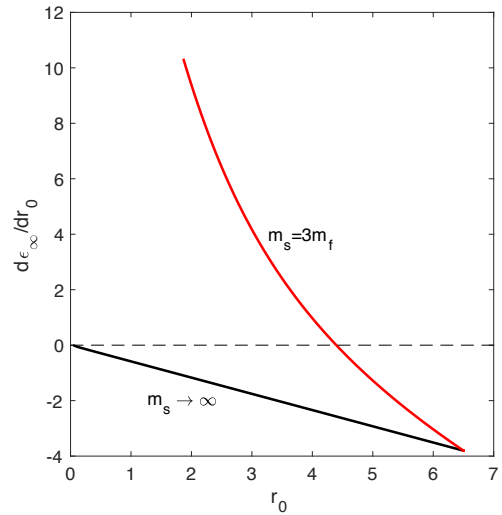
Figure 2.9: Same as Fig. 2.9, but with $\alpha < \alpha_{crit}$. In both cases there is a region in which the derivative is negative.

2.3   The shell method

In this section, the numerical method used to simulate the expansion in spherical geometry is presented, completely and rigorously. Other Authors introduced and applied the same method, with other formulations, (in particular, in refs. (Dawson, 1962; Eldridge and Feix, 1962; Popov et al., 2010)). Three formulations are presented, depending on the variables and coordinates used in the different frameworks.

First formulation   We start considering a set of N computational particles. Their coordinates $\mathbf{x}_i$ and momenta $\mathbf{p}_i$ are initialized, and the particles are put in order following the value of their radial coordinates $r_i = |\mathbf{x}_i|$, so that $r_j > r_i$ if $j > i$. According to their radial position, the electric field acting on each shell is estimated as:

$$\mathbf{E}_i = \left(\sum_{j=1}^{i-1} q_j + \tfrac{1}{2} q_i \right) \frac{\mathbf{x}_i}{r_i^3}, \tag{2.40}$$

by using the Gauss's formula and making use of the spherical symmetry of the problem. The factor $\frac{1}{2}$ present in Eq. (2.40) may be explained simply considering that, for $r = r_i - \epsilon$ ($\epsilon \to 0^+$) q_i does not contribute to the electric field, while for $r = r_i + \epsilon$ the total charge to be evaluated is $\sum_{j=1}^{i} q_j$. Therefore, a linear behavior of $\mathbf{E}$ is supposed at the interface and the factor $\frac{1}{2}$ gives the precise value of the field (Sect. 2.4 presents a rigorous proof of the formula above). The equation of motion can be written, knowing the electric field $\mathbf{E}$ on each computational particle:

$$\begin{cases} \dfrac{\mathrm{d}\mathbf{x}_i}{\mathrm{d}t} = \dfrac{\mathbf{p}_i}{m_i}, \\[2ex] \dfrac{\mathrm{d}\mathbf{p}_i}{\mathrm{d}t} = q_i \mathbf{E}_i \quad (\mathbf{x}_1, \mathbf{x}_2, ..., \mathbf{x}_N). \end{cases} \tag{2.41}$$

The solution of the system (2.41) can be retrieved using the proper numerical technique (e.g., the leapfrog or the Runge-Kutta method), with a suitable time step, smaller respect to the inverse of the plasma frequency.

Second formulation   The above formulation is straightforward, but excessively memory and time consuming to be implemented, considering that a further simplification may be done. In this type of geometry, each particle moves on a plane due to the presence of a central field of force; indeed a new formulation of the method is suggested, taking advantage on this fact. The initial coordinates $\mathbf{x}_i$ and momenta $\mathbf{p}_i$ of the system are generated on a 3D plane, and then the 2D coordinates $\mathbf{X}_i$ and $\mathbf{P}_i$ are set as

$$\begin{cases} \mathbf{X}_i = (r_i, 0), \qquad i = 1,2,...,N, \\[1.5ex] \mathbf{P}_i = \left(\mathbf{p}_i \cdot \dfrac{\mathbf{x}_i}{r_i}, \left| \mathbf{p}_i - \left(\mathbf{p}_i \cdot \dfrac{\mathbf{x}_i}{r_i} \right) \dfrac{\mathbf{x}_i}{r_i} \right| \right). \end{cases} \tag{2.42}$$

Apart from that, the method is identical to the previous formulation, but it adopts only 2D vectors. In particular, the radial position of the particles is calculated as $R_i = |\mathbf{X}_i|$ and the particles are ordered according to this variable. The electric field takes the value

$$\mathbf{E}_i = \left(\sum_{j=1}^{i-1} q_j + \tfrac{1}{2} q_i \right) \frac{\mathbf{X}_i}{R_i^3}, \tag{2.43}$$

and the evolution of the system is represented by the equations

$$\begin{cases} \dfrac{\mathrm{d}\mathbf{X}_i}{\mathrm{d}t} = \dfrac{\mathbf{P}_i}{m_i}, \\[2mm] \dfrac{\mathrm{d}\mathbf{P}_i}{\mathrm{d}t} = q_i \mathbf{E}_i \quad (\mathbf{X}_1, \mathbf{X}_2, ..., \mathbf{X}_N). \end{cases} \tag{2.44}$$

Third formulation The third formulation of the method starts with the definition of the Lagrangian for a single particle

$$\mathscr{L}(r, \varphi, \dot{r}, \dot{\varphi}, t) = \frac{m}{2} \left(\dot{r}^2 + r^2 \dot{\varphi}^2 \right) - q\Phi(r, t), \tag{2.45}$$

Φ is a central potential and depends on t due to the interaction with the other particles of the plasma. From Eq. 2.45 we can write the Hamiltonian

$$\mathscr{H}(r, \varphi, p_r, p_\varphi, t) = \frac{1}{2m} \left(p_r^2 + \frac{p_\varphi^2}{r^2} \right) + q\Phi(r, t), \tag{2.46}$$

and the motion equations

$$\begin{cases} \dfrac{\mathrm{d}r}{\mathrm{d}t} = \dfrac{p_r}{m}, & \dfrac{\mathrm{d}\varphi}{\mathrm{d}t} = \dfrac{p_\varphi}{mr^2}, \\[2mm] \dfrac{\mathrm{d}p_r}{\mathrm{d}t} = -q\dfrac{\partial \Phi}{\partial r} + \dfrac{p_\varphi^2}{mr^3}, & \dfrac{\mathrm{d}p_\varphi}{\mathrm{d}t} = 0. \end{cases} \tag{2.47}$$

Finally, as it is well known, the axial angular momentum, p_φ, is a constant of the motion for a central potential and in radial direction the motion is mostly one-dimensional. This fact implies the possibility of studying the dynamics of these systems in a third way. Starting again from the set $\{\mathbf{x}_i, \mathbf{p}_i\}$ we can calculate

$$r_i = |\mathbf{x}_i|, \qquad p_{r,i} = \mathbf{p}_i \cdot \frac{\mathbf{x}_i}{r_i}, \qquad p_{\varphi,i} = r_i \left| \mathbf{p}_i - p_{r,i} \frac{\mathbf{x}_i}{r_i} \right|. \tag{2.48}$$

Then, it is possible to calculate the radial electric field as

$$E_{r,i} = \left(\sum_{j=1}^{i-1} q_j + \tfrac{1}{2} q_i \right) \frac{1}{r_i^2} \tag{2.49}$$

21

where particles are sorted according to r_i. The equations of the motion become:

$$\begin{cases} \dfrac{\mathrm{d}r_i}{\mathrm{d}t} = \dfrac{p_{r,i}}{m_i}, \\ \dfrac{\mathrm{d}p_{r,i}}{\mathrm{d}t} = q_i E_{r,i}(r_1, r_2, ..., r_N) + \dfrac{p_{\varphi,i}^2}{m_i r_i^3}, \end{cases} \tag{2.50}$$

in which the $p_{\varphi,i}$'s are constants of the motion and the initial conditions fix them. Implementing this last formulation of the method the memory used and the computational effort are lower, compared to the other formulations. Nevertheless, special attention must be paid to the term $p_\varphi^2/(mr^3)$ in Eqs. (2.50), when $r \to 0$. Generally, the second formulation is the most used because it represents a good compromise concerning computational efficiency and simplicity.

Interaction between shells The problem under consideration has obviously spherical symmetry and it follows the choice of a spherical surface (a "shell") as a computational particle. The electric charge on the surface of the shell is distributed uniformly and the points on the surface move according to different trajectories, all of them with the same radial coordinate, $r(t)$, and the same angular momentum p_φ. We start by considering only a system made of two shells (having charge q_1 and q_2 and radii r_1 and r_2, with $r_1 < r_2$). The electric field in this case is

$$E(r) = \begin{cases} 0, & r < r_1, \\ \dfrac{q_1}{r^2}, & r_1 < r < r_2, \\ \dfrac{q_1 + q_2}{r^2}, & r > r_2, \end{cases} \tag{2.51}$$

and the electrostatic energy U can be readily computed, as

$$U(r_1, r_2) = \int_{\mathbb{R}^3} \frac{E^2}{8\pi} \, \mathrm{d}^3\mathbf{x} = \frac{q_1^2}{2r_1} + \frac{q_2^2 + 2q_1 q_2}{2r_2}. \tag{2.52}$$

If there is a variation δr_1 on r_1, the change of energy $-\delta U$ is evaluated as the work $qE_1 \cdot \delta r_1$ of the field on the shell itself. In other terms, we have:

$$E_1 = -\frac{1}{q_1} \frac{\partial U}{\partial r_1} = \frac{\frac{1}{2}q_1}{r_1^2}. \tag{2.53}$$

Similarly, the electric field acting on the second shell can be computed as

$$E_2 = -\frac{1}{q_2} \frac{\partial U}{\partial r_2} = \frac{q_1 + \frac{1}{2}q_2}{r_2^2}. \tag{2.54}$$

In both cases, the value of the electric field respects the rule "$\sum_{j=1}^{i-1} q_j + \frac{1}{2}q_i$", previously introduced in the formulation of the method.

Now let's consider the dynamics of the two shells: if r_1 remains smaller than r_2 it means that there is no crossing (i.e., no collisions) between shells. In this case

$$\frac{\mathrm{d}p_1}{\mathrm{d}t} = q_1 \frac{\frac{1}{2}q_1}{r_1^2} \quad , \quad \frac{\mathrm{d}p_2}{\mathrm{d}t} = q_2 \frac{q_1 + \frac{1}{2}q_2}{r_2^2}, \tag{2.55}$$

where we consider radial motion as the only possibility for the shells (i.e., $p_{\varphi,i} = 0$). The two equations (2.55) are rewritten as

$$\begin{cases} \dfrac{\mathrm{d}p_1}{\mathrm{d}t} = -\dfrac{\partial}{\partial r_1}\left(\dfrac{\frac{1}{2}q_1^2}{r_1}\right), \\ \dfrac{\mathrm{d}p_2}{\mathrm{d}t} = -\dfrac{\partial}{\partial r_2}\left(\dfrac{q_1 q_2 + \frac{1}{2}q_2^2}{r_2}\right), \end{cases} \tag{2.56}$$

from which we immediately obtain

$$\begin{cases} \dfrac{p_1^2}{2m_1} + \dfrac{\frac{1}{2}q_1^2}{r_1} = \mathrm{Const}, \\ \dfrac{p_2^2}{2m_2} + \dfrac{q_1 q_2 + \frac{1}{2}q_2^2}{r_2} = \mathrm{Const}. \end{cases} \tag{2.57}$$

Therefore, following the expansion of the two shells, the asymptotic kinetic energy for $t \to +\infty$, $\mathcal{E}(+\infty)$, can be readily computed, as

$$\begin{cases} \mathcal{E}_1(+\infty) = \mathcal{E}_1(0) + \dfrac{\frac{1}{2}q_1^2}{r_1(0)}, \\ \mathcal{E}_2(+\infty) = \mathcal{E}_2(0) + \dfrac{q_1 q_2 + \frac{1}{2}q_2^2}{r_2(0)}. \end{cases} \tag{2.58}$$

Let's now consider the case of collision instead. Defining $t = t_c$ as the instant when $r_1(t_c) = r_2(t_c) = r_c$, for $t > t_c$ the shell #1 overtakes the shell #2. Therefore, Eqs. (2.55-2.57) are valid only for $t < t_c$. For $t > t_c$, Eqs. (2.55) must be replaced by

$$\begin{cases} \dfrac{\mathrm{d}p_1}{\mathrm{d}t} = q_1 \dfrac{q_2 + \frac{1}{2}q_1}{r_1^2}, \\ \dfrac{\mathrm{d}p_2}{\mathrm{d}t} = q_2 \dfrac{\frac{1}{2}q_2}{r_2^2}, \end{cases} \tag{2.59}$$

simply exchanging indices 1 and 2, from which we finally obtain

$$\begin{cases} \dfrac{p_1^2}{2m_1} + \dfrac{q_1 q_2 + \frac{1}{2}q_1^2}{r_1} = \mathrm{Const}, \\ \dfrac{p_2^2}{2m_2} + \dfrac{\frac{1}{2}q_2^2}{r_2} = \mathrm{Const}. \end{cases} \tag{2.60}$$

23

In order to evaluate the new asymptotic energy when we have a collision, $\mathcal{E}'(+\infty)$, both Eqs. (2.57) (for $t < t_c$) and Eqs. (2.60) must be taken into account:

$$\begin{cases} \mathcal{E}'_1(t_c) = \mathcal{E}_1(0) + \dfrac{\frac{1}{2}q_1^2}{r_1} - \dfrac{\frac{1}{2}q_1^2}{r_c} = \mathcal{E}_1(+\infty) - \dfrac{\frac{1}{2}q_1^2}{r_c}, \\[2ex] \mathcal{E}'_2(t_c) = \mathcal{E}_2(0) + \dfrac{q_1q_2 + \frac{1}{2}q_2^2}{r_2} - \dfrac{q_1q_2 + \frac{1}{2}q_2^2}{r_c} = \mathcal{E}_2(+\infty) - \dfrac{q_1q_2 + \frac{1}{2}q_2^2}{r_c}, \end{cases} \qquad (2.61)$$

and

$$\begin{cases} \mathcal{E}'_1(+\infty) = \mathcal{E}'_1(t_c) + \dfrac{q_1q_2 + \frac{1}{2}q_1^2}{r_c} = \mathcal{E}_1(+\infty) + \dfrac{q_1q_2}{r_c}, \\[2ex] \mathcal{E}'_2(+\infty) = \mathcal{E}'_2(t_c) + \dfrac{\frac{1}{2}q_2^2}{r_c} = \mathcal{E}_2(+\infty) - \dfrac{q_1q_2}{r_c}. \end{cases} \qquad (2.62)$$

It means that when a collision takes place, an increase $\Delta\mathcal{E} = q_1q_2/r_c$ in the energy of the shell #1 is produced, and it corresponds in a decrease $-\Delta\mathcal{E}$ for the shell #2. In a typical case of plasma expansion, the energy $\mathcal{E}$ of a shell stays in the order of qQ/R, being Q the total charge and R the initial plasma radius. So, with $\Delta\mathcal{E} \sim q^2/R$ for a single collision, we can conclude that the "plasma parameter" $\Delta\mathcal{E}/\mathcal{E}$ for a set on N shells will be of the order of $q/Q = 1/N$. Finally, for typical values of the number of computational particles, the system can always be considered collisionless.

Validation of the code   To test the reliability of the numerical method a simple case of electrons expansion in a spherical plasma is introduced, considering the ions at rest during all the transient. Both electrons and positive ions are initially distributed uniformly in a sphere of radius R and at $t = 0$ electrons have Maxwellian velocity distribution with temperature T. Reference results have been obtained running the simulation with a very high number of shells ($N \simeq 10^6$) and then a comparison with the solution using a reduced ($N \simeq 10^3$) number of particles has been performed. Since the initial distribution of electrons in terms of positions and velocities was generated using random numbers, for a small number of shells the results will depend on the particular choice of the phase spaces. It follows that the same calculation has been repeated for 300 times (with different initial conditions, all corresponding to the same physical situation) in order to compute the mean behavior and the distribution of the physical quantities (as performed in (D'Angola et al., 2014)). In Figs. 2.10 and 2.11 are reported respectively the time evolution of the number of electrons inside the ion sphere (i.e., with $r \leq R$) and of the fraction of trapped electrons (i.e., with total energy $\frac{p^2}{2m} - e\Phi(r) \leq 0$). As we can observe, the shell method provides excellent results, even with a reduced set of particles.

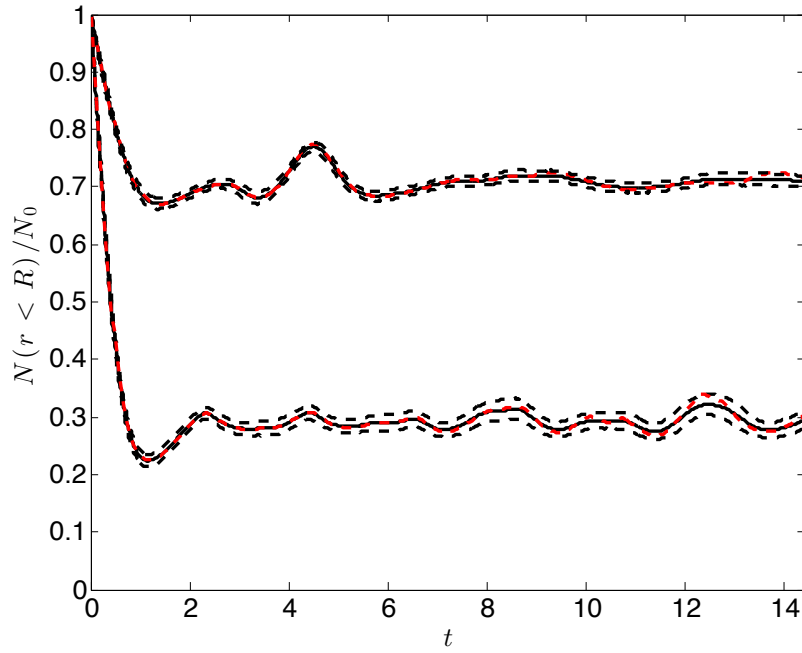Figure 2.10: Time evolution of the fraction of electrons inside the ion sphere for two different normalized temperature, $T = 0.0431, 0.431$. For each value of T, ensemble averages (full black line) and standard deviation ranges (dashed black lines) are reported for $N = 10^3$ shells and 300 simulations with different initial conditions, together with reference results provided by a simulation with $N = 10^6$ shells (dashed red line). Adapted from B. Peiretti Paradisi, E. Boella, A. D'Angola and G. Coppa, Computer Physics Communications, 2017.
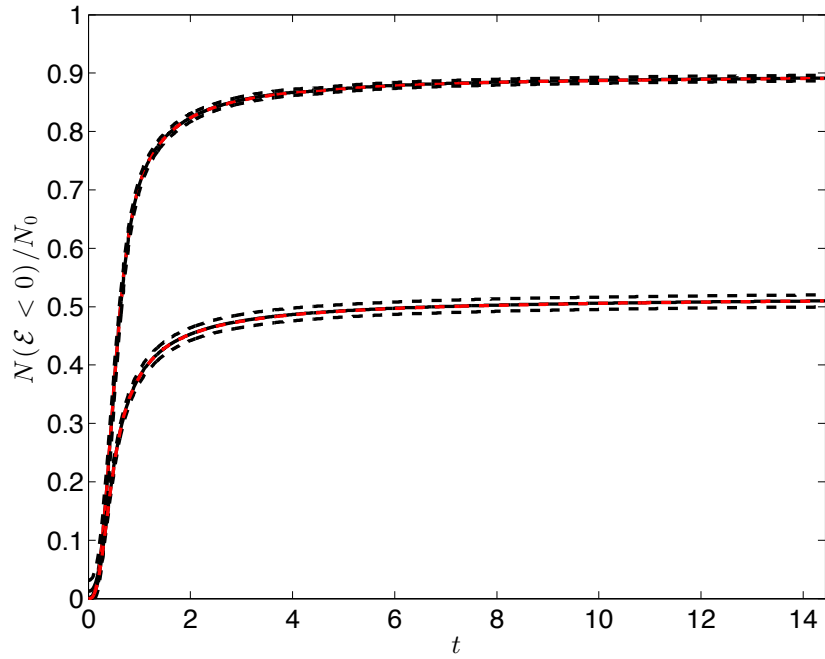
Figure 2.11: Time evolution of the fraction of trapped electrons for the same case of Fig. 2.10. Adapted from B. Peiretti Paradisi, E. Boella, A. D'Angola and G. Coppa, Computer Physics Communications, 2017.

Chapter 3

Coulomb explosion of cylindrical targets

The aim of the present chapter is the presentation and explanation in details of the three numerical methods developed to study the expansion of a thin slab, in case of uniform charge density or heterogeneous double layer targets. Numerical simulations are needed to investigate the phenomenon in this geometry because a theoretical model is not possible. The first approach was a 3D N-body algorithm, the so-called Soft-Spheres method, which is necessary when there is no possibility of making assumptions on the geometry of the system, see in Sec. 3.1. We developed two other methods useful in case the original system presents some symmetries. For example, when a laser pulse ionizes the considered slab with a circular spot, the area interested by the mechanism of Coulomb explosion will be cylindrical. The geometry of the system presents an axial symmetry and we decide to develop another N-body method: the ring method, Sec. 3.2. Here computational particles are rings which are coaxial with the system symmetry axis; they change radial and axial position during the simulation, conserving their annular shape. In the end, a 2D Particle-In-Cell (PIC) code was developed to follow the expansion in cylindrical coordinates, all details in Sec. 3.3. In particular, the in-house code has a grid which enlarges in time to properly study the phenomenon. In the following chapter, the methods are validated in simple geometries (spherical systems) by comparison with the analytic solution, giving an excellent agreement.

Declarations   Part of the work described in this Chapter was also previously published in the following publication, further reported in Appendix of this thesis: B. Peiretti Paradisi, E. Boella, A. D'Angola and G. Coppa, Gridless simulation of collisionless systems with high degree of symmetry, Computer Physics Communications, 2017.

27

3.1 The Soft-Spheres method

The soft-spheres method is an N-body algorithm, which can simulate a 3D system, without any hypothesis on the symmetry of the real situation. The number of computational particles used, N_p, is much order of magnitude smaller than the number of real particles, N_0, but the collisionless of the system must be maintained. The coupling parameter, ε_p, of two point-like computational particles both of charge q and mass m presents the same structure of the one for a real plasma, ε, and can be written as:

$$\varepsilon_p = \frac{q^2/\bar{d}_p}{mv^2},\tag{3.1}$$

where v is the mean velocity between two particles. In Eq. (3.1), $\bar{d}_p = \bar{d}N^{1/3}$ is the mean distance between computational particles (while $\bar{d}$ is the distance between real particles) and $N = N_0/N_p$ is the number of real particles constituting a computational one. Equation (3.1) becomes $\varepsilon_p = \varepsilon \cdot (N_0/N_p)^{2/3}$ showing that the collisionality increases dramatically if the number of computational particles is too low. To solve this issue soft-spheres have a finite radius r_s to ensure a limited value of electrostatic potential when $r < r_s$. In this case, the coupling parameter is

$$\varepsilon_p = \varepsilon \mathcal{V}(\bar{d}_p)N\bar{d},\tag{3.2}$$

being $\mathcal{V}$ the new potential energy of interaction between two soft-spheres, for unitary charges. In particular, to ensure that the system is collisionless, the worst case is examined: two completely overlapped soft-spheres, i.e., with $\mathcal{V} = \mathcal{V}(0)$. Therefore the function $\mathcal{V}$ must have a structure such that the condition below is respected

$$\mathcal{V}(0)N\bar{d} \lesssim 1.\tag{3.3}$$

The interaction energy $U_{12} = \mathcal{V}q^2$ between two spheres of uniform charge density is a function of the distance between the centers:

$$U_{12}(r) = \frac{1}{2}\int \mathrm{d}^3 x' \frac{q}{\frac{4}{3}\pi r_s^3}\Phi_s(|\mathbf{x} - \mathbf{x'}|);\tag{3.4}$$

where Φ_s is the electrostatic potential generated by a sphere uniformly charged:

$$\Phi_S(r) = \begin{cases} \dfrac{q}{r_s}\left[\dfrac{3}{2} - \dfrac{1}{2}\left(\dfrac{r}{r_s}\right)^2\right], & r < r_s \\[2em] \dfrac{q}{r}, & r > r_s. \end{cases}\tag{3.5}$$

28

Finally, after calculating the integral in Eq. (3.4) (the end of the section reports all the details), one obtains

$$U_{12}(r) = q^2 \begin{cases} \dfrac{1}{r_s}\left[\dfrac{6}{5} - \dfrac{1}{2}\left(\dfrac{r}{r_s}\right)^2 + \dfrac{3}{16}\left(\dfrac{r}{r_s}\right)^3 - \dfrac{1}{160}\left(\dfrac{r}{r_s}\right)^5\right], & r < 2r_s \\[2ex] \dfrac{1}{r}, & r > 2r_s. \end{cases}$$

(3.6)

Obviously, $U_{12}(r)$ for $r < 2r_s$ is different from $q\Phi_S$, which is the energy of a sphere interacting with a point charge, as shown in Fig.(3.1a), where $q\Phi_S$ and U_{12} are compared. The two functions coincide when the two particles do not overlap each others, $r > 2r_s$. Then from Eq.(3.6) the Coulomb force between two soft-spheres is obtained, as:

$$\mathbf{F}_{12}(r) = -\frac{\partial U_{12}}{\partial r}\mathbf{e}_r = q^2 \begin{cases} \dfrac{1}{r_s^2}\left[\dfrac{r}{r_s} - \dfrac{9}{16}\left(\dfrac{r}{r_s}\right)^2 - \dfrac{1}{32}\left(\dfrac{r}{r_s}\right)^4\right]\mathbf{e}_r, & r < r_s \\[2ex] \dfrac{1}{r^2}\mathbf{e}_r, & r > 2r_s; \end{cases}$$

(3.7)

the force F_{12} is compared with qE_s in Fig. (3.1b). Taking into account the potential energy of the soft-spheres (from Eq. 3.6), in case of $r = 0$, $\mathcal{V}(0) = 6/(5r_s)$ and the constraint on the collisionality of the computational system reduces to

$$\frac{N_0 \bar{d}}{N_p r_s} \lesssim 1.$$

(3.8)

Details of the numerical method In the present method, the center of each sphere has three degrees of freedom for moving, while the radius r_s remains constant and it is the same for each computational particle. The appropriate choice of r_s is fundamental, in order to respect the condition on the collisionality (Eq.3.8) of the original system. At the beginning of the simulation, N_p computational particles are created with different positions and velocity $\{\mathbf{x}_p, \mathbf{v}_p\}$ in a way that reconstructs the initial density. The charge-to-mass ratio of a computational particle is the same as the real one and also systems composed by mixtures of different species can be analyzed. At each time step, the equations of motion are discretized with a Runge-Kutta method of fourth order and the velocity and the center of each sphere are updated. Equations of motion for the soft sphere are

$$\begin{cases} \dfrac{\mathrm{d}\mathbf{x}_p}{\mathrm{d}t} = \dfrac{\mathbf{P}_p}{m} \\[2ex] \dfrac{\mathrm{d}\mathbf{p}_p}{\mathrm{d}t} = q\mathbf{E}(\mathbf{x}_p), \end{cases}$$
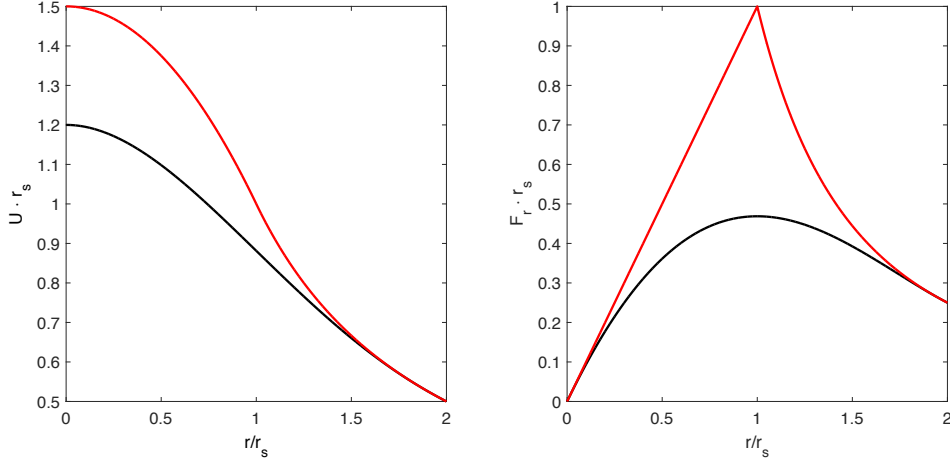
(3.9)

29

Figure 3.1: a) Comparison between the interaction potential energy U_{12} (Eq. 3.6) of two soft-spheres (black curve) unitary charged and the electrostatic potential of one sphere (red curve). b) Radial Coulomb force between two soft-spheres (Eq. 3.7, black curve) compared with the electric field of one sphere unitary charged (red curve). In both cases, the two curves coincide when the distance between the centers of the two soft-spheres is $r > 2r_s$ (no overlapping between the two spheres).

and the electric field acting on the i-th sphere is

$$\mathbf{E}(\mathbf{x}_p) = \sum_{j \neq i} \mathbf{E}_{p'}(\mathbf{x}_p); \tag{3.10}$$

where $\mathbf{E}_{p'}(\mathbf{x}_p)$ is given by

$$\mathbf{E}_{p'}(\mathbf{x}_p) = \begin{cases} \dfrac{q_{p'}}{r_s^3} \left[1 - \dfrac{9}{16} \dfrac{r_{pp'}}{r_s} - \dfrac{1}{32} \left(\dfrac{r_{pp'}}{r_s} \right)^3 \right] (\mathbf{x}_p - \mathbf{x}_{p'}), & r_{pp'} < 2r_s \\ \\ \dfrac{q_{p'}}{r_{pp'}^3} (\mathbf{x}_p - \mathbf{x}_{p'}), & r_{pp'} > 2r_s; \end{cases} \tag{3.11}$$

being $q_{p'}$ the charge of the sphere interacting with i-th sphere and $r_{pp'}$ the distance between the centers of the two spheres.

Energy and momentum conservation The soft-spheres algorithm is a mass conserving model, and also the conservation of energy and momentum of the system is respected. In particular, Fig. 3.2 shows the evolution of the total kinetic (red line) and potential energy (blue line) of the system, at different time steps, for a sampling spherical cluster composed by Hydrogen and Deuterium. The total energy (black line) of the system remains constant, respecting the conservation of energy. The conservation of momentum on the three directions, for a mixture of two species, should be:

$$\mathbf{p} = \sum_{i=1}^{N_s} \mathbf{p}_i + \sum_{j=1}^{N_f} \mathbf{p}_j = 0, \qquad (3.12)$$

being N_s and N_f the number of slow and fast spheres, constituting the system.
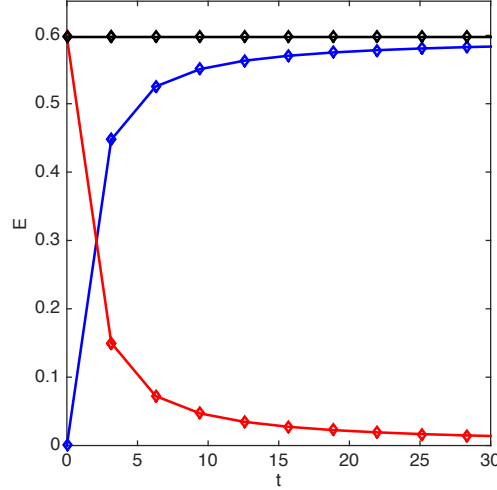
Figure 3.2: Evolution of total energies of the system, for a spherical cluster composed by Hydrogen and Deuterium. The kinetic energy is in red and potential energy in blue; the mechanical energy (black line) remains constant, being the method energy conserving.

Computing the evolution in time of the momentum, p_α, in the three directions, it has some fluctuations around the zero. To estimate if the variations of the function are small enough, verifying the conservation of momentum, a comparison is needed. An average momentum is computed, on the $\alpha - th$ component, as:

$$<p_\alpha> = \frac{1}{N_p} \left(\sum_{i=1}^{N_s} p_{i,\alpha} + \sum_{j=1}^{N_f} p_{j,\alpha} \right) ; \qquad (3.13)$$

thus, the modulus of the average momentum is simply

$$< p >= \sqrt{\sum_{\alpha=1}^{3} < p_\alpha >^2}.$$

(3.14)

The average total momentum $< p >$ is compared with a modified average kinetic energy of the system, $< K_e >$, defined as:

$$< K_e >= \frac{2(N_s m_s + N_f m_f)}{N_p} \left(\sum_{i=1}^{N_s} \frac{|\mathbf{p}_i|^2}{2m_s} + \sum_{j=1}^{N_f} \frac{|\mathbf{p}_j|^2}{2m_f} \right).$$

(3.15)

In order to respect the conservation of momentum, the square of the average kinetic energy should be much larger respect to the average momentum:

$$< p > \ll \sqrt{< K_e >};$$

(3.16)

Figure (3.3) shows that the inequality in Eq. (3.16) is satisfied at each time step of the simulation.
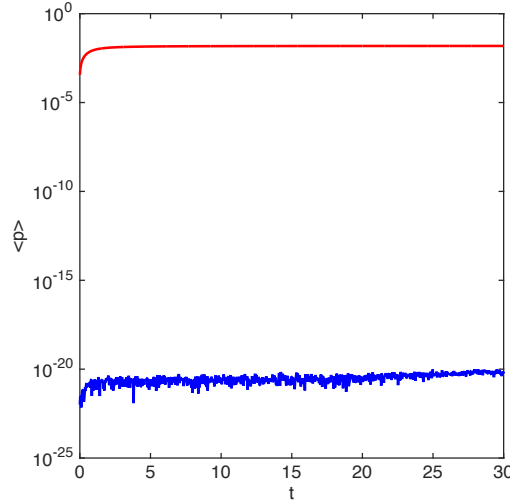
Figure 3.3: Comparison between the total average momentum $< p >$ (blue line) and the function $\sqrt{< K_e >}$ (red line). The momentum remains many order of magnitude lower than the square of the average kinetic energy.

Validation of the code in spherical geometry To proof the validity of the method, soft-spheres have been used in a simple spherical geometry, showing perfect agreement with the analytic solution. The expansion of a spherical cluster with uniform initial charge density is considered, as theoretically described in Sec. 2.1. One of the aims is also the comparison between two different initial particle loading:

1. the particles are loaded equally spaced in a cube, with the side corresponding to the diameter of the sphere. Then, the particles outside the sphere of initial radius R are rejected,

2. the particles are randomly loaded inside the sphere, always respecting the uniformity of the charge distribution;

in both cases, the initial velocities of the ions are set as zero.

   The first test consists in the discrete calculation of the initial potential energy of the sphere, considering an increasing number of particles, with both particle loading methods. The electrostatic energy, U_s, of a sphere of charge Q and radius R is given by

$$U_s = \frac{3}{5}\frac{Q^2}{R} \tag{3.17}$$

where in case of unitary charge and radius, we simply obtain the value $U_s = 3/5$. Starting from this value it is possible to compare the result obtained from the N-body method, to clarify the accuracy of depicting the initial charge density and set a suitable number of computational particles. In Fig. 3.4 the two particle loading methods are compared and we can notice that the error on the calculation of the electrostatic energy is negligible also with a few numbers of particle, while the random method gives the best result. Once the initial particle loadings are tested, the expansion of a uniform spherical cluster is presented; in this example, we try to use a small number of soft-spheres to balance the computational cost of the method. The simulation runs with only 5000 soft-spheres and the radius of each soft-sphere is fixed as a fraction of the radius of the cluster: $r_s = R/20$, respecting Eq. (3.8). The initial radius R, total charge Q and mass M of the cluster are fixed at unitary values. Fig. 3.5, shows the phase space at different times, multiples of the plasma period T_p defined as

$$T_p = \frac{2\pi}{\omega_p} = \sqrt{\frac{m\pi}{nq}} \tag{3.18}$$

being q the charge of a single sphere, m its mass and n the initial density. Fig. 3.7 shows the kinetic energy spectrum of the ions, in case of equally spaced particles on the initial axial sections of the sphere. On the other hand, Figs. 3.6 and 3.8 present the same situation with ions randomly distributed on the initial volume of the sphere. All the results are in perfect agreement with the analytic solution, (Boella et al., 2016), even if in the case of ions randomly distributed the histogram
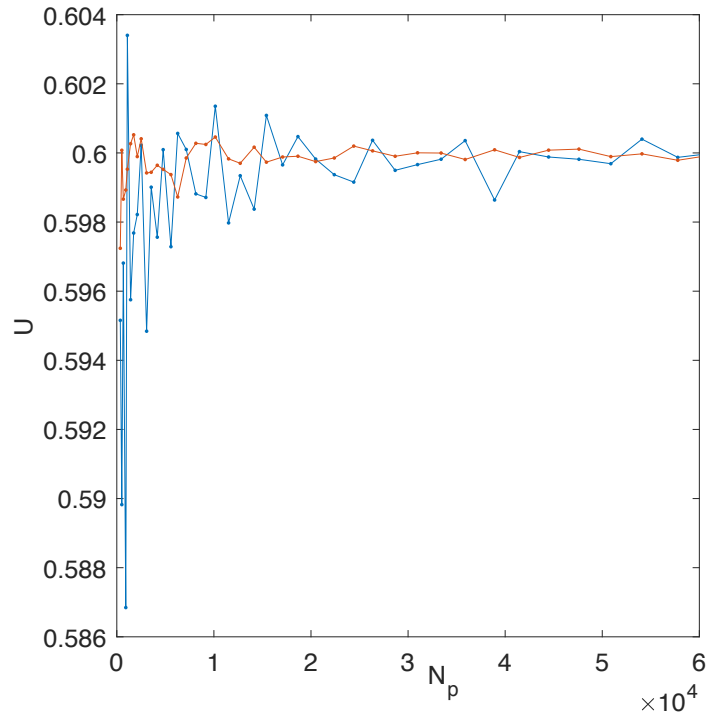
Figure 3.4: Initial potential energy in a spherical cluster with uniform charge density, calculated with a different number of computational particles and the two loading methods. Random (red line), equally spaced (blue line).

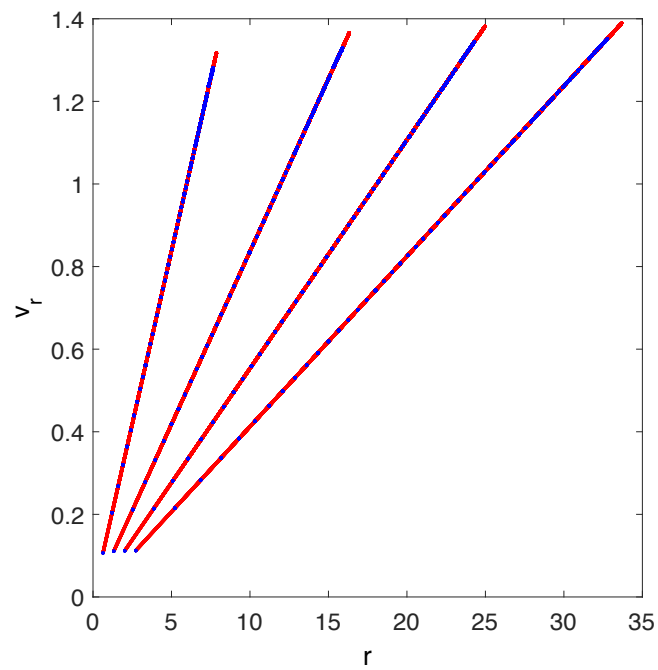used to depict the spectrum is more precise.

Figure 3.5: Phase space evolution for a spherical cluster at different times $[T_p, 2T_p, 3T_p, 4T_p]$ with initial particle loading equally spaced. Results from the Soft-spheres method (blue dots) are compared with the analytic solution (red line).
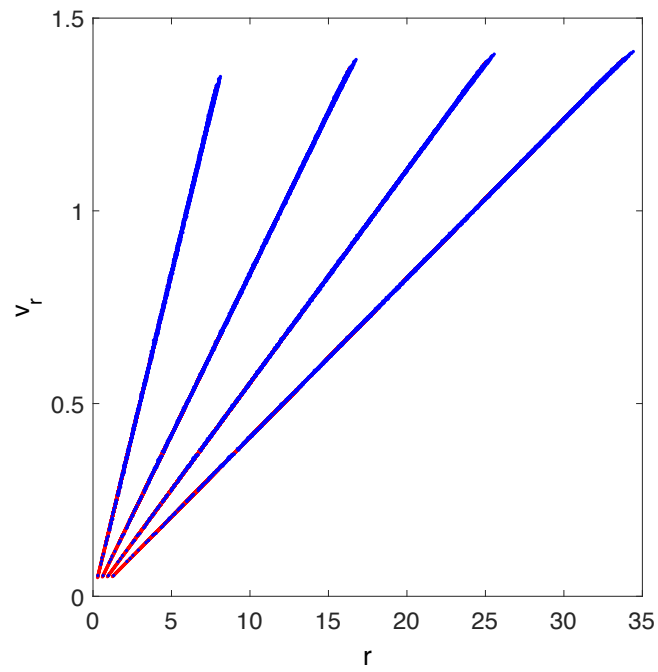
Figure 3.6: Same of Fig. 3.5 but with ions randomly distributed at $t = 0$. Results from the Soft-spheres method (blue dots) are compared with the analytic solution (red line).
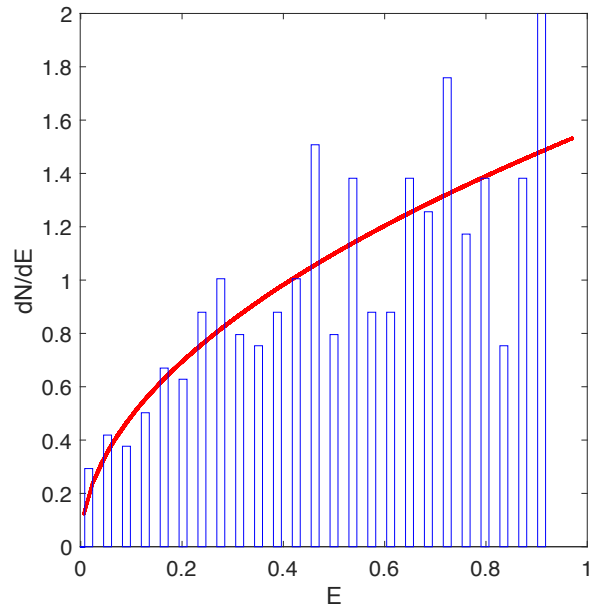
Figure 3.7: Kinetic energy spectrum of the ions inside the same sphere of Fig. 3.5, the histogram in blue represents the result of the Soft-spheres method compared with the analytic solution (red line).
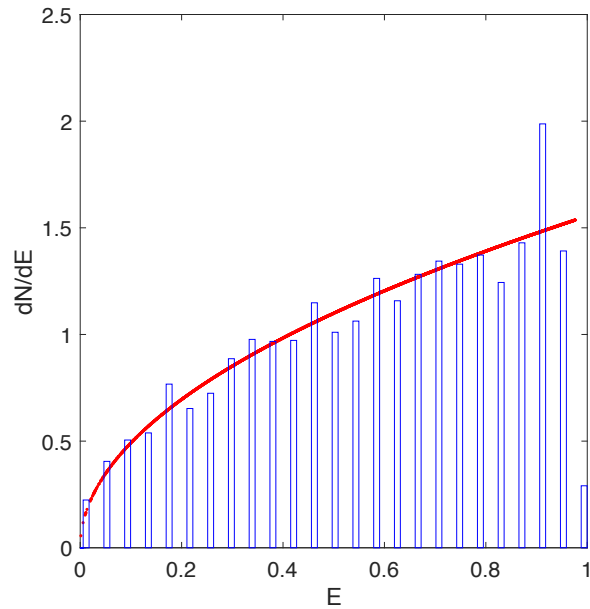
Figure 3.8: Kinetic energy spectrum of the ions inside the same sphere of Fig. 3.6, the histogram in blue represents the result of the Soft-spheres method compared with the analytic solution (red line).

37

3.1.1 Interaction potential energy between two soft spheres

This section treats the derivation of the potential energy, U_{12}, between two soft spheres, uniformly charged, both with radius r_s. The definition in polar coordinates is

$$U_{12}(d) = \rho \int_0^{r_s} r^2 \, \mathrm{d}\, r \int_{-1}^1 \mathrm{d}\, \mu \int_0^{2\pi} \Phi_{S_1}(r_{12}) \, \mathrm{d}\, \phi \qquad (3.19)$$

being ρ the charge density, $r_{12} = (d^2 + r^2 - 2\mu rd)^{1/2}$ the generic distance between the center of the sphere S_1 and a point P inside S_2, d the centers' distance, r the distance between P and the center of S_2 and $\mu = \cos(\theta)$ the cosine of the angle between d and r, as can be seen in Figs 3.10 and 3.9. The potential $\Phi_S(r_{12})$ is the potential of a charged sphere, given by Eq. (3.5). When $d > 2r_s$, $\Phi_{S_1} = q/r_{12}$ and Eq. (3.19) reduces to the potential energy of interaction between two point particles: $U_{12} = q^2/d$. When the two spheres start overlapping, it is necessary to split the integral (3.19), depending on the position of the fraction of S_2 respect to S_1, inside or outside it.

Case $r_s < d < 2r_s$

As the two spheres partially overlapping, two zone are considered, delimited by the critical radius $r = d - r_s$ (Fig. 3.9). In this case, the integral is split as:

$$U_{12} = 2\pi\rho \left[\int_0^{d-r_s} r^2 \, \mathrm{d}\, r \int_{-1}^1 \mathrm{d}\, \mu \Phi_{S_1}(r_{12}) + \int_{d-r_s}^{r_s} r^2 \, \mathrm{d}\, r \int_{-1}^1 \mathrm{d}\, \mu \Phi_{S_1}(r_{12}) \right]. \qquad (3.20)$$

In a zone with $r < d-r_s$, for each angle θ, the point P is outside S_1 and consequently, $r_{12} > r_s$: the potential is simply $\Phi_{S_1} = q/r_{12}$. On the other hand, if P is in the portion of S_2 with $r > d - r_s$ the integral with respect to μ has also to be split, because if $\theta > \tilde{\theta}$ (green zone Fig.3.9) one has $r > r_s$, vice-versa with $\theta < \tilde{\theta}$. In summary, Eq. (3.20) becomes

$$U_{12} = 2\pi\rho q \left\{ \int_0^{d-r_s} r^2 \, \mathrm{d}\, r \int_{-1}^1 \frac{\mathrm{d}\, \mu}{(d^2 + r^2 - 2\mu rd)^{1/2}} + \right. \qquad (3.21)$$

$$\left. + \int_{d-r_s}^{r_s} r^2 \, \mathrm{d}\, r \left[\int_{-1}^{\tilde{\mu}} \frac{\mathrm{d}\, \mu}{(d^2 + r^2 - 2\mu rd)^{1/2}} + \int_{\tilde{\mu}}^1 \frac{3r_s^2 - d^2 - r^2 + 2\mu rd}{2r_s^3} \mathrm{d}\, \mu \right] \right\}$$

being

$$\tilde{\mu} = \cos\tilde{\theta} = \frac{d^2 + r^2 - r_s^2}{2rd}, \qquad (3.22)$$
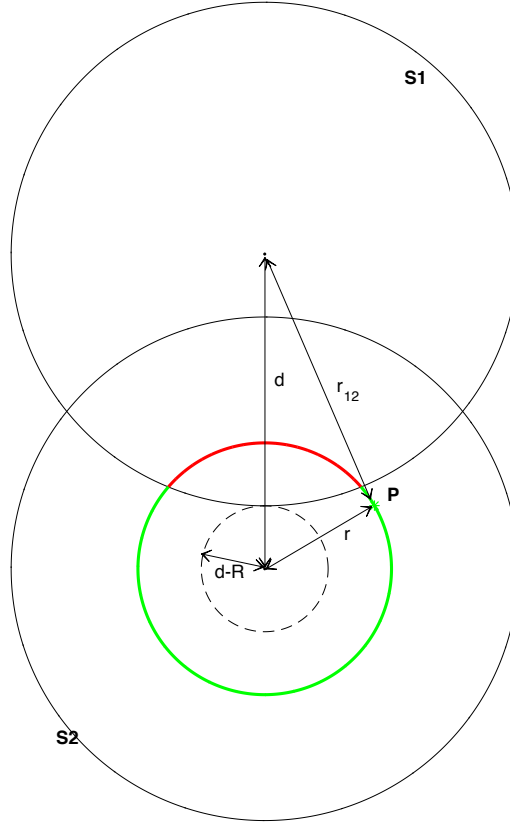
(the angle $\tilde{\theta}$ is such that $r_{12} = r_s$).

Figure 3.9: Overlapping of two soft spheres, with the centers' distance respecting the following condition $r_s < d < 2r_s$. Both spheres have radius r_s.

Case $d < r_s$

In this case, the center of S_2 is inside S_1, as shown in Fig. 3.10 and the critical radius on which the integral is split becomes $r = r_s - d$

$$U_{12} = 2\pi\rho \left[\int_0^{r_s-d} r^2 \, \mathrm{d}\,r \int_{-1}^1 \mathrm{d}\,\mu \Phi_{S_1}(r_{12}) + \int_{r_s-d}^{r_s} r^2 \, \mathrm{d}\,r \int_{-1}^1 \mathrm{d}\,\mu \Phi_{S_1}(r_{12}) \right], \quad (3.23)$$

where in the case $r < r_s - d$, for each angle θ, $r_{12} < r_s$ then the potential Φ_{S_1} is the inner one of the system (3.5). On the contrary, with $r > r_s - d$, the integral
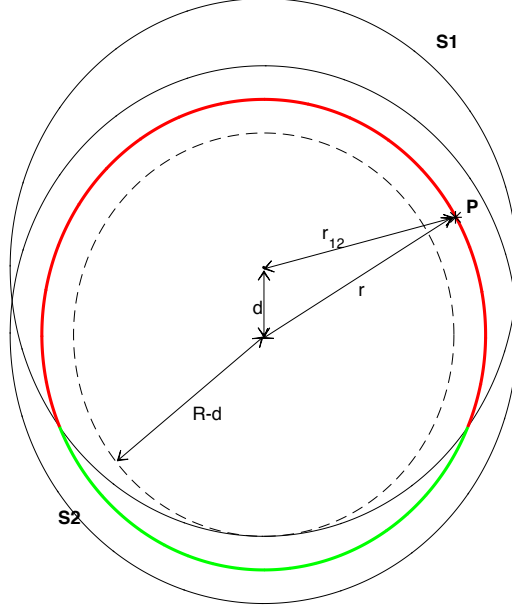
Figure 3.10: Same configuration of Fig. 3.9, but with $d < r_s$.

splits also on the angle. In particular, for $\theta < \tilde{\theta}$ (red zone in Fig.3.10) S_2 overlaps S_1, vice-versa for $\theta < \tilde{\theta}$ (green zone Fig.3.10). Consequently, the integral becomes

$$U_{12} = 2\pi\rho q \left\{ \int_0^{r_s-d} r^2 \, \mathrm{d}\, r \int_{-1}^{1} \left(\frac{3}{2r_s} - \frac{d^2 + r^2 - 2\mu r d}{2r_s^3} \right) \mathrm{d}\, \mu + \right. \tag{3.24}$$
$$\left. + \int_{r_s-d}^{r_s} r^2 \, \mathrm{d}\, r \left[\int_{-1}^{\tilde{\mu}} \frac{\mathrm{d}\, \mu}{(d^2 + r^2 - 2\mu r d)^{1/2}} + \int_{\tilde{\mu}}^{1} \frac{3r_s^2 - d^2 - r^2 + 2\mu r d}{2r_s^3} \, \mathrm{d}\, \mu \right] \right\}.$$

In both cases (3.21) e (3.24), also with different integrals, the solution is the same

$$U_{12}(d) = \frac{q^2}{r_s} \left[\frac{6}{5} - \frac{1}{2} \left(\frac{d}{r_s} \right)^2 + \frac{3}{16} \left(\frac{d}{r_s} \right)^3 - \frac{1}{160} \left(\frac{d}{r_s} \right)^5 \right]. \tag{3.25}$$

Eq. (3.25) is finally the interaction potential energy between two soft spheres, in function of the distance d between the two centers.

3.2   The ring method

Developing an N-body code, in case of axial symmetry, the computational particle used has the shape of a ring. More precisely, we consider a torus having a circular cross-section (of radius a). All the tori are constructed around the same axis of symmetry, which is the z-axis, and their position is defined by a radius, R_i, and an axial coordinate, z_i (as in Fig. 3.11). When we take into account N tori, the electrostatic energy of the system can be written as:

$$U = \frac{1}{2} \sum_{i \neq j} q_i q_j \varphi_{ring}(R_i, R_j, z_i - z_j) + \sum_{i=1}^{N} q_i^2 U_{torus}(R_i, a), \qquad (3.26)$$

where we have

- q_i as the total charge of a torus

- $\varphi_{ring}(r, R, z)$ as the potential generated by a unit charge distributed on a torus with $a = 0$, that we call ring, of radius R laying on the xy plane in a point of polar coordinates (r, z),

- $U_{torus}(R, a)$ as the potential energy of a torus of unitary charge.

We start evaluating the potential of an infinitesimal ring defined by its total charge q and radius R, acting on a generic point $P(x, y, z)$. A fraction of the ring has infinitesimal charge $dq = q/(2\pi)d\theta$; therefore the potential on P is

$$\Phi_{ring \to P} = \int_{Vol} \frac{q}{r_{PP'}} \frac{\mathrm{d}\,\theta}{2\pi}. \qquad (3.27)$$

Fig. 3.12 displays the symmetry of the problem: in this case, the point P can be taken for simplicity with the coordinates $P = (r, 0, z)$ and the potential created by the ring will be the same for each point with coordinates $(r \sin\theta, r \cos\theta, z)$ for a generic angle θ and fixed r, z. One point of the ring, called P', has coordinates $P' = (R \sin\theta, R \cos\theta, 0)$ and the distance $r_{PP'}$ is made explicit as

$$r_{PP'} = (r^2 + R^2 + z^2 - 2rR \cos\theta)^{1/2}. \qquad (3.28)$$

At this point, our idea is to lead back to a known function for the calculus of the integral (3.27); expressing $\cos\theta$ in function of $\alpha = \frac{\theta}{2} - \frac{\pi}{2}$, the integral becomes

$$\Phi_{ring} = \frac{q}{s(r, R, z)} \int_0^{\pi/2} \frac{\mathrm{d}\,\alpha}{(1 - \xi \sin^2 \alpha)^{1/2}}, \qquad (3.29)$$

where ξ and s are defined as

$$\xi = \frac{4Rr}{s^2(r, R, z)} \quad \text{e} \quad s = [(r + R)^2 + z^2]^{1/2}. \qquad (3.30)$$

Finally, the ring potential is expressed as

$$\Phi_{ring}(r, R, z) = \frac{2q}{\pi} \frac{K[\xi]}{s(r, R, z)}, \tag{3.31}$$

being $K[\xi]$ the complete elliptic integral of the first kind

$$K[\xi] = \int_0^{\pi/2} \frac{d\,\alpha}{(1 - \xi \sin^2 \alpha)^{1/2}}. \tag{3.32}$$

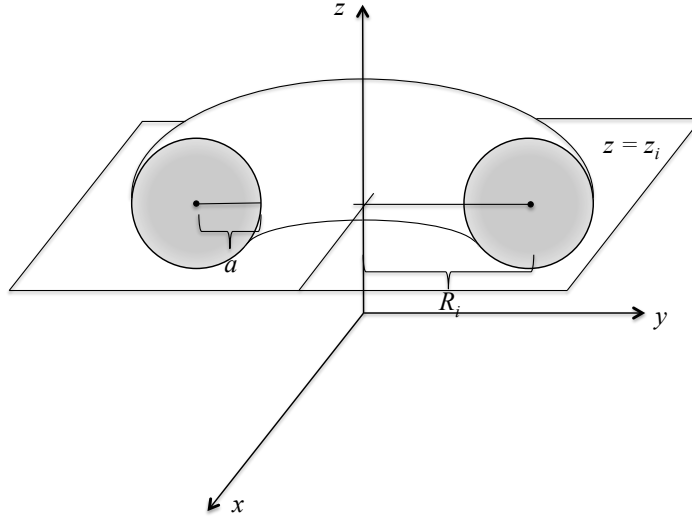The following section reports in details the calculation of $U_{torus}(R, a)$, but for the

Figure 3.11: Scheme of a torus. Adapted from B. Peiretti Paradisi, E. Boella, A. D'Angola and G. Coppa, Computer Physics Communications, 2017.

case of interest in which $a \ll R$, we obtain:

$$U_{torus}(R, a) \sim -\frac{1}{2\pi R} \left[\log\left(\frac{a}{8R}\right) - \frac{1}{4} \right]. \tag{3.33}$$

When we refer to a ring with $a \to 0$ it can be noticed that the expression in Eq.(3.33) diverges and this is the reason why computational particles are chosen as tori and not simply rings. On the other hand, when we calculate the interaction energy between tori, we use the value of φ_{ring}, as we suppose that in the case $a \ll R$ the energy of two tori or two rings is necessarily the same.

Now, we derive the equations of the motion for the set of rings. The kinetic energy of the system is considered

$$\sum_{i=1}^N \frac{m_i}{2} \left(\dot{R}_i^2 + \dot{z}_i^2 + R_i^2 \dot{\varphi}_i^2 \right), \tag{3.34}$$
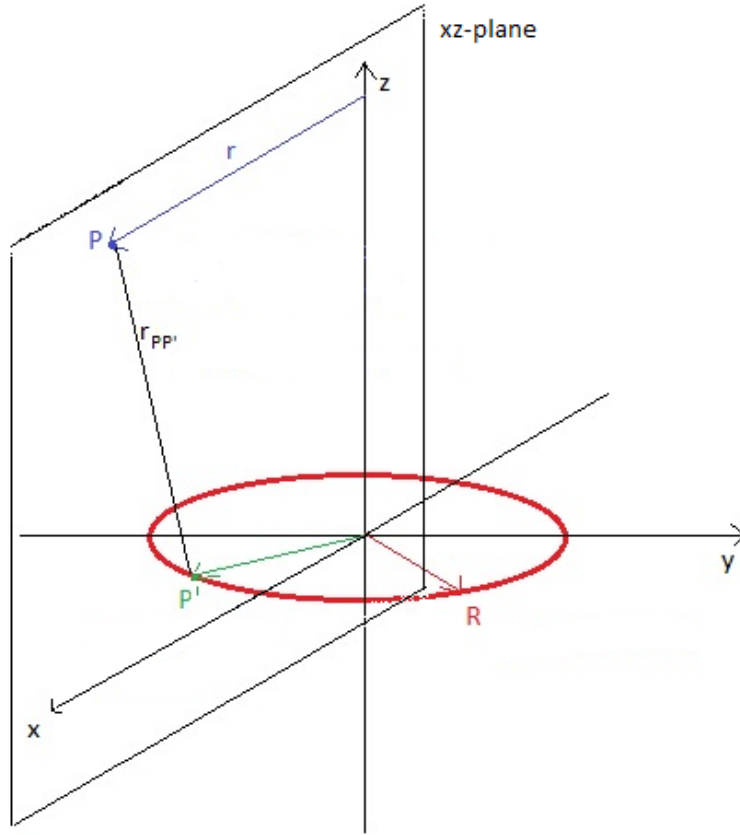
Figure 3.12: Geometry to solve the integral. Adapted from B. Peiretti Paradisi, E. Boella, A. D'Angola and G. Coppa, Computer Physics Communications, 2017.

in order to derive the Lagrangian. By introducing the momenta $p_{R,i}$, $p_{z,i}$, and $p_{\varphi,i}$:

$$p_{R,i} = m_i \dot{R}_i, \qquad\qquad p_{z,i} = m_i \dot{z}_i, \qquad\qquad p_{\varphi,i} = m_i R_i^2 \dot{\varphi}_i, \qquad (3.35)$$

we finally obtain the Hamiltonian $\mathscr{H}$ of the N interacting rings as:

$$\mathscr{H} = \sum_{i=1}^{N} \frac{1}{2m_i} \left(p_{R,i}^2 + p_{z,i}^2 + \frac{p_{\varphi,i}^2}{R_i^2} \right) +$$

$$+\frac{1}{2} \sum_{i \neq j} q_i q_j \varphi_{ring}(R_i, R_j, z_i - z_j) + \sum_{i=1}^{N} q_i^2 U_{torus}(R_i, a), \qquad (3.36)$$

43

and the equations of the motion are:

$$
\begin{cases}
\dfrac{\mathrm{d}\,R_\alpha}{\mathrm{d}\,t} = \dfrac{p_{R,\alpha}}{m_\alpha}, \qquad \dfrac{\mathrm{d}\,z_\alpha}{\mathrm{d}\,t} = \dfrac{p_{z,\alpha}}{m_\alpha}, \\[3mm]
\dfrac{\mathrm{d}\,p_{R,\alpha}}{\mathrm{d}\,t} = \dfrac{p_{\varphi,\alpha}^2}{m_\alpha R_\alpha^3} - \sum_{\beta\neq\alpha} q_\alpha q_\beta \dfrac{\partial}{\partial R_\alpha}\varphi_{ring}(R_\alpha, R_\beta, z_\alpha - z_\beta) - q_\alpha^2 \dfrac{\partial}{\partial R_\alpha} U_{torus}(R_\alpha; a), \\[3mm]
\dfrac{\mathrm{d}\,p_{z,\alpha}}{\mathrm{d}\,t} = - \sum_{\beta\neq\alpha} q_\alpha q_\beta \dfrac{\partial}{\partial z_\alpha}\varphi_{ring}(R_\alpha, R_\beta, z_\alpha - z_\beta).
\end{cases}
$$

$$(3.37)$$

We notice that the angular momenta $p_{\varphi,\alpha}$ are constants of the motion. The partial derivatives of φ_{ring} can be readily computed using the expression for the derivative of the elliptic integral of first kind $K[x]$:

$$
\frac{\mathrm{d}\,K[x]}{\mathrm{d}\,x} = \frac{E[x] - (1-x)K[x]}{2x(1-x)},
\tag{3.38}
$$

being $E[x] = \int_0^{\pi/2}(1 - x\sin^2\alpha)^{1/2}\mathrm{d}\alpha$ the complete elliptic integral of the second kind (Abramowitz and Stegun, 1965).

Validation of the code in spherical geometry   To test its reliability and accuracy, we employ the ring method to simulate the expansion of an ion sphere of uniform density, for which we have available the analytic solution. The physical quantities are always normalized to obtain a total radius of the sphere $R = 1$ and total unitary charge and mass. The initial distribution of the rings with coordinates $\{R_i, z_i\}$ has been conceived in two different ways, considering that the initial domain $[R, z]$ is a half circle of radius R_0:

1. the initial domain is divided into a number N of small squares, each corresponding to the cross-section of a ring,

2. taking a set of $\{R_i, z_i\}$ in a random way, but in order to obtain a uniform charge density.

The radius a_i of the section of each torus has been determined as proportional to R_i, i.e., $a_i = k \cdot R_i$. We choose the constant k by imposing the potential energy of the set of the rings equal to the exact value of the energy of the sphere. Figures 3.13, 3.14 and 3.15, 3.16 refer to method 1 and method 2, for ring loading, respectively. Figs. 3.13 and 3.14 show the time evolution of the phase-space distribution, comparing the results from the ring method with the analytical behavior. Figures 3.15 and 3.16 display the evolution in time of the total kinetic energy of the ions, $\mathcal{E} = \sum_{i=1}^{N} \frac{m_i}{2}\mathbf{v}_i^2(t)$; in addition, the behavior of $[\mathcal{E}^{(t)} - \mathcal{E}_r(t)]/\mathcal{E}$ is also depicted,
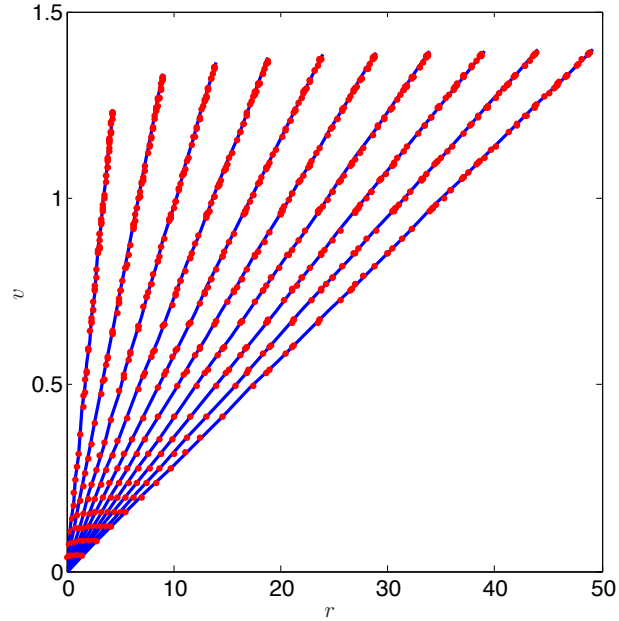
Figure 3.13: Phase-space distribution at different times ($t = 4 \div 36$) of a spherical ion plasma in the case of ring-loading with method 1. Results obtained with the ring method (red dots) are compared with the analytic solution (blue lines). Adapted from B. Peiretti Paradisi, E. Boella, A. D'Angola and G. Coppa, Computer Physics Communications, 2017.

where $\mathcal{E}_r(t) = \sum_{i=1}^{N} \frac{m_i}{2} \left[\mathbf{v}_i^2(t) \cdot \mathbf{e}_{r,i}(t) \right]$ is the kinetic energy due to the motion in radial direction. Obviously, in the exact solution $\mathcal{E}_r(t) \equiv \mathcal{E}(t)$, so we expect a value of $\left| \frac{\mathcal{E} - \mathcal{E}_r(t)}{\mathcal{E}} \right| \ll 1$. All the numerical results obtained are in excellent agreement with the theory.
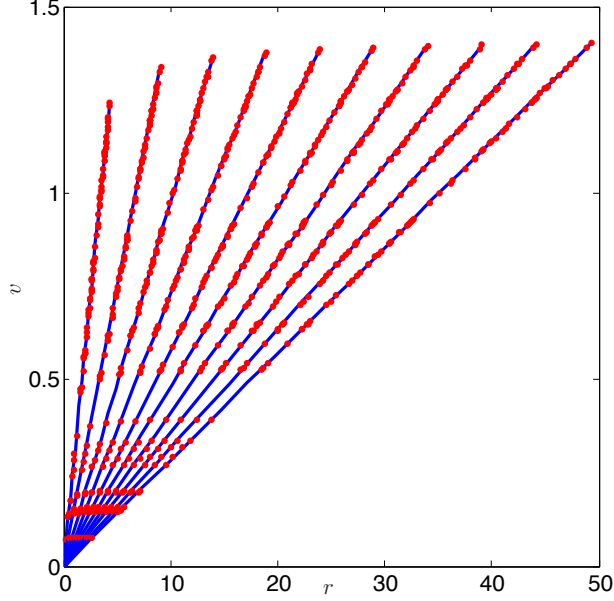
Figure 3.14: Same as Fig. 3.13 in the case of ring loading with method 2 ($t = 4 \div 36$). Results obtained with the ring method (red dots) are compared with the analytic solutions (blue lines). Adapted from B. Peiretti Paradisi, E. Boella, A. D'Angola and G. Coppa, Computer Physics Communications, 2017.

3.2.1 Electrostatic energy of a torus with $a \ll R$

To calculate the electrostatic energy of a torus, we start by dividing the cross-section S in a large number of subdomains, as in Fig. 3.17. Each of them acted an electrostatic potential that we approximate as the one of a ring. Calling Δq_i the discrete charge of the i-th subdomain and by $\varphi_{ring}(\mathbf{x}_i; \mathbf{x}_j)$ the potential in $\mathbf{x}_i$ due to a unitary charge in $\mathbf{x}_j$, the energy of the torus is given by

$$U \simeq \frac{1}{2} \sum_{i \neq j} \Delta q_i \Delta q_j \varphi_{ring}(\mathbf{x}_i, \mathbf{x}_j). \tag{3.39}$$

Taking the limit case, when the size of the subdomains tends to zero, the sum becomes an integral

$$U = \int_{\mathscr{S}} \mathrm{d}^2 x_Q \int_{\mathscr{S}} \mathrm{d}^2 x_P \sigma(\mathbf{x}_Q) \sigma(\mathbf{x}_P) \varphi_{ring}(\mathbf{x}_P, \mathbf{x}_Q), \tag{3.40}$$

where $\sigma(\mathbf{x})$ represents the charge density for a unit cross-section. Supposing that the torus is uniformly charged and in the particular case with $a \ll R$, we can assume

$$\sigma \simeq \frac{q}{\pi a^2} = \text{Const.} \tag{3.41}$$

46
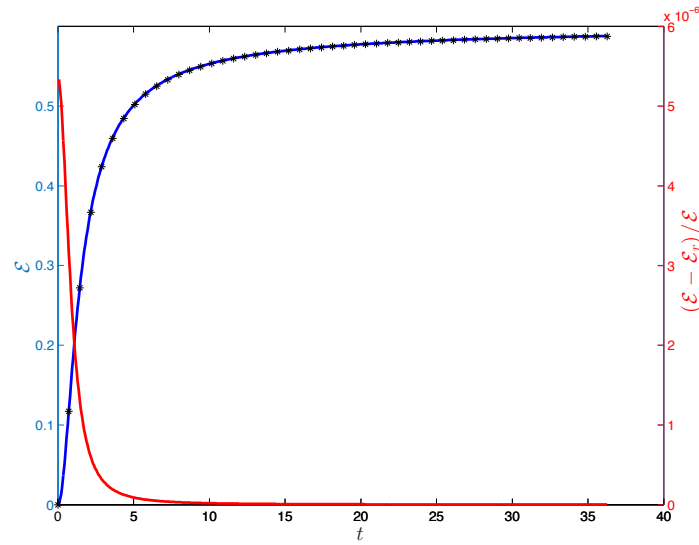
Figure 3.15: Time evolution of the total kinetic energy of the ions (blue line) and of the fraction of the perpendicular kinetic energy (red line) obtained with the ring method for the same case of Fig. 3.13 (method 1 for ring loading). Results obtained with the ring method are compared with the analytic solutions (black stars). Adapted from B. Peiretti Paradisi, E. Boella, A. D'Angola and G. Coppa, Computer Physics Communications, 2017.
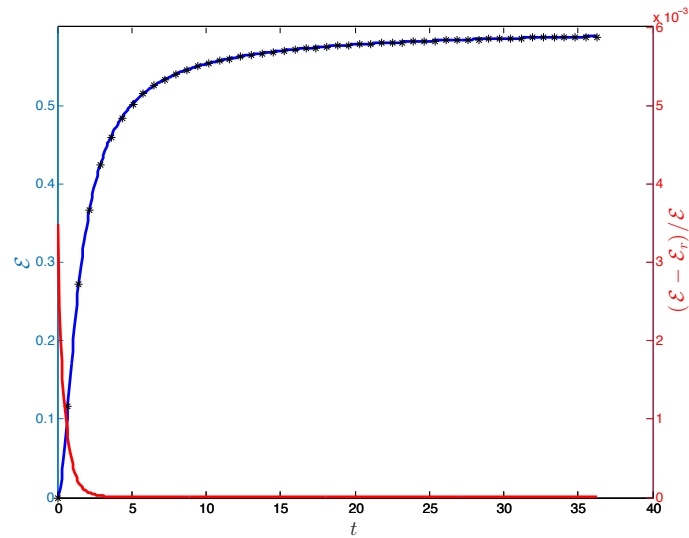
Figure 3.16: Same as Fig. 3.15, using method 2 for ring loading. Excellent agreement between the ring method (solid lines) and the analytic solution (black stars). Adapted from B. Peiretti Paradisi, E. Boella, A. D'Angola and G. Coppa, Computer Physics Communications, 2017.

47
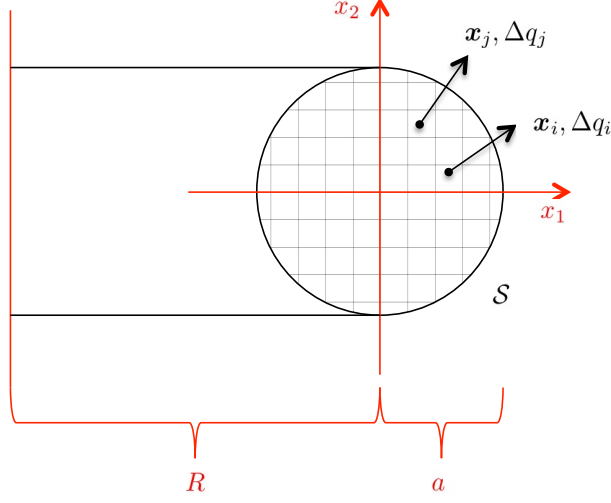
Figure 3.17: Cross section of a torus and coordinates employed in the calculation. Adapted from B. Peiretti Paradisi, E. Boella, A. D'Angola and G. Coppa, Computer Physics Communications, 2017.

In order to evaluate $\varphi_{ring}(\mathbf{x}_P, \mathbf{x}_Q)$, the parameters s and ξ, defined in Eq. (3.30), must be rewritten in this case. One has:

$$\xi = \frac{4(R + x_{1,P})(R + x_{1,Q})}{s^2},$$

$$s = \left[(R + x_{1,P} + R + x_{1,Q})^2 + (x_{2,P} - x_{2,Q})^2\right]^{1/2}. \tag{3.42}$$

Introducing the quantity $\eta = R + \frac{x_{1,P} + x_{1,Q}}{2}$, such that $R + x_{1,P} = \eta + \frac{x_{1,P} - x_{1,Q}}{2}$, $R + x_{1,Q} = \eta - \frac{x_{1,P} - x_{1,Q}}{2}$, the variable ξ can be written as:

$$\xi = \frac{1 - \left(\frac{x_{1,P} - x_{1,Q}}{2\eta}\right)^2}{1 + \left(\frac{x_{2,P} - x_{2,Q}}{2\eta}\right)^2} \simeq 1 - \left(\frac{r_{PQ}}{2R}\right)^2, \tag{3.43}$$

with $r_{PQ}^2 = (\mathbf{x}_P - \mathbf{x}_Q)^2$. Indeed, η is much larger with respect to the quantity $|x_{2,P} - x_{2,Q}| \leq a$, so the approximation $\frac{1}{1+\epsilon} \simeq 1 - \epsilon$ can be used; moreover, η can be approximated by R. We introduce the approximation for the asymptotic behavior of $K[\xi]$ when $\xi \to 1$:

$$K[\xi] \underset{\xi \to 1}{\sim} -\frac{1}{2}\log(1 - \xi) + \log 4, \tag{3.44}$$

and assuming that $s \simeq 2R$, the following expression for $\varphi_{ring}(\mathbf{x}_P, \mathbf{x}_Q)$ is finally obtained:

$$\varphi_{ring}(\mathbf{x}_P, \mathbf{x}_Q) = -\frac{1}{\pi R} \log\left(\frac{r_{PQ}}{8R}\right). \tag{3.45}$$

Equation (3.45) can be substituted in Eq. (3.39), which can be rewritten as

$$U = \frac{\sigma^2}{2} \int_{\mathscr{S}} \mathrm{d}^2 x_Q \varphi_{torus}(\mathbf{x}_Q), \tag{3.46}$$

being

$$\varphi_{torus}(\mathbf{x}_Q) = -\frac{1}{\pi R} \int_{\mathscr{S}} \mathrm{d}^2 x_P \log\left(\frac{r_{PQ}}{8R}\right). \tag{3.47}$$

In the case of $\mathbf{x}_Q = 0$, φ_{torus} is easily evaluated:

$$\varphi_{torus}(0) = -\frac{1}{\pi R} \int_0^a 2\pi r dr \log\left(\frac{r}{8R}\right) = -\frac{a^2}{R}\left[\log\left(\frac{a}{8R}\right) - \frac{1}{2}\right]. \tag{3.48}$$

To calculate φ_{torus} for a generic $\mathbf{x}_Q \in S$, we can start by highlighting that $\log(r_{PQ})$ is proportional to the Green function for the two-dimensional Poisson's equation:

$$\nabla_Q^2 \log r_{PQ} = 2\pi\delta\left(\mathbf{x}_Q - \mathbf{x}_P\right). \tag{3.49}$$

So, by applying the Laplacian operator ∇_Q^2 to Eq. (3.47), we obtain

$$\nabla_Q^2 \varphi_{torus} = -\frac{1}{\pi R} \int_S \mathrm{d}^2 x_P \cdot 2\pi\delta\left(\mathbf{x}_P - \mathbf{x}_Q\right) = -\frac{2}{R}. \tag{3.50}$$

In the particular symmetry of the problem, φ_{torus} is a function of $r_Q = |\mathbf{x}_Q|$, and the Laplacian operator becomes $\nabla_Q^2 = \frac{1}{r_Q}\frac{\mathrm{d}}{\mathrm{d}\,r_Q} r_Q \frac{\mathrm{d}}{\mathrm{d}\,r_Q}$. Therefore, Eq. (3.50) can be readily solved, so obtaining

$$\varphi_{torus}(\mathbf{r}_Q) = \varphi_{torus}(0) - \frac{r_Q^2}{2R}. \tag{3.51}$$

In the end, the energy of the torus can be calculated solving the integral in Eq. (3.46):

$$U = \frac{q^2}{2\pi^2 a^4} \cdot 2\pi \int_0^a r_Q \mathrm{d}r_Q \left[\varphi_{torus}(0) - \frac{r_Q^2}{2R}\right] = -\frac{q^2}{2\pi R}\left[\log\left(\frac{a}{8R}\right) - \frac{1}{4}\right]. \tag{3.52}$$

Equation (3.52) provides very accurate results in the case $a \ll R$. Making a comparison between Eq. (3.52) and the value of U obtained from numerical integration of Eq. (3.39), the relative error obtained is less than 0.5% for $a/R < 0.2$. A similar formula (except for the term -1/4) has been deduced in a concise, brilliant way in (Landau and Lifshitz, 1984) by using the technique of asymptotic matching.

3.3 EXPICYL: the PIC method for expansions

A two-dimensional cylindric (r, z) Particle-In-Cell has been developed and used to describe the rapid expansion of plasmas due to the interaction of a high-power laser pulse with solid targets. Thus, the computational domain has not a fixed size, but it follows the expansion, increasing its dimensions. The method is a 2D model, with axial symmetry, and each cell has an annular shape with size Δr and Δz, in cylindrical coordinates. The grid starts with an initial radius R_0 and initial height H_0, containing all the computational particles. Fig. 3.18 presents an example of a typical initial grid. At each time step, because of the expansion mechanism, some particles take values of r_j, z_j larger than the domain limits, which are recomputed. The number of grid cell (N_r, N_z) remains constant and the new size of the domain, and of each cell, becomes:

$$
\begin{aligned}
R_{new} &= \max(\mathbf{r}_i) \\
H_{new} &= \max(\mathbf{z}_i) \\
\Delta r_{new} &= R_{new}/N_r \\
\Delta z_{new} &= H_{new}/N_z.
\end{aligned}
\tag{3.53}
$$

There are some particular situations in which a particle takes a high value of acceleration during one-time step will also be pushed so far from the other ones and, respecting Eqs. (3.53), the risk is to have a vast new grid, with a lot of empty cells near the boundaries of the domain. In this case, there is the possibility to exclude from the simulation the small fraction of particles so far from the center of the domain, because it does not influence the electrostatic potential of the system. Thus, Eq. (3.53) is replaced, excluding from the domain the particles with a radial or axial position greater than a calculated limit. In the radial direction, the limit is calculated as $R_{new} = \overline{R_e} + N_{\sigma_E}\sigma_E$, being $\overline{R_e}$ and σ_E the average and the standard deviation of the radial distribution of the computational particles and N_{σ_E} a real factor such as $N_{\sigma_E} \leq [\max(r_j) - \overline{R_e}]/\sigma_E$. The same criterion is adopted for the axial direction, calculating H_{new} and the new origin of the cylinder.

3.3.1 Poisson solver

To solve Poisson equation, the finite volume method is used, in cylindrical coordinates with axial symmetry; the aim is to obtain the value of the electric potential on the center of each grid cell. Here we have Poisson's equation in Gaussian unit

$$
\nabla^2 \Phi = -4\pi\rho,
\tag{3.54}
$$

being ρ the charge density and stating $\partial\Phi/\partial\theta = 0$ in cylindrical coordinates, we obtain

$$
\frac{1}{r}\frac{\partial\Phi}{\partial r} + \frac{\partial^2\Phi}{\partial r^2} + \frac{\partial^2\Phi}{\partial z^2} = -4\pi\rho_Q.
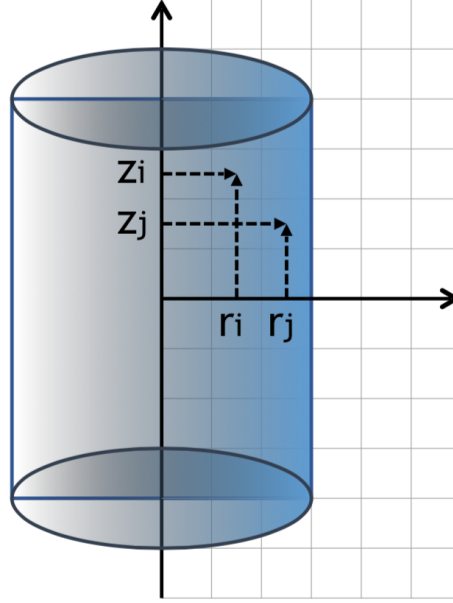\tag{3.55}
$$

Figure 3.18: Schematic representation of the grid for the EXPICYL method, with a center cell j and a boundary cell i highlighted.

Integrating the general form (3.54) on a volume of interest and applying the divergence theorem $\int_V \nabla \cdot F dV = \oint_{\partial V} F \cdot dS$ at the left-hand side of the equation, we get as a result

$$\oint_S \nabla \Phi dS = -4\pi \tilde{\rho} \Delta V; \tag{3.56}$$

considering an average value of density, $\tilde{\rho}$, on the right-hand side and being ΔV the elementary volume of a grid cell. In the finite volume method, the integral is approximated as a sum

$$\sum_{i=1}^{6} (\nabla \Phi)_i \cdot (\hat{n} \mathrm{dA})_i = -4\pi \tilde{\rho} \Delta V, \tag{3.57}$$

and applying the obtained result on a central grid cell, as in Fig. 3.19, we obtain

$$\frac{\Phi_N - \Phi_O}{\Delta z} S_N + \frac{\Phi_S - \Phi_O}{\Delta z} S_S + \frac{\Phi_W - \Phi_O}{\Delta r} S_W + \frac{\Phi_E - \Phi_O}{\Delta r} S_E = -4\pi \tilde{\rho}_O \Delta V. \tag{3.58}$$

We can rewrite Eq. (3.58) making explicit the expression of the surface and the volume of the cell in the cylinder, obtaining in matrix notation

$$
\begin{aligned}
\Phi_{i-1,j} 2r_j \Delta r^2 + \Phi_{i+1,j} 2r_j \Delta r^2 + \Phi_{i,j-1} 2(r_j - \Delta r/2)\Delta z^2 \quad & \tag{3.59} \\
+ \Phi_{i,j+1} 2(r_j + \Delta r/2)\Delta z^2 + \Phi_{i,j}(-4r_j(\Delta r^2 + \Delta z^2)) \quad = \quad & -8\pi \tilde{\rho}_{i,j} r_j \Delta r^2 \Delta z^2
\end{aligned}
$$
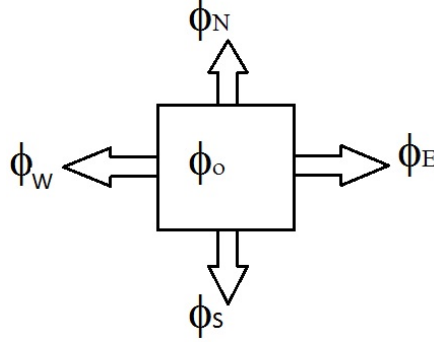
Figure 3.19: Central elementary cell of the domain.

valid for a central cell of the domain with distance r_j from the cylinder axis. Referring at the boundary conditions, we have two different situations: on three sides of the domain the grid has external cells, but on one side we are on the cylinder axis and a hypothesis on the symmetry of the electric field must be applied as a boundary condition. Regarding the external cells, the electrostatic potential $\Phi(r, z)$ has been obtained by the superposition of the analytical potentials generated by charged particles distributed on rings (Boella et al., 2018). In fact, the electrostatic potential is calculated at the boundaries of the computational domain by summing the contributions due to all the rings, each of them represented by a computational cell, centered in (r_j, z_j) and with charge density obtained with weighted particle-grid projection; in this way, "exact" boundary conditions are provided for the solver of the Poisson's equation. In particular, the exact electric potential on a ring is given by two contributions (see Chapter 3.2):

$$\Phi_a = \sum_{k=0, k \neq a}^{N_a} \Phi_{k \to a} + \Phi_{a \to a}, \tag{3.60}$$

being $\Phi_{k \to a}$ the potential of an infinitesimal ring of radius $r_k = R_k$ acting on another ring of radius r_a:

$$\Phi_{k \to a} = \frac{2q}{\pi} \frac{K[m]}{[(r_a + R_k)^2 + (z_a - z_k)^2]^{1/2}} \text{ e } m = \frac{4R_k r_a}{(r_a + R_k)^2 + \Delta z^2} \tag{3.61}$$

with $K[m]$ complete elliptic integral of the first kind. $\Phi_{a \to a}$ is the potential actuated by the ring on itself and it has been obtained considering the average potential of a torus of charge q, with radius r_a and radius of the circular section a:

$$\Phi_{a \to a} = -\frac{q}{2\pi r_a} \left[\log \left(\frac{a}{2r_a} \right) - \frac{1}{4} \right]. \tag{3.62}$$

On the cylinder axis, we have mentioned that the hypothesis is that the electric field vanishes. In this case, the balance given by Eq. 3.60, will be slightly different because referring to Fig. 3.20, $\Phi_W - \Phi_O = 0$.
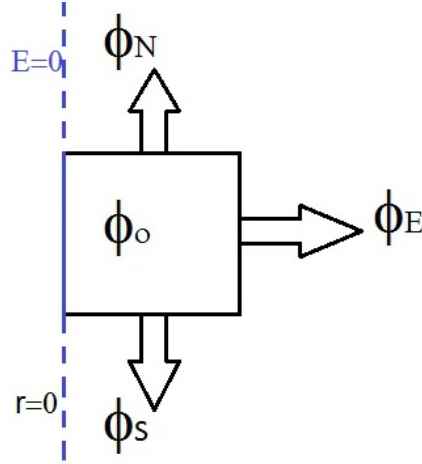

Figure 3.20: Grid cell on the axis of the cylinder, symmetry condition of the electric field.

The balance on the grid cell becomes

$$\Phi_{i-1,j}2r_j\Delta r^2 + \Phi_{i+1,j}2r_j\Delta r^2 + \Phi_{i,j+1}2(r_j + \Delta r/2)\Delta z^2 \qquad (3.63)$$
$$+\Phi_{i,j}(-4r_j\Delta r^2 - 2(r_j + \Delta r/2)\Delta z^2)) = -8\pi\tilde{\rho}_{i,j}r_j\Delta r^2\Delta z^2.$$

Validation of the code To test the convergence of the algorithm a comparison with the analytic solution for the expansion of a spherical Hydrogen cluster ($R = 1$ and $Q = 1$) is made. The relative error in the computation of the final kinetic energy is evaluated, varying some characteristic parameters of the model, as the total number of cells and the number of computational particles. Tab. 3.1 shows the standard deviation of the energy spectra, σ_E, respect to the analytic value, in function of N_p, with two different grid configurations. When the grid is sharper σ_E is smaller, but in both cases it remains under 3%, with $N_p > 1e5$. In Tab. 3.1 also simulations times are shown, in function of the number of computational particles.

Grid cells: $N_r = 50$ and $N_z = 80$		
N_p	$\sigma_E(t = t_f)$	$t_{sim}[s]$
1e4	0.1115	542
5e5	0.0601	550
1e5	0.0293	590
5e5	0.0222	1070
1e6	0.0200	1719
Grid cells: $N_r = 100$ and $N_z = 130$		
N_p	$\sigma_E(t = t_f)$	$t_{sim}[s]$
1e4	0.0790	2015
5e5	0.0428	2020
1e5	0.0299	2051
5e5	0.0151	2547
1e6	0.0103	3129

Table 3.1: Simulation times and standard deviation on the energy spectra, computed in comparison with the analytic solution, in function of the number of computational particles N_p, with different grid configurations.

In order to compare results obtained by using the PIC code with the corresponding reference solutions of the Vlasov-Poisson model, the electron expansion in a spherical plasma (Peano et al., 2006) is studied. Reference solutions of the Vlasov-Poisson model are obtained by using the shell method presented in Sec. 2.3, and results are compared with calculations performed by using a high number of particles ($N \simeq 10^6$) and averaging over different initial conditions (all corresponding to the same physical situation (D'Angola et al., 2014)). In particular, initial electron positions and velocities (r_{p0}, v_{p0}) are assigned by using pseudorandom numbers to simulate a uniform spatial distribution inside a sphere of radius R and a Gaussian distribution in velocity with a variance $(k_B T)^{1/2}$. Positive ions are initially distributed uniformly in the sphere and considered at rest during all the transient. In all the calculations, the total charge, the total mass of the plasma and the initial radius R are all equal to 1 by using a suitable normalization. In Figures 3.21 the time

evolution of the number of electrons inside the ion sphere (i.e., with $r \leq R$) are reported, for three different electron initial velocities, showing the excellent agreement between the PIC and the shell method.
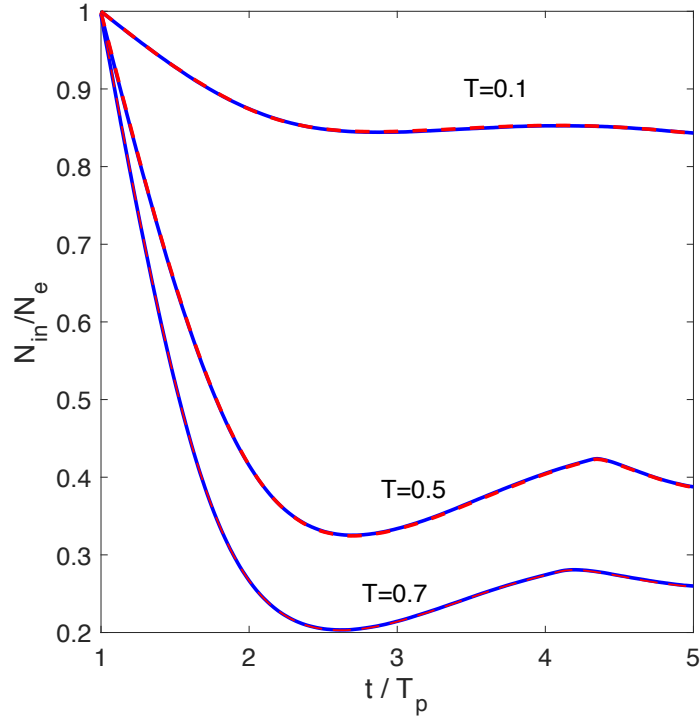

Figure 3.21: Time evolution of the fraction of electrons inside the ion sphere for three initial normalized temperature, $T = 0.1, 0.5, 0.7$. Results obtained by the PIC code with $N_p = 2 \cdot 10^5$ (red dotted line) are compared with the reference solution provided by the shell method (full blue line).

3.4   Coulomb explosion of a thin slab

In this section, a simplified analysis of the expansion of a cylindrical slab made by two ion species is considered, with the approximation of no overtakings between particles of the same type. All the parameters characteristic of the mixture are defined as in Chapter 2.2. Figure 3.22 displays the ideal situation of a slab made by a mixture of two species during the expansion at a generic $t = t'$, considering as direction of motion only the z-axis, perpendicular to the surface of the slab. Inside the region delimited by the axial coordinate $[-F_s, F_s]$ we can find a mixture of the two species and the electric field has a linear behavior. On the other hand, in the region between the two frontlines, $F_s < z < F_f$, only the light/fast species is present. The 1D approximation, which was perfectly suitable in the spherical cluster configuration, must be tested in case of the slab. The results of our 3D N-body method (Soft-spheres) are compared with the ones of the PIC code, which supposes an axial symmetry. The soft-spheres method is used to simulate the expansion of a target composed by a mixture with $\alpha = 0.5$ and $\mu = 0.5$, using $N_s = 2500$ soft-spheres. In the case of the PIC method, $N_p = 5e5$ particles are used. The initial aspect ratio of the slab is $H/R = 0.1$. Fig. 3.23 depicts the positions of slow and fast ions at different times, compared with the initial slab. An excellent agreement of the two techniques suggests that a 2D approximation, with the PIC code, may be done. On the contrary, as can be seen in the evolution of the expansion, the motion on the direction parallel to the slab surface cannot be neglected, even if the velocities v_z are larger respect to v_x, Fig. 3.24. Finally, Fig. 3.25 depicts the kinetic energy spectrum at $t = T_p$ of the fast species, showing a narrow peak of energy, as in the case of the mixture expansion of a spherical cluster. All calculations are performed normalizing the initial total charge, mass and radius of the slab.
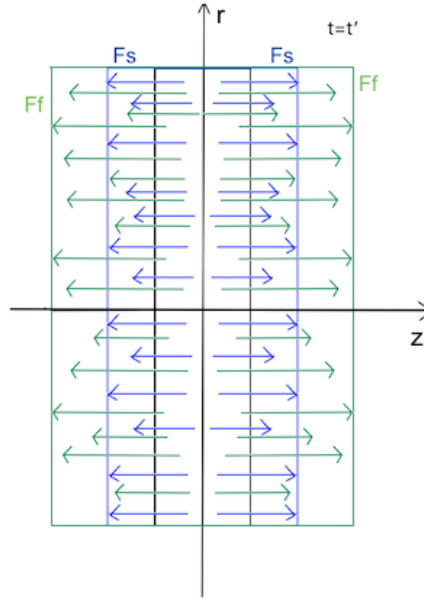
Figure 3.22: Expansion of an heterogeneous slab, made by two ions species, supposing only an expansion perpendicular to the surface of the slab.
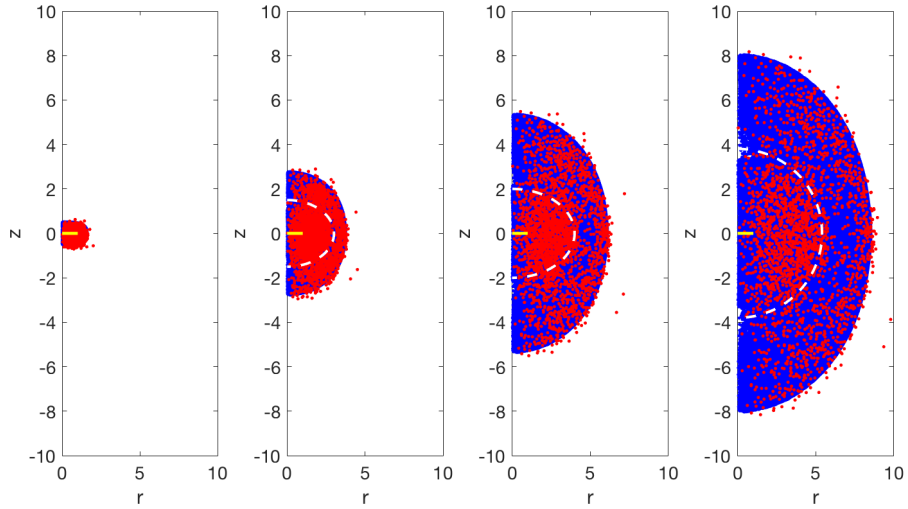

Figure 3.23: Evolution of the positions of fast and slow ions inside a slab made by a mixture of two type of ions ($\alpha = 0.5$ and $\mu = 0.5$), depicted with the Soft-Spheres method (red dots) in comparison with the PIC code (blue dots). Time of the pictures $1/4T_p, 1/2T_p, 3/4T_p, T_p$. Inside the dotted white lines, all the slow ions are confined.
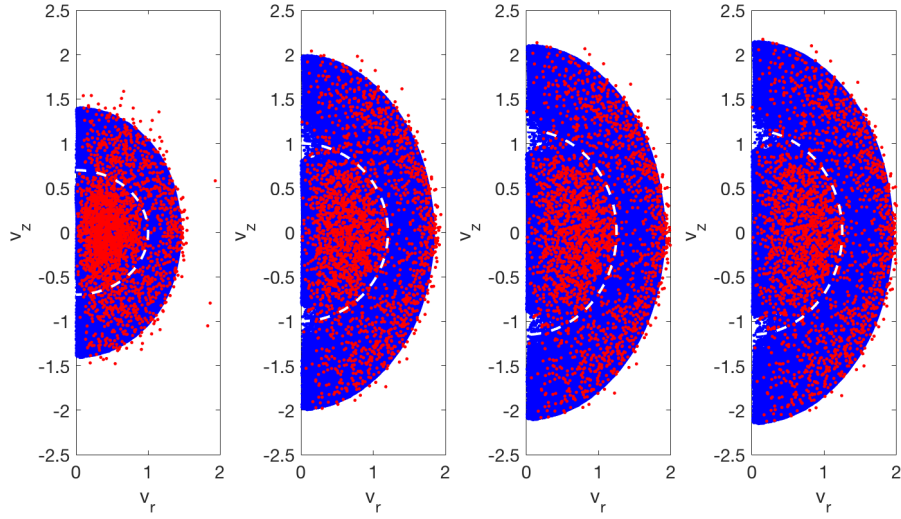
Figure 3.24: Velocities at different time steps $(1/4T_p, 1/2T_p, 3/4T_p, T_p)$ of fast and slow ions, depicted with the Soft-Spheres method (red dots) in comparison with the PIC code (blue dots). Same slab of Fig. 3.23. .
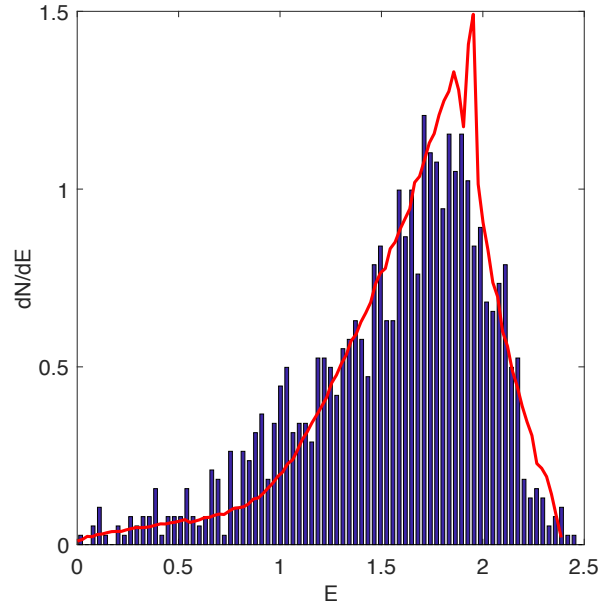
Figure 3.25: Kinetic energy spectrum of fast ions, same slab of Fig. 3.23. Blue histogram for the Soft-spheres method and red line for the PIC code.

Chapter 4

Results for spherical clusters

In the following chapter, some typical results are reported, regarding the expansion of spherical clusters. Firstly the phenomenon of shock formation is analyzed (Section 4.1), starting from a spherical nano-plasma, made by one ion species, with a non-uniform initial charge density (Peano et al., 2005). In this case, there is a maximum of the electric field inside the plasma region and overtakings between ions can occur. The shell method simulates this situation comparing results obtained with a high and low number of computational particles, to test the algorithm also in a case where the density could rise dramatically. Then, the Coulomb explosion of mixtures composed by two types of atoms is described (Boella et al., 2016), comparing results from the numerical method and the analytic solution, when available. Firstly, in Sec. 4.2 a Hydrogen-Deuterium mixture is considered, comparing the kinetic energy spectra obtained with the shell method and the soft-spheres, and by varying the parameter α also for values where the theoretical model is not applicable, for the presence of overtakings between fast ions. Secondly, a Deuterium-Tritium mixture is inspected (Section 4.3), with a value of the parameter $\alpha > \alpha_{crit}$ to have the possibility of comparison with the analytic solution. Then, a test on the kinetic energy spectrum is completed with the shell method, varying the parameter α also where the analytic solution is no more valid. The expansion of the same mixture is also performed with the soft-spheres method, in order to to test two different initial configurations of the ions to describe the initial uniform charge density of the sphere. The choice is between a random initial distribution and equally spaced coordinates of the particles on the section of the sphere. At the end in Sec. 4.4, the behavior of different Carbon-Hydrogen mixtures is simulated with the shell method, varying the positive charge of the carbon ion and, consequently, the parameter μ of the mixture. A detailed analysis is done on the changes of the asymptotic energy of the fast ions, varying the parameter α. The possibility of a linear dependence of the function $< \epsilon_\infty(\alpha) >$ is initially supposed and analyzed with numerical simulations. A simplified theoretic calculation is also proposed to verify or not this feature. Since not indicated differently, a suitable normalization for the physical quantities has been

used such that the total charge, the total mass of the plasma and the initial radius R are all equal to 1.

Declarations   Part of the work described in this Chapter was also previously published in the following publications, further reported in Appendix of this thesis: 1) E. Boella, B. Peiretti Paradisi, A. D'Angola, L. O. Silva and G. Coppa, Study on coulomb explosions of ion mixtures, Journal of Plasma Physics 82 (2016) 905820110, 2) B. Peiretti Paradisi, E. Boella, A. D'Angola and G. Coppa, Gridless simulation of collisionless systems with high degree of symmetry, Computer Physics Communications, 2017.

4.1 Shock formation phenomena described with the shell method

In this section, the possibility of arising of shock shells is analyzed, in case of a pure Coulomb explosion (Peano et al., 2006, 2007). When only one ion species is present, to obtain overtakings the initial ion density must be not uniform and the inner density of the cluster must be larger than the outer one. In this condition, a maximum of the electric field E appears inside the plasma region and E is no more a linear function of r, as in the case of uniform initial density. Consequently, the inner particles gain higher velocities and kinetic energies than the outer ones and overtakings can occur. Figs. 4.1 and 4.2 show the situation of an ion plasma made by only one ion species, with two regions of different initial densities. In particular, $n(r,0) = n_1$ when $r < R/3$ and n_2 when $r \in \left[\frac{R}{3}, R\right]$, with $n_1/n_2 = 8$. In Fig. 4.1 the value of the radial coordinate, $r(r_0, t)$, of the particles is plotted as a function of their initial radius r_0, at different times. In the inner region the dependence of r on r_0 remains linear because the density is constant.
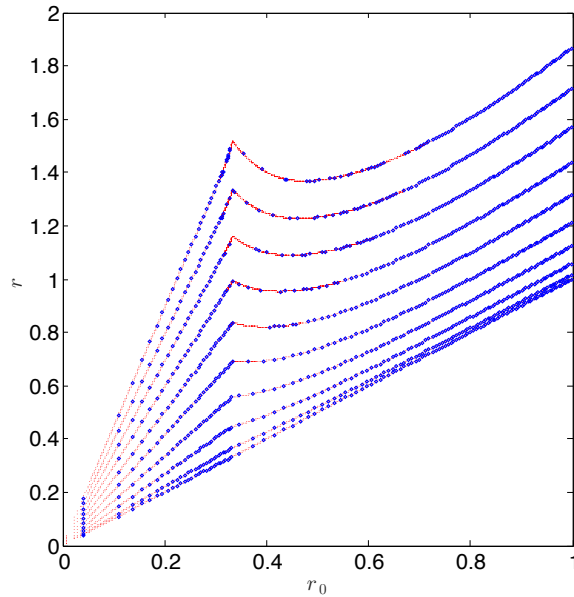
Figure 4.1: Radial coordinate, r, at different times ($t = 0 \div 1.47$) as a function of their initial position, r_0, for a single-species ion plasma with a non uniform initial density distribution. Results for 10^4 shells (blue dots) are compared with those obtained with 10^6 shells (red line). Adapted from B. Peiretti Paradisi, E. Boella, A. D'Angola and G. Coppa, Computer Physics Communications, 2017.

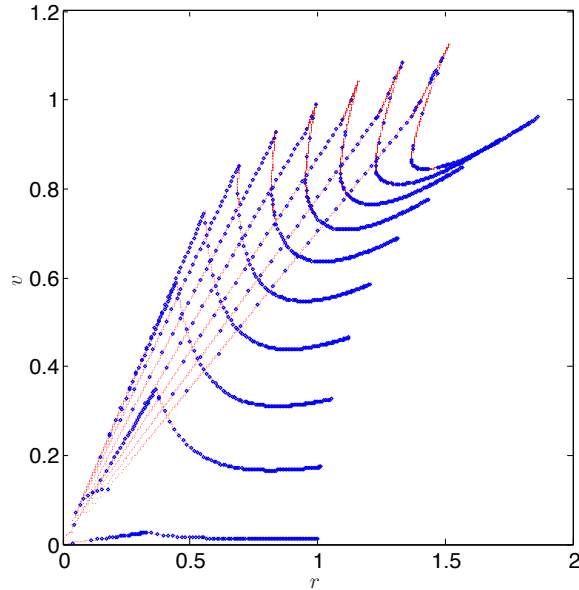Therefore, at the inner boundary of the outer region a portion of ions is less

Figure 4.2: Ion phase-space distribution at different times ($t = 0 \div 1.47$) for the same case of Fig. 4.1. Results for 10^4 shells (blue dots) are compared with those obtained with 10^6 shells (red line). Adapted from B. Peiretti Paradisi, E. Boella, A. D'Angola and G. Coppa, Computer Physics Communications, 2017.

accelerated than the inner ones, and halfway through the simulation, the function $r(r_0, t)$ highlights the phenomenon of overtakings, near the boundary of the two plasma regions. If two ions start their expansion at radii $r_{0,1} > r_{0,2}$ and then during the expansion they reach a radial position $r_2 > r_1$, we can see the presence of overtakings. Fig. 4.2 reports the evolution of phase-space distribution and similar considerations can be achieved. When two ions with radii r_1 and r_2, gain velocities $v_1 < v_2$ at a distance $r_1 > r_2$, overtakings can finally occur. In the simulation, the total charge and mass considered are normalized at 1, as well as the initial radius of the cluster. Despite the particular phenomenon analyzed, the results here reported show the capacity of the shell method to simulate cases in which the density, in theory, may become infinite in some points. A reference result obtained with a huge number of shells (10^6) is compared with a simulation with a low number of computational particles (10^4), and they are in perfect agreement.

62

4.2 Comparison between Soft-Spheres and shell method: expansion of a HD nanocluster

The first set of results, in the case of a mixture expansion, considers the Coulomb explosion of a spherical cluster, made by an ion mixture Hydrogen-Deuterium; Table 4.1 shows the values of the parameters for this type of mixture. Both the shell

q_f, q_s	$q_f = q_s = 1$
m_f, m_s	$m_s = 2m_f$
$\mu = \dfrac{q_s m_f}{q_f m_s}$	$\dfrac{1}{2}$
$\alpha_{crit} = \dfrac{q_s}{2q_f + q_s}$	$\dfrac{1}{3}$

Table 4.1: Simulation parameters.

and soft-spheres method were used to simulate the explosion, with the following computational parameters: $N_s = 5000$ Soft-Spheres with a finite radius of the particle $r_0 = 0.01$ and $N_c = 10^5$ shells. The final time of the simulation is $t_f = T_p$, being T_p the plasma period for the mixture. Ions are always supposed initially at rest and they start to be accelerated by electrostatic repulsion. In both the computational methods, particles are initially randomly distributed inside the cluster, always guaranteeing a uniform charge distribution of both ion species. At the end of the simulation, when the total kinetic energy of the plasma is considered quite constant, the normalized energy spectra for the fast ions is calculated numerically. Fig. 4.3 presents the results obtained by varying the parameter $\alpha = [0.2 \div 0.8]$, comparing the ones by the Soft-Spheres and the shell method. An analytic solution is not available for all the values of α, because we are crossing the limit of the presence of overtakings. Results from the shell method are in total agreement with the ones from the Soft-Spheres, while the spectrum of the 3D approach is noisy, due to the small number of computational particles used to simulate the expansion. We can see that the most energetic mixture is the one with the lower value of α, below the limit given by α_{crit}, where overtakings are present. For this value of α also the spread of energy is limited and the peak is very narrow.
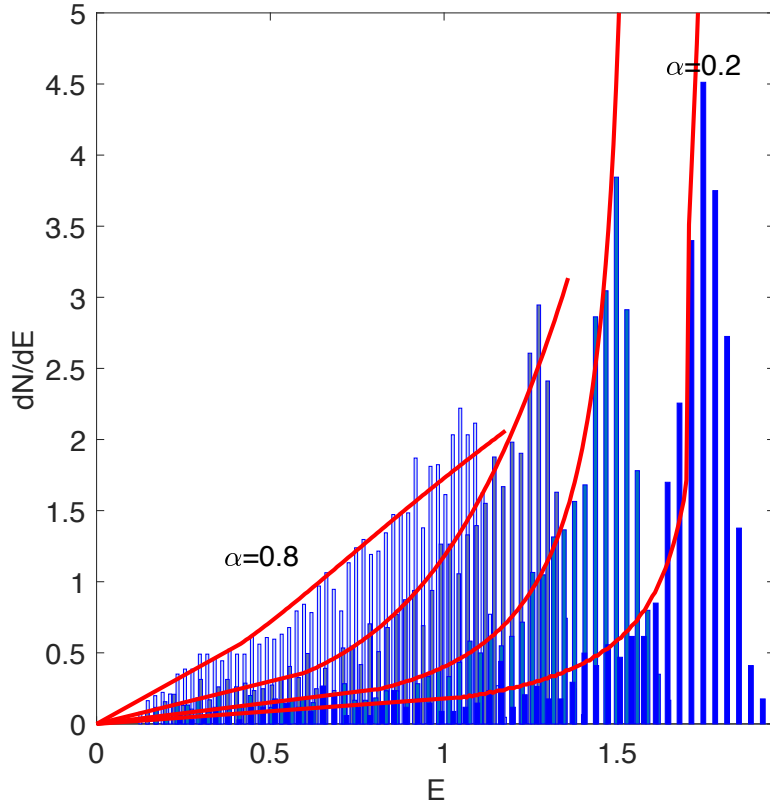
Figure 4.3: Kinetic energy spectrum of the fast ions for a mixture of HD, results for the shell method (red lines) compared with results from the Soft-Spheres (red lines).

4.3 Expansion of a DT mixture: the Soft-Spheres, the shell and the analytic solution

The second set of results (Figs. 4.4-4.6) displays the acceleration of an ion plasma made by a mixture of two different species, depicted with the shell method. The two species here considered present the mixture parameters in Tab.4.2, which could represent a mixture of Deuterium and Tritium. Choosing a proper value of the parameter $\alpha > \alpha_{crit}$ (for Fig. 4.4 and 4.5 $\alpha = 0.5$), analytic solutions for the problem are available (Boella et al., 2016) and can be used as a reference. The final time of the simulation is fixed at two plasma periods, $t_f = 2T_p$. Fig. 4.4 compares the phase-space distribution for the two species at different times, calculated with the shell method and analytic results. Only 10^3 shells are sufficient to depict the situation

q_f, q_s	$q_f = q_s = 1$
m_f, m_s	$m_s = 3/2 m_f$
$\mu = \dfrac{q_s m_f}{q_f m_s}$	$\dfrac{2}{3}$
$\alpha_{crit} = \dfrac{q_s}{2q_f + q_s}$	$\dfrac{1}{3}$

Table 4.2: Simulation parameters.

correctly. The slow species shows a linear behavior of the phase space during all the evolution, being the electric field linear with the radius inside the slow species sphere S_s (see Sec. 2.2.1). On the contrary, the fast species across all the plasma region is accelerated by a non-uniform electric field, with a peak at the boundary of S_s. Figure 4.5 presents $\mathcal{E}(t \to +\infty)/m$ of the light ions as a function of their initial radial coordinate, $r = r_0$. This function is important in order to calculate the asymptotic energy spectrum, $\frac{dN}{d\mathcal{E}}$, of the ions (considering that $\Delta\mathcal{E} = \frac{d\mathcal{E}}{dr_0}\Delta r_0$ and $\Delta N = 4\pi r_0^2 n_0 \Delta r_0$). The two figures show the excellent agreement between numerical and analytic results. Finally, the kinetic energy spectrum of the fast ions is calculated with the shell method, not only for $\alpha = 0.5$, but by varying its value in the range $[0.1 \div 0.9]$, also for values of α where analytic results are not reliable, due to the presence of overtakings. In this case, results are shown in elettronVolt, to highlight the range of energies reached by the explosion of this type of mixture. The initial radius of the cluster is $R = 6.5 nm$ and the final time of the simulation is a multiple of the plasma period $T_p = 2\pi/\omega_p$, where the plasma frequency of the mixture is defined as $\omega_p = \sqrt{(4\pi n q_f q_s)/m_f}$.

The third set of results (Figs. 4.7-4.10) presents the same mixture expansion ($\mu = 2/3$ and $\alpha = 0.5$), simulated for comparison with the Soft-Spheres method, with the two initial particle loading techniques described in Sec. 3.1. In this case, the simulation was stopped at $t_f = T_p$ to follow the initial transient. Both simulations are run with 25000 soft-spheres and the radius of each soft-sphere is fixed as $r_s = R_0/20$, respecting Eq. (3.8). In particular, Fig. 4.7, shows the phase space at different times and Fig. 4.8 the kinetic energy spectrum of the fast ions with soft-spheres equally spaced on the section at the initial time. On the other hand, Figs. 4.9 and 4.10 present the same situation with ions randomly distributed on the volume of the sphere. All the results are in perfect agreement with the analytic solution, (Boella et al., 2016). We can notice that in Fig. 4.9 the particles are spread a little more around the analytic solution, especially at the initial stage of the expansion, compared to the equally spaced particle loading, 4.7. A small number of computational particles depicts the expansion correctly, while the distribution of positions and velocities during the simulation is affected by a more regular initial distribution. In case of random initial positions an ensemble average on different
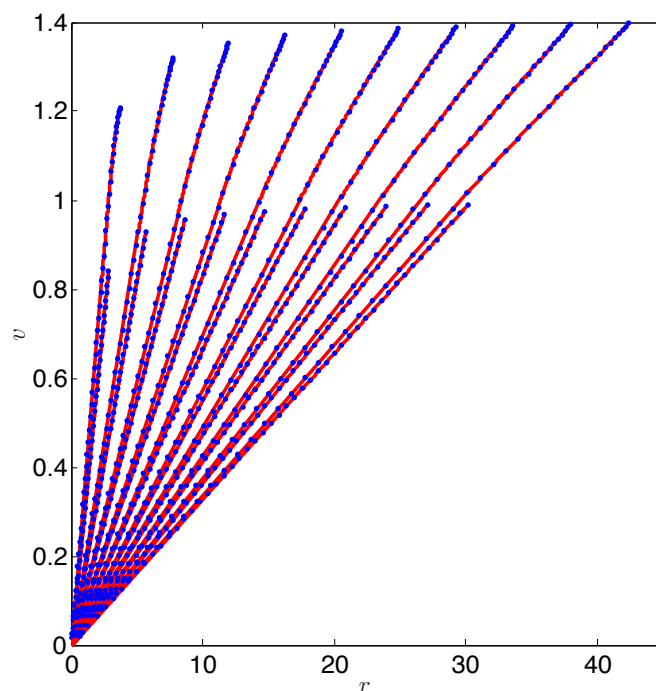
Figure 4.4: Phase-space distributions of a mixture with $m_1/m_2 = 2/3$ and $q_1 = q_2$ at different times ($t = 3 \div 31$). Results obtained with the shell method (blue dots) are compared with the analytic solution (red solid lines). Adapted from B. Peiretti Paradisi, E. Boella, A. D'Angola and G. Coppa, Computer Physics Communications, 2017.

sets of initial loadings could be impressive to perform. On the contrary, regarding the energy spectrum, the situation is different, and the 2nd particle loading method gives a more accurate outcome. In any case, the differences between the analytic solution and the numerical one are negligible.
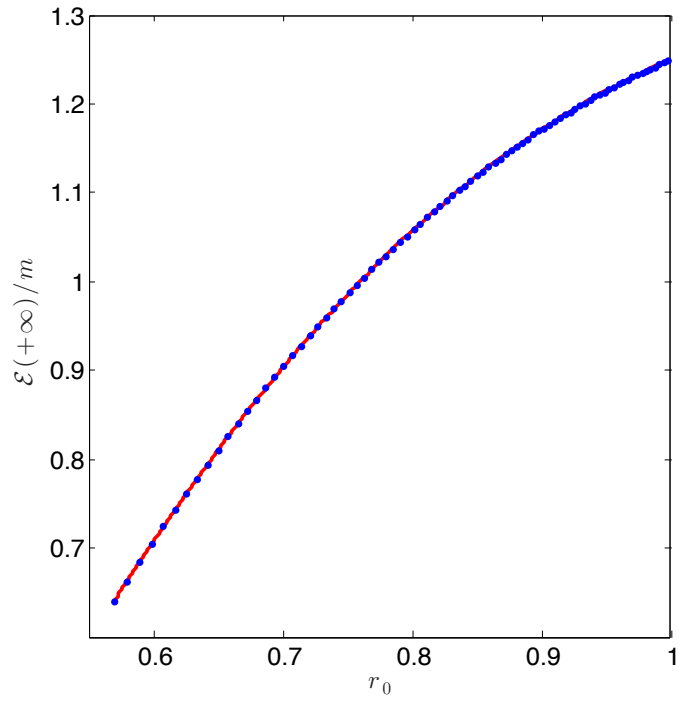
Figure 4.5: $\mathcal{E}(t \rightarrow +\infty)/m$ of the light ions as a function of their initial radial coordinate, r_0, for the case of Fig. 4.4. Results obtained with the shell method (blue dots) are compared with the analytic solution (red line). Adapted from B. Peiretti Paradisi, E. Boella, A. D'Angola and G. Coppa, Computer Physics Communications, 2017.
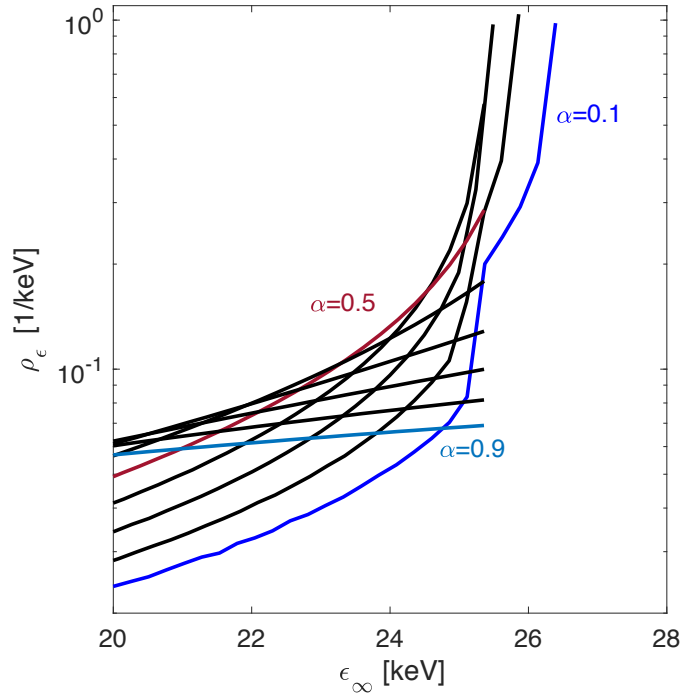
Figure 4.6: Enlargement of the normalized kinetic energy spectrum for the fast ions, in a spherical cluster composed by the same mixture of Fig. 4.4, varying the parameter α in the range $[0.1 \div 0.9]$, the mentioned case of $\alpha = 0.5$ is highlighted in red.
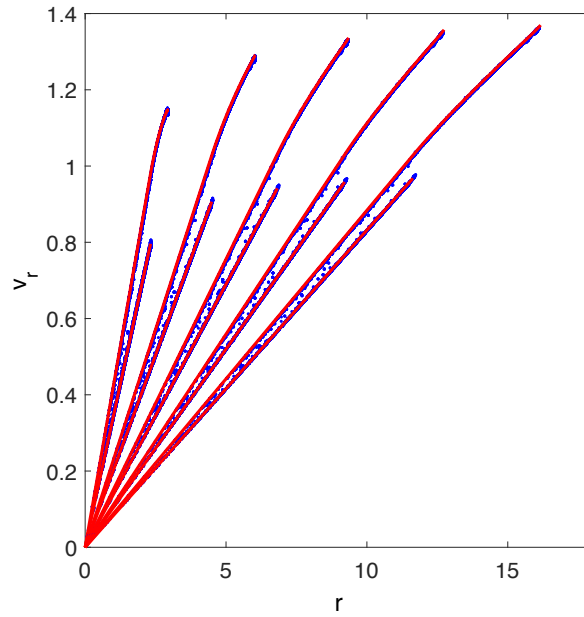
Figure 4.7: Phase space at different times, for a hetero-nuclear spherical cluster ($\mu = 2/3$ and $\alpha = 0.5$) depicted with the soft-spheres (blue points) in comparison with the theoretical model (red lines). The computational objects are loaded with equally spaced initial coordinates.
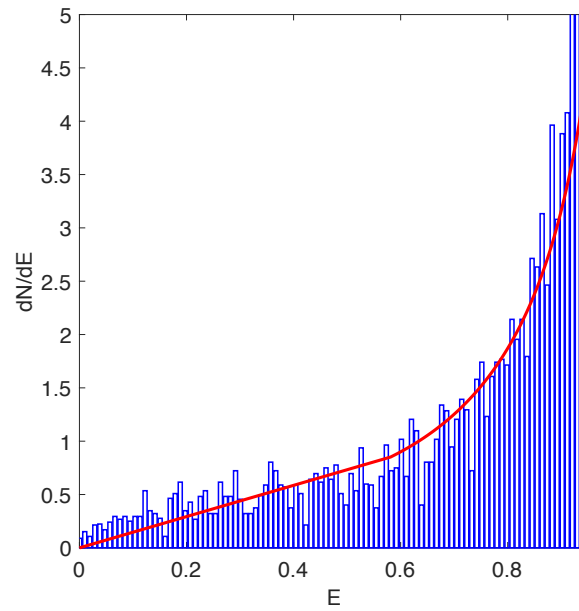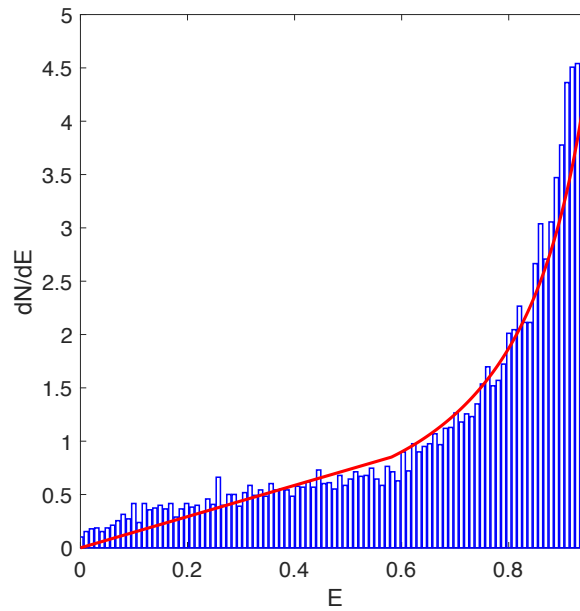

Figure 4.8: Energy spectrum in the same configuration of Fig. 4.7. Histogram in blue for the Soft-spheres method and red line for the analytic solution.
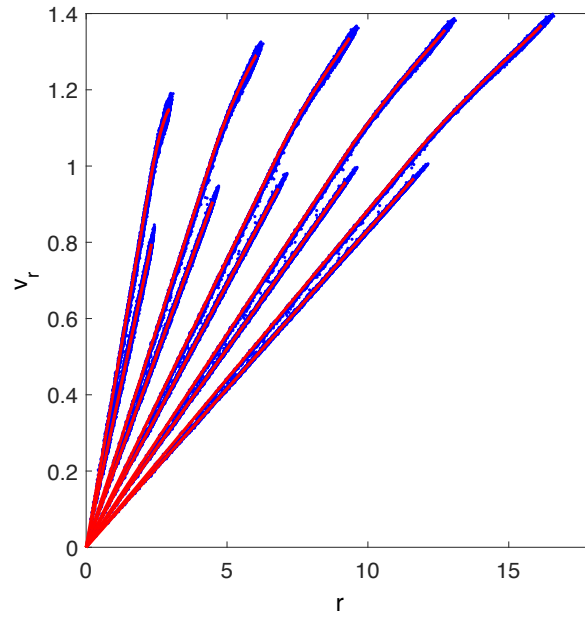
Figure 4.9: Phase space at different times for an expansion of an hetero-nuclear spherical cluster ($\mu = 2/3$ and $\alpha = 0.5$) with the soft-spheres (blue points) in comparison with the theoretical model (red lines). The computational objects are loaded with random initial positions.

Figure 4.10: Energy spectrum in the same configuration of Fig. 4.9. Histogram in blue for the Soft-spheres method and red line for the analytic solution.

4.4 Numerical and semi-analytical approaches for the energy spectra of CH composite cluster

In Chapter 2, the theoretical analysis of the expansion of composite clusters demonstrates the presence of a particularly attractive value for the mixture parameter α, for which fast ion spectra could be particularly narrow. A full set of calculations has been carried out to investigate that fact numerically for the mixtures C^+H^+, $C^{2+}H^+$, $C^{3+}H^+$ and $C^{4+}H^+$, using the shell method to simulate the Coulomb explosion (Tab. 4.3).

	C^+H^+	$C^{2+}H^+$	$C^{3+}H^+$	$C^{4+}H^+$
q_f, q_s	$q_s = q_f$	$q_s = 2q_f$	$q_s = 3q_f$	$q_s = 4q_f$
m_f, m_s	$m_s = 12m_f$	$m_s = 12m_f$	$m_s = 12m_f$	$m_s = 12m_f$
$\mu = \dfrac{q_s m_f}{q_f m_s}$	$\dfrac{1}{12}$	$\dfrac{1}{6}$	$\dfrac{1}{4}$	$\dfrac{1}{3}$
$\alpha_{crit} = \dfrac{q_s}{2q_f + q_s}$	$\dfrac{1}{3}$	$\dfrac{1}{2}$	$\dfrac{3}{5}$	$\dfrac{2}{3}$

Table 4.3: Simulation parameters.

Firstly, we depict in Fig. 4.11 the mean value of the energy for each type of mixture for $\alpha \in [0,1]$ and $\langle\epsilon_\infty\rangle$, as a function of α, seems to be linear. To examine this behavior, we start writing the total kinetic energy of the fast ions, $\mathscr{E}_f$, as the difference between the total potential energy at $t = 0$ and the total kinetic energy of the slow ions

$$\mathscr{E}_f = \mathcal{U}(t = 0) - \mathscr{E}_s = \frac{3(Q_s + Q_f)^2}{2R} - \frac{3}{5}N_s\frac{m_s}{2}[R\xi'_s(+\infty)]^2, \qquad (4.1)$$

being the mean kinetic energy simply $\langle\epsilon_\infty\rangle = \mathscr{E}_f/N_f$. The term to pay attention to, looking for linear dependence of the parameter α, is the only one that changes with the mixture composition: $[\xi'_s(+\infty)]^2$. As shown in Fig. 4.12, the trend of the kinetic energy of the slow species, $[\xi'_s(+\infty)]^2$, in function of the parameter α, seems to be linear. However, looking at the behavior of $[\xi'_f(+\infty)]^2$, in function of α (Fig. 4.13), it is clearly not linear. This particular trend of the square of ξ'_f and ξ'_s, has been examined. To achieve precise values of $\xi'_s(+\infty)$ and $\xi'_f(+\infty)$, instead of taking enormous values for T and instead of approximating $\xi'_s(+\infty) \cong \xi'_s(T)$, an extrapolation technique has been employed. In fact, the value of $\xi'_s(+\infty)$ progressively changes with the final time of the simulation and it tends to a constant value very slowly, Fig. 4.14. However, we can extrapolate the value of $[\xi'_s(+\infty)]^2$ with high precision, applying the conservation of energy on the slow species, and
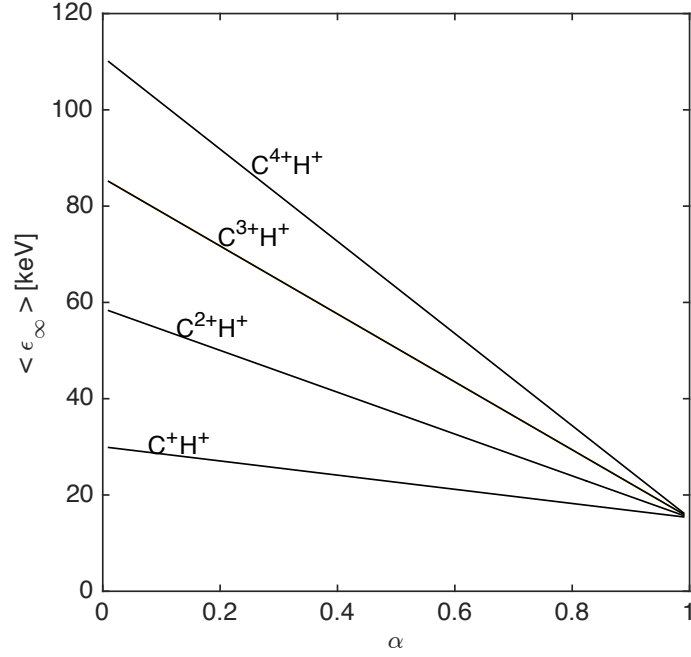
Figure 4.11: Mean value of the asymptotic energy for different mixtures Carbon-Hydrogen, as a function of the fraction of fast ions. Adapted from: E. Boella, B. Peiretti Paradisi, A. D'Angola, L. O. Silva and G. Coppa, Journal of Plasma Physics 82 (2016).

knowing the exact value of the kinetic and potential energy at a particular time step τ, as:

$$[\xi_s'(\tau)]^2 + 2U(\xi_s(\tau)) = [\xi_s'(+\infty)]^2 \tag{4.2}$$

being the potential energy zero when $t \to +\infty$. In particular, the numerical solution of the system (2.19), gives the value of $\xi_s'(t)$ at each time step, and to calculate the expression of the potential energy in function of $\xi_s'(t)$, we hypothesize a relationship between the two functions

$$\xi_f(t) \simeq p\xi_s(t) + q, \tag{4.3}$$

and for sufficiently high simulation time the approximation $\xi_f/\xi_s \sim p$ is valid. Eq. (4.3) is supported by results of numerical simulations, as can be seen in Fig. 4.15. The equation for $\xi_s(t)$ becomes

$$\frac{\mathrm{d}^2 \xi_s}{\mathrm{d} t^2} \simeq \frac{\mu}{\xi_s^2} \left(\frac{\alpha}{p^3} + \bar{\alpha} \right), \tag{4.4}$$

72
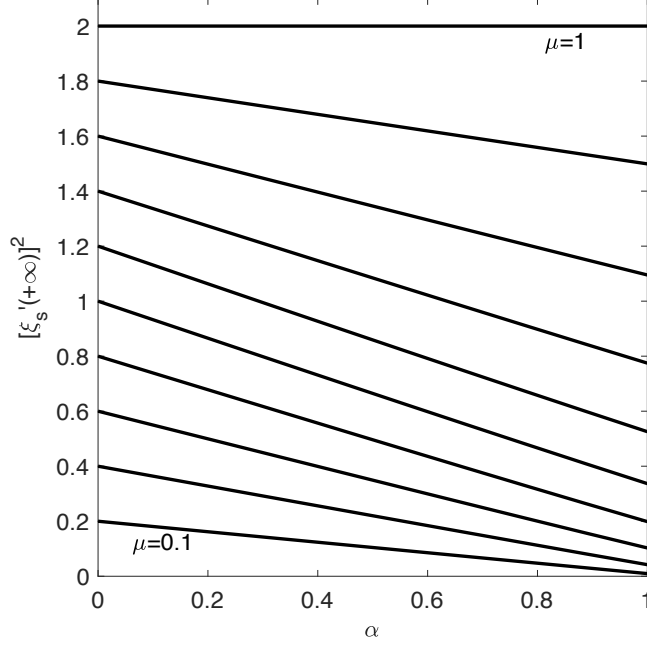
Figure 4.12: $[\xi_s'(+\infty)]^2$ at different μ, in function of α.

being $\xi_s'' = -\partial U/\partial S$, the expression of U, integrated between $t = 0$ and $t = \tau$, is

$$U = \frac{\mu}{\xi_s}\left(\frac{\alpha}{p^3} + \bar{\alpha}\right). \tag{4.5}$$

In the end, the value of $[\xi_s'(+\infty)]^2$ is calculated as

$$[\xi_s'(+\infty)]^2 = [\xi_s'(\tau)]^2 + \frac{2\mu}{\xi_s(\tau)}\left(\frac{\alpha}{p^3} + \bar{\alpha}\right), \tag{4.6}$$

and it can be demonstrated that the trend of the asymptotic kinetic energy is not really linear in function of α. Fig. 4.16 depicts the standard deviation of the spectrum, σ_ϵ, calculated for the four types of mixture. There is a minimum value of α, which is close to α_{crit} when $(m_s/q_s)/(m_f/q_f) \gg 1$. In fact, for $\alpha \simeq \alpha_{crit}$ the spectrum has a large plateau and a sharp peak. Probably the plateau gives a non-negligible contribution to σ_ϵ, while for practical applications the presence of the peak and its energy spread are more critical.

For the same mixtures considered in the calculation of the mean energy (Tab 4.3 gives characteristic parameters), in Figs. (4.17-4.20) the shapes of the energy spectra for different values of α are presented, highlighting the ones with the α closest to α_{crit}. Approaching the value of α_{crit}, the spectrum becomes narrower and narrower,
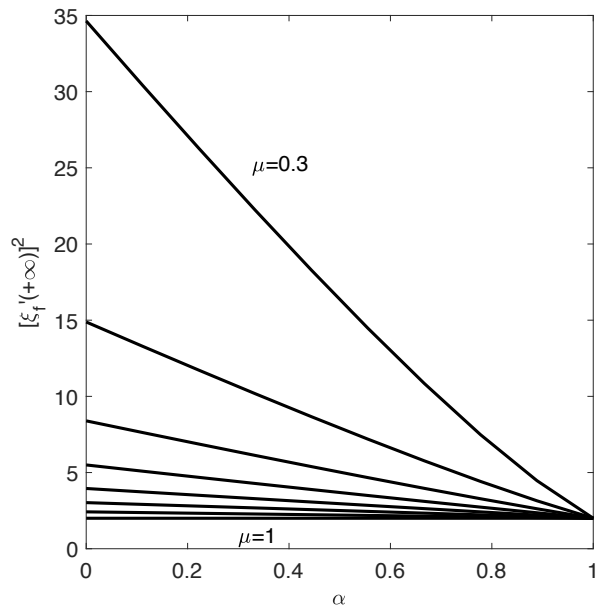
73

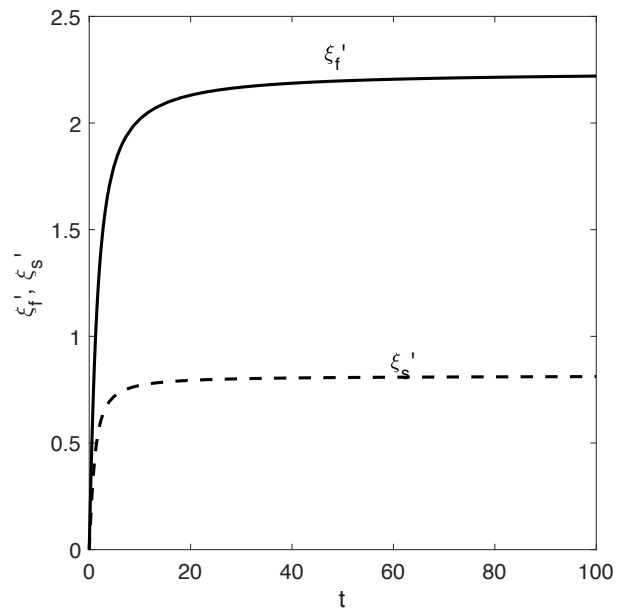Figure 4.13: Behavior of $[\xi'_f(+\infty)]^2$ at different μ.

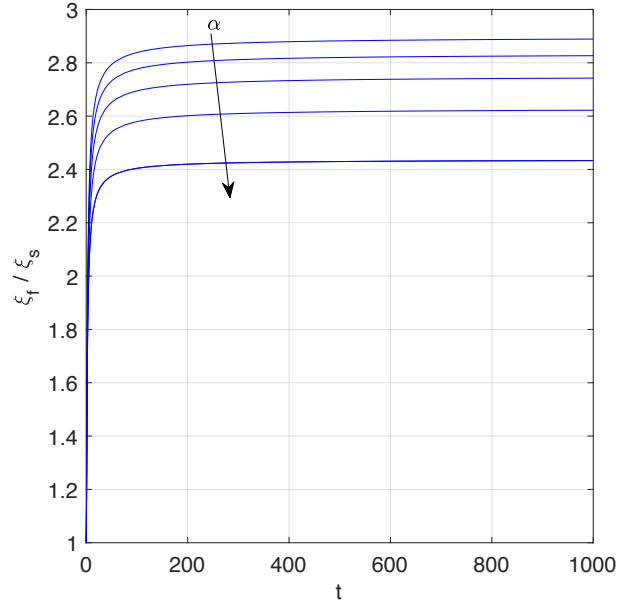Figure 4.14: Behavior of the functions $\xi'_s(t)$ and $\xi'_f(t)$.

Figure 4.15: Evolution of the ratio ξ_f/ξ_s for sufficiently high simulation times; varying the parameter α, it tends to a constant value.

confirming the minimum on the standard deviation of the energy (Fig. 4.16). In this case, results are shown in dimensioned units: the initial radius of the cluster is $R = 6.5$ nm and the final time of the simulation is a multiple of the plasma period $T_p = 2\pi/\omega_p$ (in the range $90 \div 400$ fs), where the plasma frequency of the mixture is defined as $\omega_p = \sqrt{(4\pi n q_f q_s)/m_f}$. As can be seen, the peak energies reached by the fast species are in the range $25 \div 50$ keV.
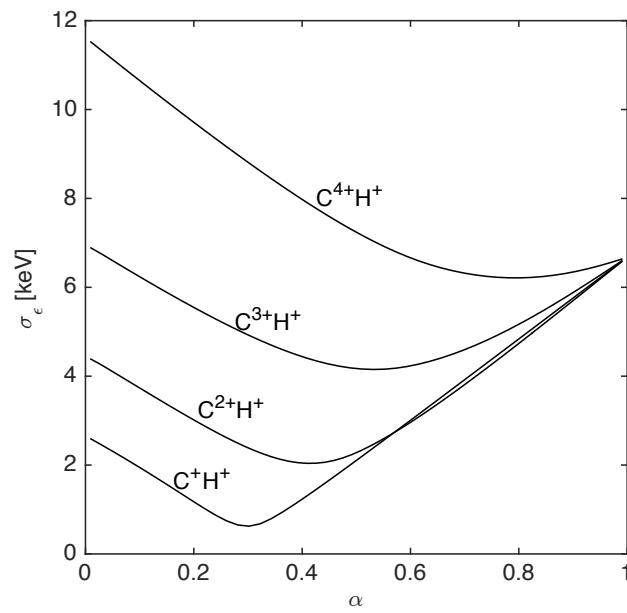
Figure 4.16: Standard deviation of the energy spectra as a function of the fraction of fast ions, for different mixtures Carbon-Hydrogen. Adapted from: E. Boella, B. Peiretti Paradisi, A. D'Angola, L. O. Silva and G. Coppa, Journal of Plasma Physics 82 (2016).
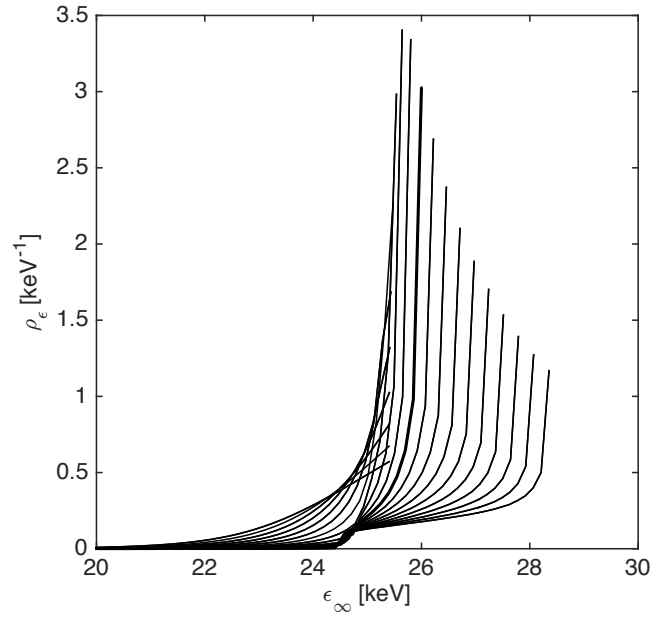
Figure 4.17: Energy spectra of a mixture C^+H^+ with different values of α in the range $[0.2, 0.4]$. Adapted from: E. Boella, B. Peiretti Paradisi, A. D'Angola, L. O. Silva and G. Coppa, Journal of Plasma Physics 82 (2016).
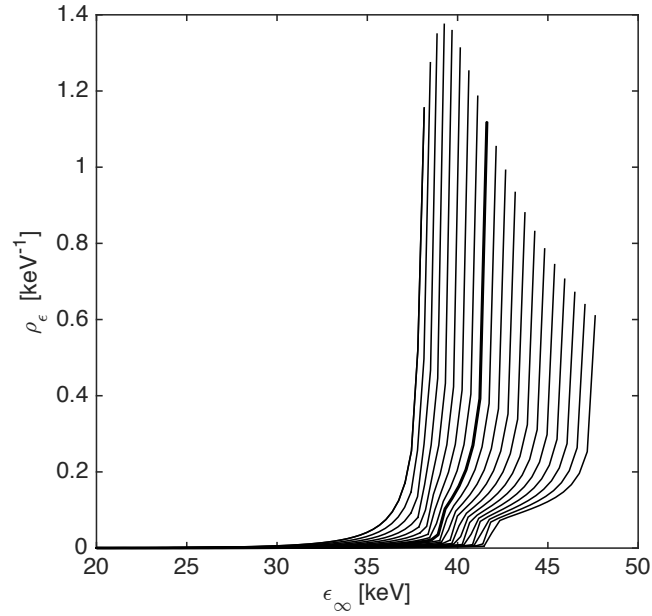

Figure 4.18: Energy spectra of a mixture $C^{2+}H^+$ with different values of α in the range $[0.3, 0.5]$. Adapted from: E. Boella, B. Peiretti Paradisi, A. D'Angola, L. O. Silva and G. Coppa, Journal of Plasma Physics 82 (2016).
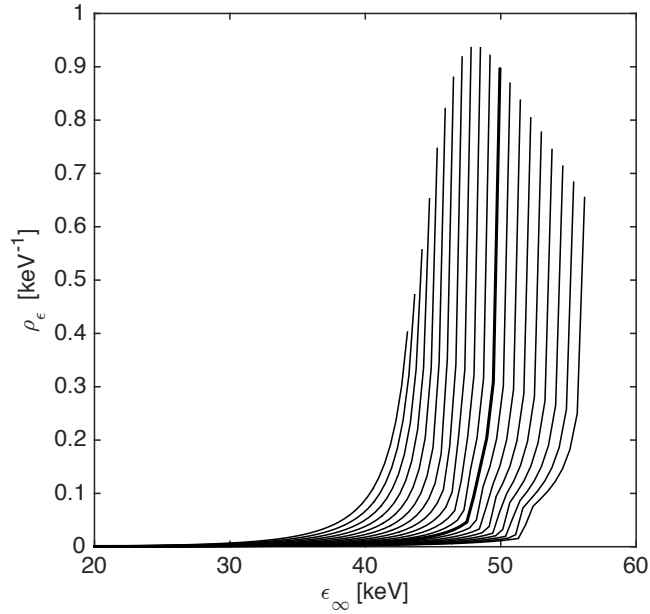
Figure 4.19: Energy spectra of a mixture $C^{3+}H^+$ with different values of α in the range $[0.45, 0.65]$. Adapted from: E. Boella, B. Peiretti Paradisi, A. D'Angola, L. O. Silva and G. Coppa, Journal of Plasma Physics 82 (2016).
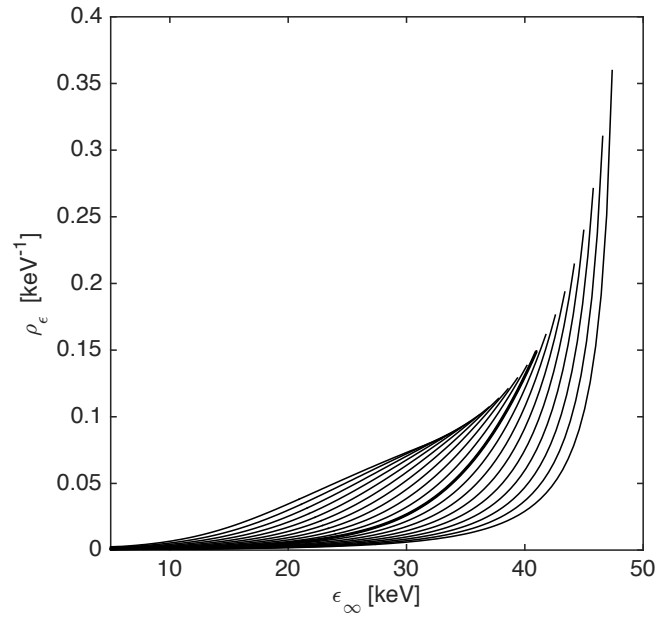

Figure 4.20: Energy spectra of a mixture $C^{4+}H^+$ with different values of α in the range $[0.7, 0.9]$. Adapted from: E. Boella, B. Peiretti Paradisi, A. D'Angola, L. O. Silva and G. Coppa, Journal of Plasma Physics 82 (2016).

Chapter 5

Results for cylindrical targets

In the present chapter, the dynamics of ions acceleration by a Coulomb explosion of a thin slab is investigated, employing the EXPYCIL PIC code, the soft-spheres and the ring method. In the first set of results, a cylindrical plasma made by one ion species is considered, following the expansion of some sample particles and varying the initial aspect ratio of the target, Sec. 5.1. The angular distribution of the energy is also calculated, to inspect the presence of a common direction of expansion. All the comparisons between the ring method and the PIC code return an excellent agreement and both methods are able to depict the considered phenomena correctly. Section 5.2 presents an interesting estimation on the expansion dynamics of a slab, in comparison with the one of a sphere with the same initial potential energy. In the second part of the chapter, both homogeneous mixture and double-layer targets are examined. In particular, multi-layer targets have been used to increase the conversion efficiency of the laser energy into plasma (Fourkal et al., 2005). In fact, the use of targets made by two different ion species, changing initial aspect ratios and compositions, opens up new opportunities for controlling and optimizing the parameters of the fast proton beam, such as its energy spectrum and the size of the region where the beam deposits its energy. On this purpose, the fast kinetic energy spectra in case of an heterogeneous slab are calculated, using the PIC code and the Soft-Spheres method, varying all the possible parameters of the mixture: the fraction of fast ions α, the initial aspect ratio H/R and the mixture parameter μ, showing compelling trends on the narrowing of the spectrum, Sec. 5.3. Therefore, the heterogeneous slab geometry is compared with the double-layer target in terms of velocities and positions distribution and kinetic spectrum of the fast species, through the PIC code, Sec. 5.4. Finally, the possibility of a different initial charge density inside the target is considered, compared with the standard case of uniform charge density of the two species, Sec. 5.5. The laser pulse has a Gaussian spatial profile, due to this fact also the distribution of the ionization inside the target can be spatially Gaussian, both for the fast and the slow species, (Bulanov et al., 2008).

Declarations   Part of the work described in this Chapter was also previously published in the following publication, further reported in Appendix of this thesis: B. Peiretti Paradisi, E. Boella, A. D'Angola and G. Coppa, Gridless simulation of collisionless systems with high degree of symmetry, Computer Physics Communications, 2017.

5.1 Expansion of a homogeneous cylindrical slab

The Coulomb explosion of a homogeneous cylinder is firstly considered, here simulated with two techniques: the ring method and the PIC code. Firstly the evolution of the electric field inside the plasma region is presented, starting from the time $t = 0$, in Fig. 5.1 and after five plasma period, Fig. 5.2. The area considered in the two figures is the computational domain, where ions are present. At $t = 0$ it coincides with the initial area of the slab and at the end of the simulation the initial area of the slab is highlighted in red in the picture.
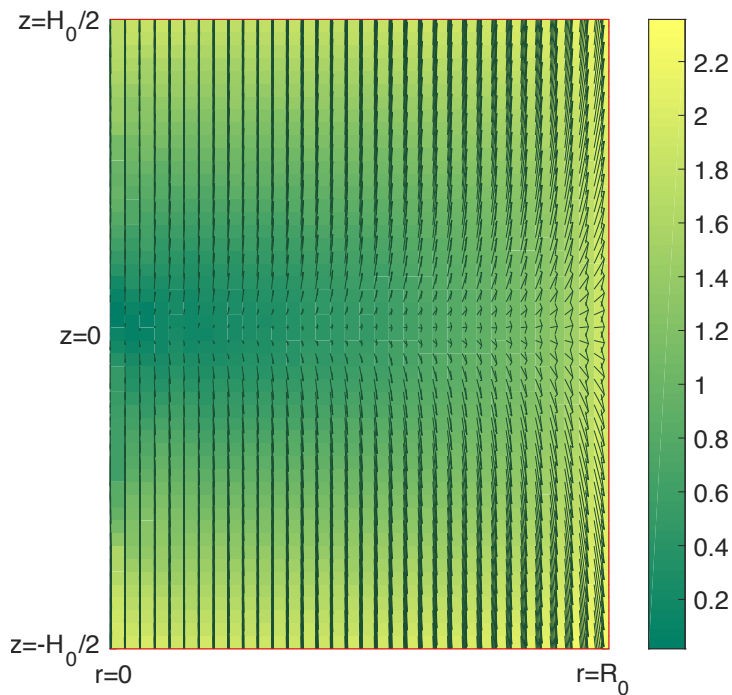

Figure 5.1: Electric field obtained with the PIC method by solving the Poisson's equation with boundary conditions (Eq. 3.26) at $t = 0$, inside a slab with uniform charge distribution and aspect ratio $H/R = 1$.

Figs. 5.3-5.6 present the expansion dynamic; two sets of results are provided, in which the cylinder has different aspect ratios. This is a case of practical interest, as it simulates the ion acceleration of the positive ions of a thin solid target after interaction with an ultraintense laser pulse. Figures 5.3 and 5.4 show the trajectories of the ions and the angular distribution of the kinetic energies for a cylinder with initial aspect ratio $H/R = 0.1$. Figures 5.5 and 5.6 present the same physical quantities for a cylinder with $H/R = 1$. In the Figures, the results of the
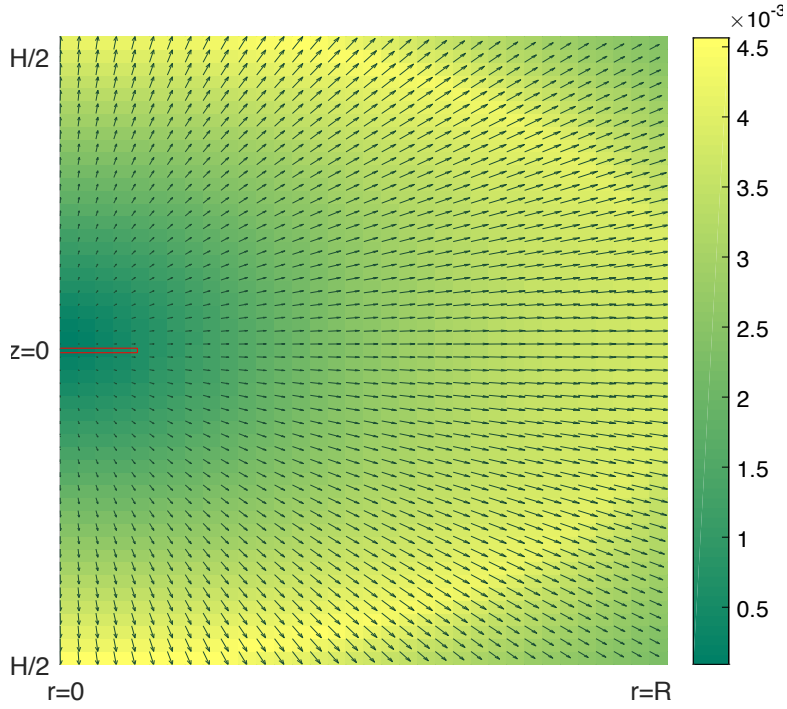
81

Figure 5.2: Electric field after five plasma period, the boundary of the initial slab is depicted in red.

ring method are compared with those obtained by using the EXPICYL PIC code. The agreement between the two techniques is excellent. Looking at the trajectories evolution for sample particles we can notice that when the slab has a more compact aspect ratio ($H/R = 1$, Fig. 5.5) also the particles near the cylinder center have a non negligible acceleration on the radial direction, while in case of a thinner slab ($H/R = 0.1$, Fig. 5.3) the acceleration for the central particles is predominant on the axial direction. Some tests reducing the thickness of the slab could be done to investigate this behavior, which is fundamental for practical application, where a predominant direction of propagation is needed. The same considerations could be done looking at the energy angular distributions.
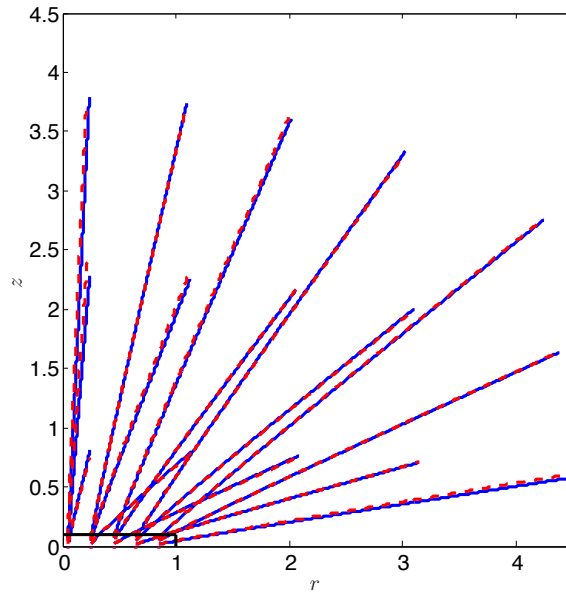
Figure 5.3: Particle trajectories for the Coulomb explosion of an ion plasma having initially a cylindrical shape ($H/R = 0.1$) for $t = 0 \div 4$. Results obtained with the ring method (blue lines) are compared with those obtained with the PIC method (red dotted lines). Adapted from B. Peiretti Paradisi, E. Boella, A. D'Angola and G. Coppa, Computer Physics Communications, 2017.
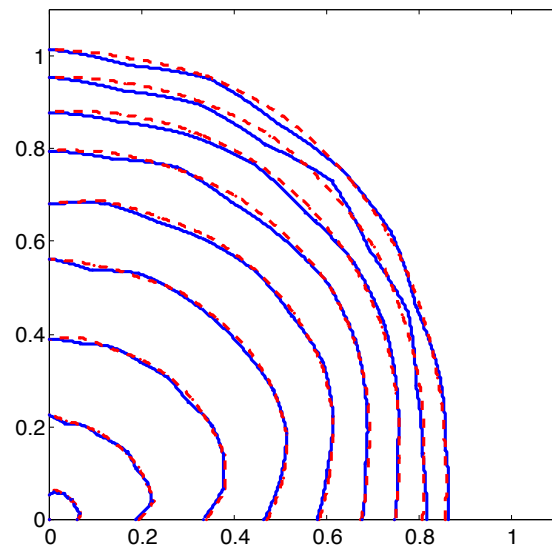

Figure 5.4: Angular distribution of $\mathcal{E}/m$ for the case of Fig. 5.3 for $t = 0 \div 4$. Results obtained with the ring method (blue lines) are compared with those obtained with the PIC method (red dotted lines). Adapted from B. Peiretti Paradisi, E. Boella, A. D'Angola and G. Coppa, Computer Physics Communications, 2017.
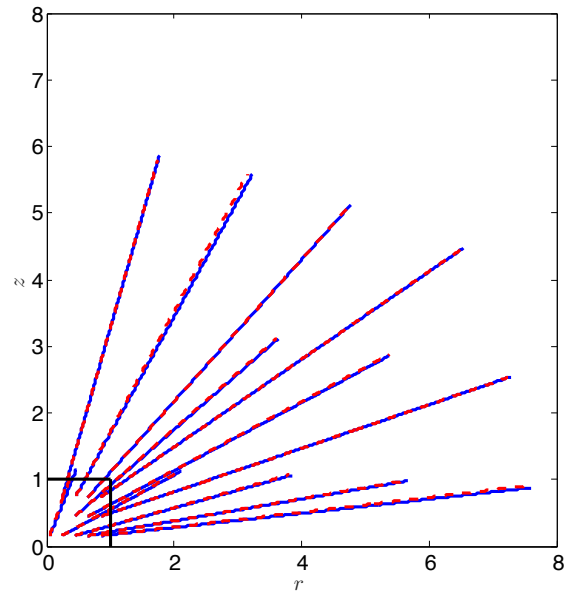
Figure 5.5: Same as Fig. 5.3, but for a cylinder with $H/R = 1$ for $t = 0 \div 10$. Results obtained with the ring method (blue lines) are compared with those obtained with the PIC method (red dotted lines). Adapted from B. Peiretti Paradisi, E. Boella, A. D'Angola and G. Coppa, Computer Physics Communications, 2017.
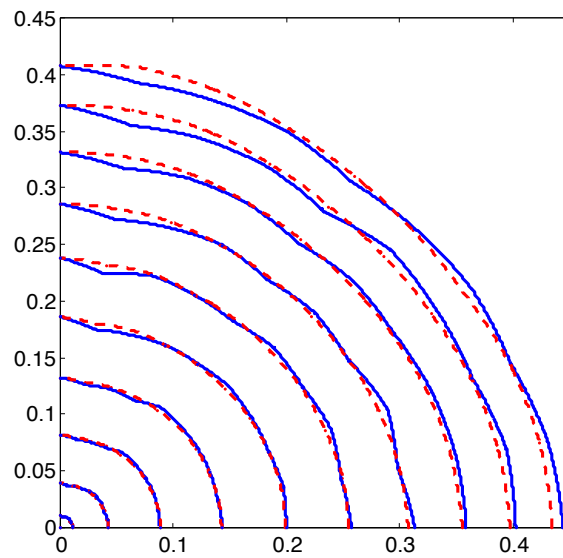

Figure 5.6: Same as Fig. 5.4, but for a cylinder with $H/R = 1$ for $t = 0 \div 10$. Adapted from B. Peiretti Paradisi, E. Boella, A. D'Angola and G. Coppa, Computer Physics Communications, 2017.

5.2   Expansion of a cylinder compared with a sphere with same initial potential energy

In the following section, an interesting comparison is made, between the expansion of a cylinder with initial aspect ratio $H/R = 0.1$, made by one ion species, and of a sphere with the same total potential energy. The simulations are made using the PIC code, to study the different evolutions of the expansion. Simulations are performed by using $N_p = 2 \cdot 10^6$ computational particles, to guarantee a very high order of precision.
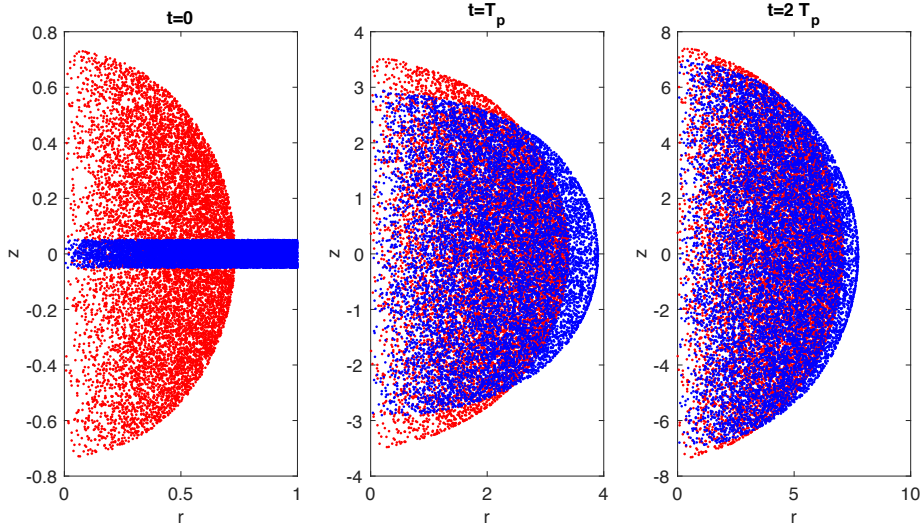

Figure 5.7: Distribution of ions in the (r, z) plane for a cylindrical target made by a single ion species (blue dots), compared with the evolution of the expansion of a sphere with the same initial potential energy (red dots). Results obtained with the PIC method at different t $(0, T_p, 2T_p)$.

Figure 5.7 depicts the positions distribution at different times, showing that also starting with different geometries, if the radial dimension of the slab is comparable with the radius of the sphere, after some plasma periods the two expansions progress similarly. This is since, for the thin slab, initially the acceleration on the axial direction is very high and in a short time a spherical shape is reached during the expansion. Fig. 5.8 shows the energy spectra, which are comparable regarding peak energy and energy spread, because the initial potential energy was the same, also with two different initial geometries.
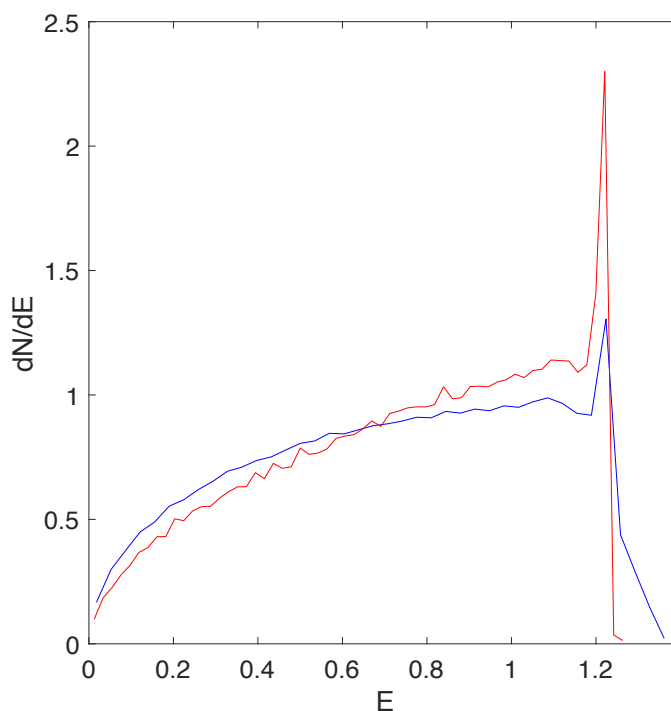
Figure 5.8: Energy spectra of the same case of Fig. 5.7, blue line for the cylindrical slab and red line for the sphere.

5.3 Expansion of a heterogeneous slab, made by two ion species

The following set of results considers a slab made by a mixture of two types of ions. In this case, to have an idea of the energy reached by the fast species in this configuration the PIC code simulates a realistic situation of a slab with initial total density $n = 10^{22}\mathrm{cm}^{-3}$ and initial height and radius $H = 0.5\mu$m, $R = 5\mu$m, the species considered are Hydrogen and Deuterium. The parameter α of the mixture is varied, to investigate the influence on the behavior of the kinetic energy spectrum. We can see in Fig. 5.9 how in this configuration the fast species gain interesting peak energy, on the order of hundred of MeVs, with a very narrow peak for $\alpha = 0.3$. A dimensionless version of the code analyzes the same mixture with two initial aspect ratio of the slab. Table 5.1 shows the choice of the characteristic mixture parameters. The kinetic energy spectra for the fast ions have been calculated, both with the PIC method and the soft-spheres, to have a comparison. Fig. 5.10 shows the results for a slab with initial aspect ratio $H/R = 0.1$, while in Fig. 5.10 is shown the case with
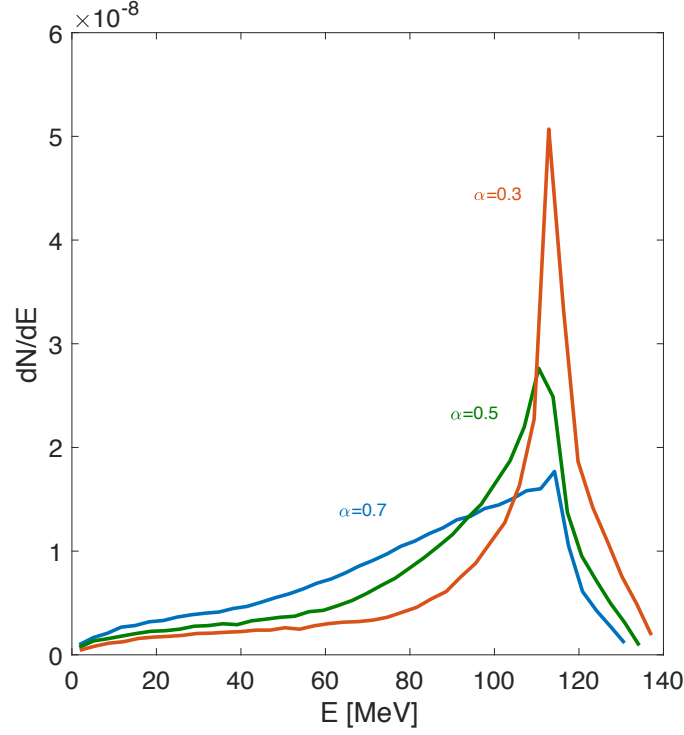
86

Figure 5.9: Energy spectra of the Hydrogen ions in a real slab, with initial density $n = 10^{22}\text{cm}^{-3}$ and initial aspect ratio $H/R = 0.1$, varying the α parameter.

	Case 1	Case 2
α	$[0.3 \div 0.7]$	$[0.3 \div 0.7]$
$\mu = \dfrac{q_s m_f}{q_f m_s}$	$\dfrac{1}{2}$	$\dfrac{1}{2}$
H/R	0.1	0.01

Table 5.1: Simulation parameters

$H/R = 0.01$. All the energy spectra are here normalized, considering a slab with unitary charge and mass. The comparison between the two techniques displays the ability to depict the phenomenon correctly with both the computational methods. The Soft-Spheres method is more noisy respect to the PIC method, due to the small number of particles used to simulate the expansion. To mitigate the noise effect in some simulation an ensemble average on different initial distributions was done.
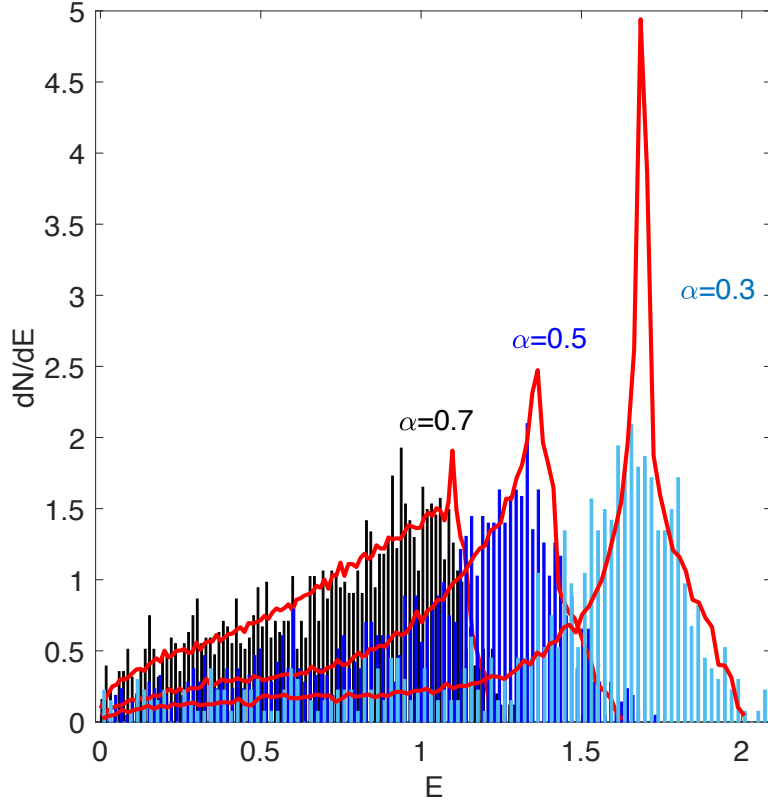
Figure 5.10: Kinetic energy spectra for the fast ions, cylindrical hetero-nuclear target ($\mu = 1/2$), varying the parameter α. Initial aspect ratio $H/R = 0.1$. Red line results from the PIC method, compared with the Soft-Spheres ones (dotted lined).

Finally, we have considered a situation with the same initial slab, in dimensionless units, varying only the parameter μ of the mixture, considering also heavier slow ions. The three values considered are $\mu = 1/12$ which can depict a situation Hydrogen-Carbon, $\mu = 1/200$ as a mixture Hydrogen-Platinum and a central value, $\mu = 1/100$. In Fig. 5.12 the Hydrogen energy spectra are presented, for the three chosen value of μ. The evident trend is increasing value of the peak energy and a larger plateau with heavier slow ions.
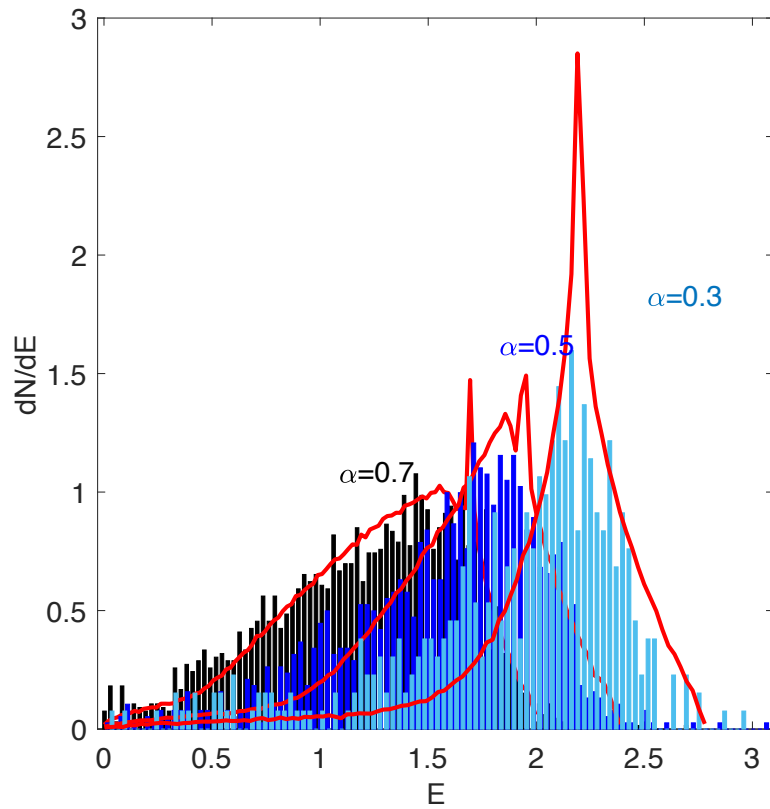
Figure 5.11: Same as Fig. 5.10 with initial aspect ratio $H/R = 0.01$. Red line results from the PIC method, compared with the Soft-Spheres ones (dotted lined).
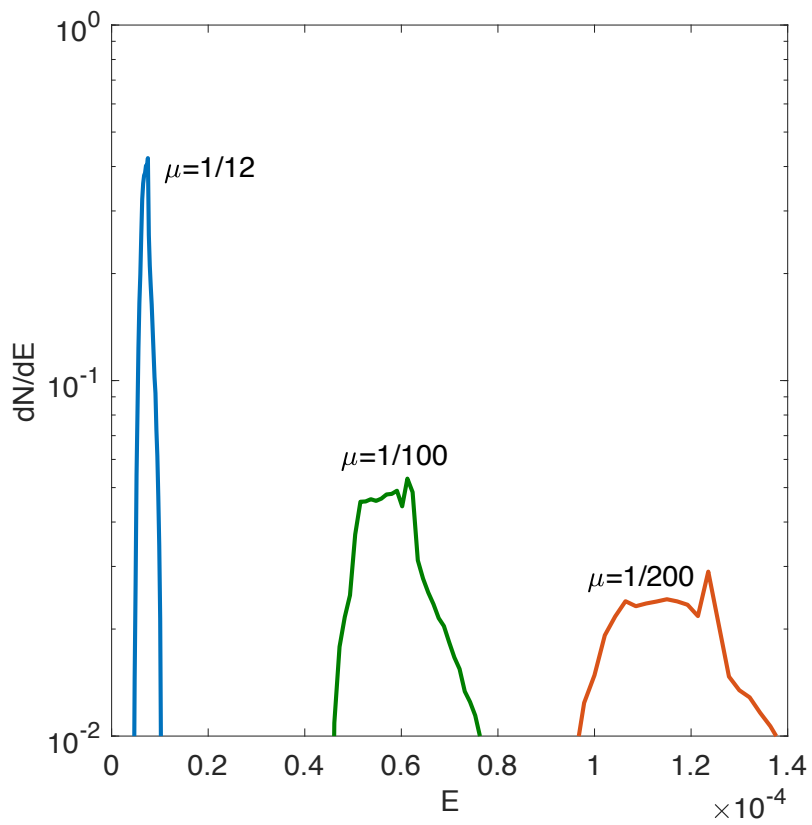
Figure 5.12: Energy spectra of the fast species for a heterogeneous slab, varying the parameter μ of the mixture. The results are presented in dimensionless units.

5.4 Comparison of a heterogeneous slab and a double-layer target

As seen in the previous sections, to achieve energies in the order of MeV and peaked energy spectra, a cylindrical configuration with a single ion species is not suitable. Therefore, two configurations with more than one ion species have been tested: a cylindrical plasma made by a mixture of two species and a double layer target. The second geometry is commonly the more used since it is the easiest to design and be produced practically. The following parameters have been chosen for this set of results, Tab.5.2, varying the initial aspect ratio of the slab; the total

	Single slab with mixture	Double-layer target
α	0.5	0.5
$\mu = \dfrac{q_s m_f}{q_f m_s}$	0.01	0.01
H/R	[0.5, 0.1, 0.01]	[0.25, 0.05, 0.005] each slab

Table 5.2: Simulation parameters.

aspect ratio in case of the double layer targets, obtained summing the aspect ratio of the layer made by the fast species and the ones of the slow species, corresponds to the aspect ratio in case of the single slab made by a mixture. Considering the same value of α, the density of both species is the same in the two geometries. The PIC method was used to obtain all the results in this section. Figures 5.13-5.18 compare the phase space distribution of the two initial geometries. In particular, in Figs. 5.13, 5.15 and 5.17, the evolution of the phase space distribution is obtained in the radial direction, for the three values of initial aspect ratio, and we can see a similar global trend in the radial position evolution and values of the velocities. On the contrary, it is interesting to highlight from Figs. 5.14, 5.16 and 5.18 how the fast species propagates only on one side of the slab in the case of the double layer targets, due to the presence of the compact slow species layer on the other side. All the values of speeds are comparable for the two initial configurations, while there are some changes varying the initial aspect ratio. A discrete increase on the maximum reached by the velocities in radial and axial direction is noticeable passing from the case of $H/R = 0.5$ to $H/R = 0.1$, while there isn't a significant difference between the two cases $H/R = 0.1$ and $H/R = 0.01$, in terms of maximum speeds. Figs. 5.19-5.22 show the kinetic energy spectra obtained for the fast species, varying the initial aspect ratio. In particular, the energy spectra is calculated in both the directions of

propagation of the ions, axial and radial. As we can see as a common trend the peak of energy at high values is given mainly by the kinetic energy in the radial direction. Figure 5.23 show the total kinetic spectra, comparing results for both the geometries. The trend is increasing value of the peak energy decreasing the thickness of the slab and a more narrow peak in case of heterogeneous slab, respect to a double-layer. Otherwise, we have to consider that the use of a heterogeneous thin slab could be difficult and the double layer target is more accessible to be produced and managed.
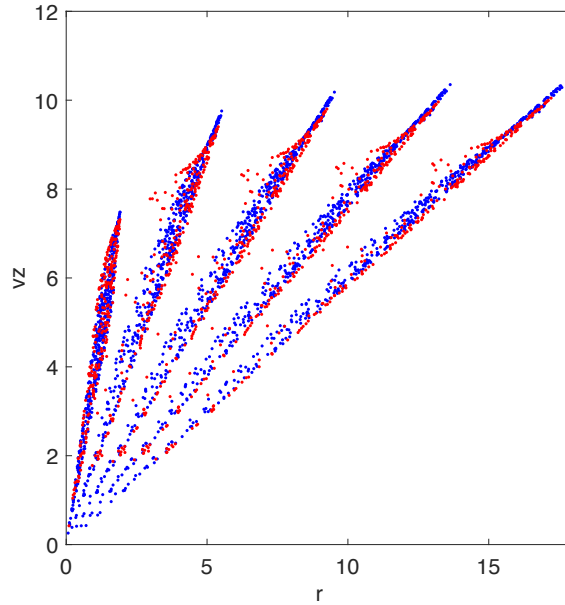
Figure 5.13: Phase space evolution on radial direction for an hetero-nuclear made by an ion mixture ($\mu = 0.01$, $\alpha = 0.5$) cylindrical target with initial aspect ratio $H/R = 1/2$ (red dots), in comparison with a double layer target (blue dots). Results obtained with the PIC code.
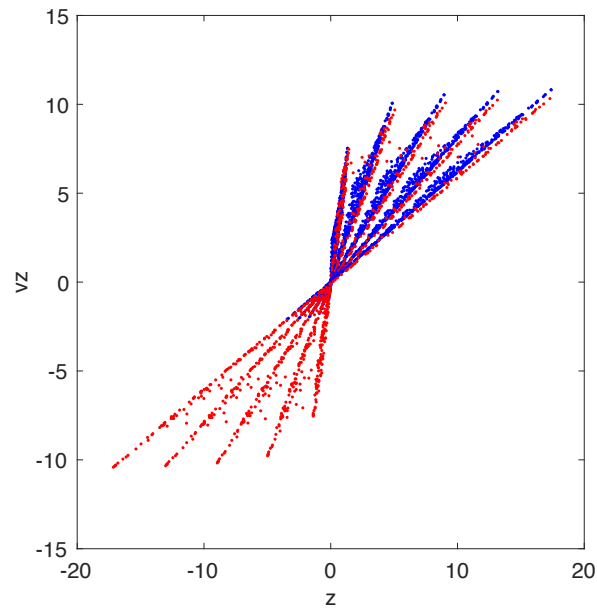
Figure 5.14: Phase space evolution on the axial direction for the same slab of Fig. 5.13.
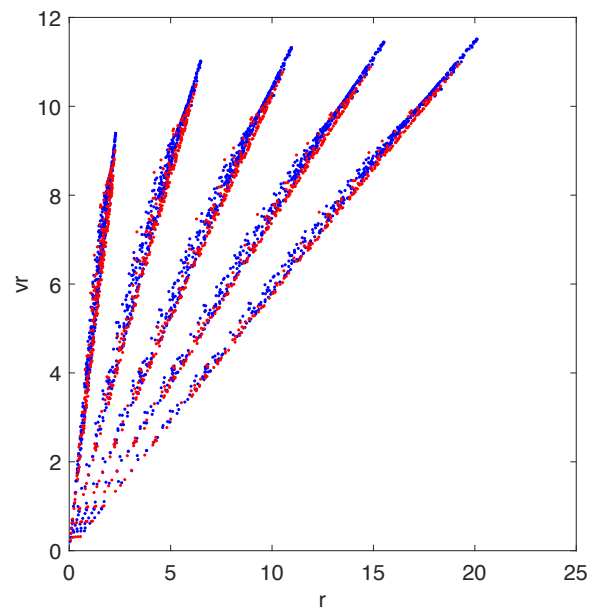
Figure 5.15: Same as Fig. 5.13 but with initial aspect ratio $H/R = 0.1$.
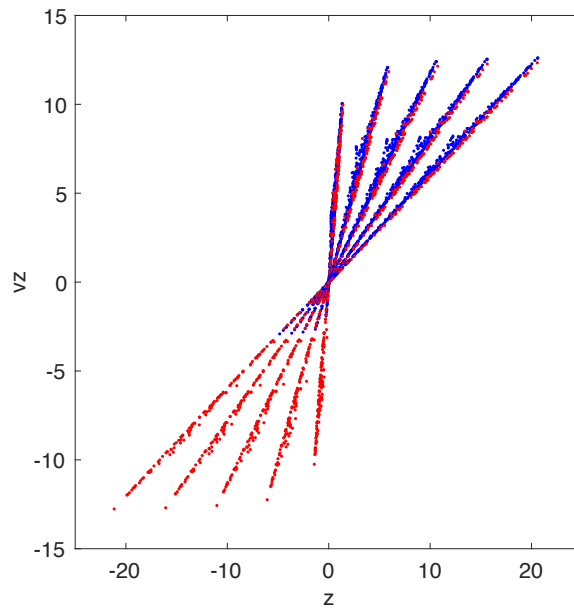
Figure 5.16: Same as Fig. 5.14 but with initial aspect ratio $H/R = 0.1$.
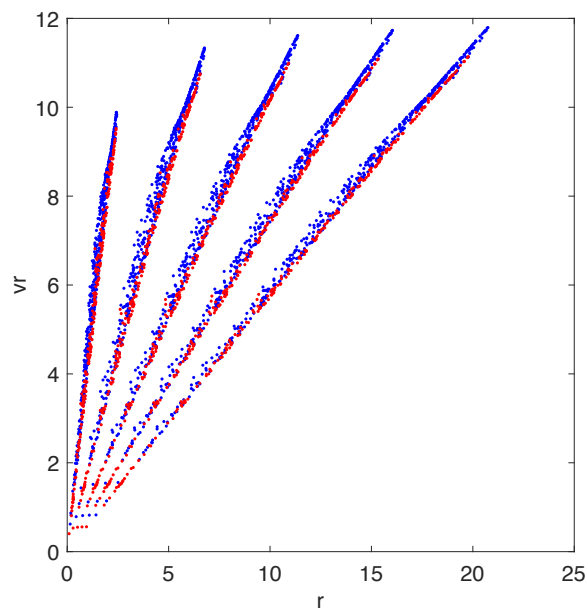
Figure 5.17: Same as Fig. 5.13 but with initial aspect ratio $H/R = 0.01$.
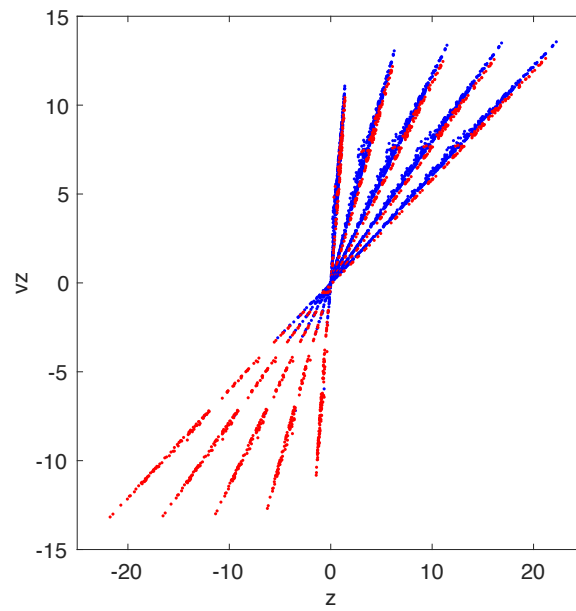
Figure 5.18: Same as Fig. 5.14 but with initial aspect ratio $H/R = 0.01$.
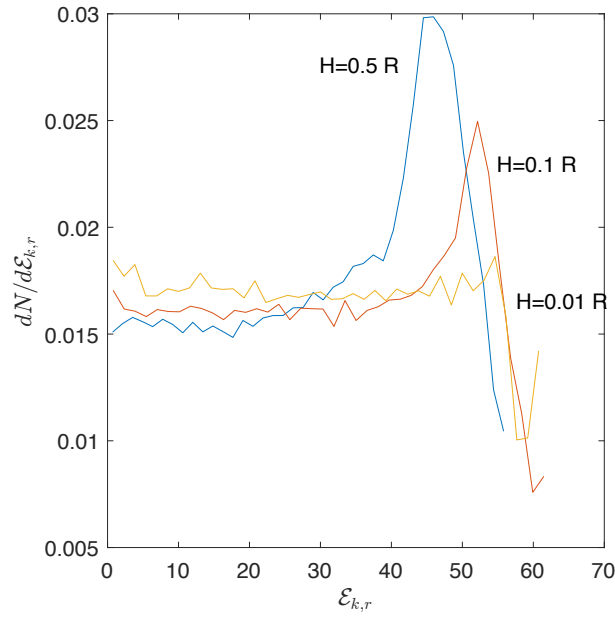
Figure 5.19: Kinetic energy spectra on the radial direction for an hetero-nuclear slab made by an ion mixture $\mu = 0.01$ and varying the initial aspect ratio, results obtained with the PIC code.
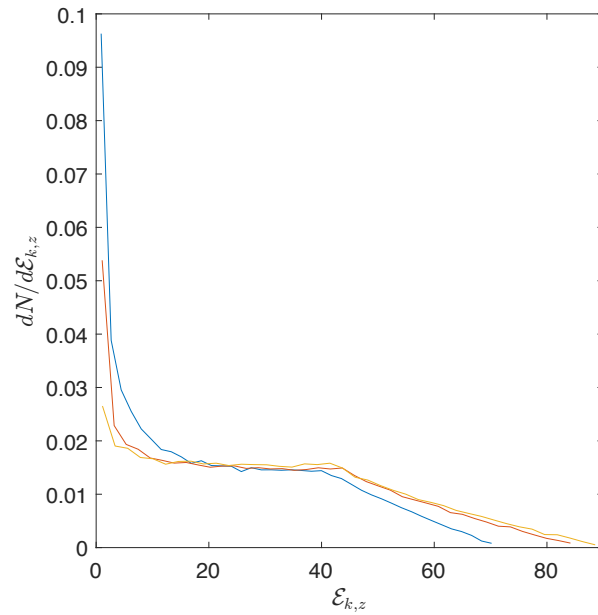
Figure 5.20: Kinetic energy spectra on the axial direction for an hetero-nuclear slab made by an ion mixture $\mu = 0.01$ and varying the initial aspect ratio, results obtained with the PIC code.
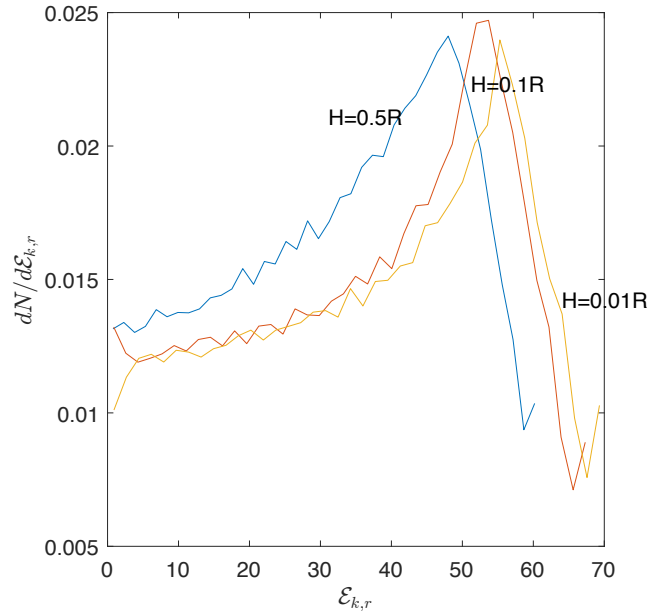
Figure 5.21: Kinetic energy spectra on the radial direction for a double layer target ($\mu = 0.01$) and varying the initial aspect ratio.
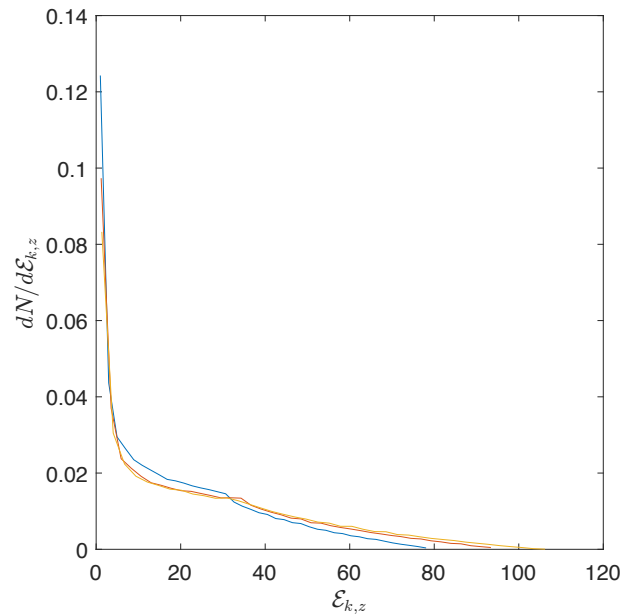
Figure 5.22: Kinetic energy spectra on the axial direction for a double layer target ($\mu = 0.01$) and varying the initial aspect ratio, as in Fig. 5.21.
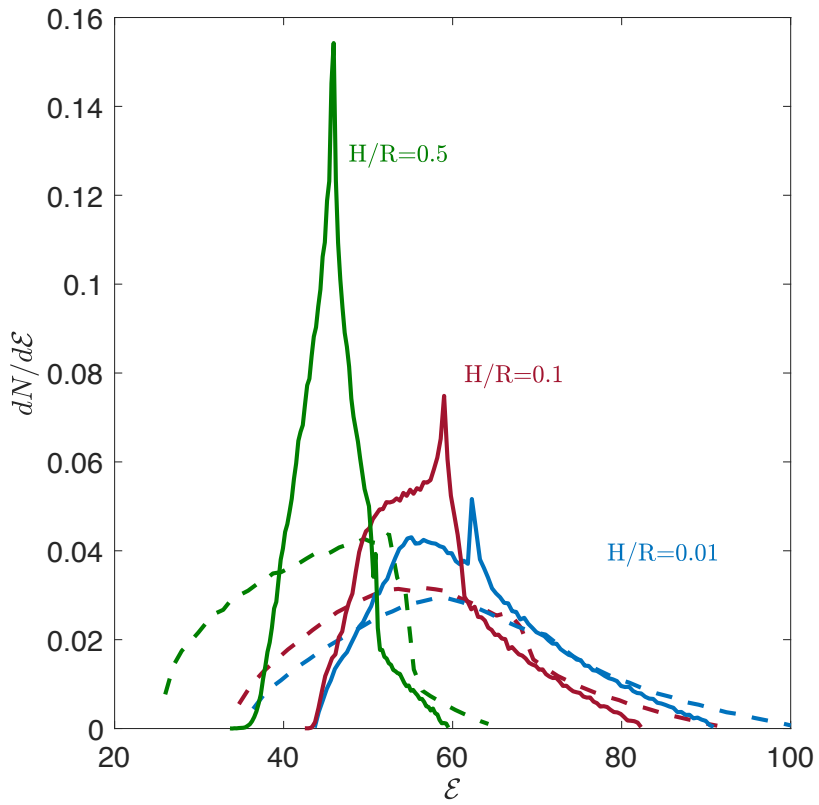
Figure 5.23: Total kinetic energy spectra for the same cylindrical targets of Figs. 5.19, 5.20, 5.21, 5.22. Solid lines for one slab with a mixture and dotted lines for a double-layer target. Results obtained with the PIC code.

5.5   Gaussian and uniform initial distribution

In this last section, we have considered a heterogeneous slab composed by a mixture of two types of ions ($\mu = 0.01$, $\alpha = 0.5$) with two different initial radial space distributions: uniform and Gaussian. The standard deviation of the Gaussian distribution is set in a way that reconstructs a slab with the same initial potential energy of the uniform target. The initial aspect ratio considered is $H/R = 0.1$ and the two species are considered initially at rest. All the simulations were performed with the PIC code in dimensionless units. In Fig. 5.25 the evolution of the positions of the fast species is followed, in a 3D representation, in the case of Gaussian initial distribution, at different times $t = 1/4T_p$, $1/2T_p$, $3/4T_p$, T_p. Figure 5.26 presents the same distribution for a slab with uniform initial distribution. Figs. 5.27, 5.28 depict the velocity distribution of the fast species at $t = 1/2T_p$ and $t = T_p$ superposing results from the Gaussian and uniform initial distribution. We can highlight how the situation is very similar in both cases and the evolution of the expansion does not present huge differences. The evidence of this result is given also by the fast energy spectra 5.24.
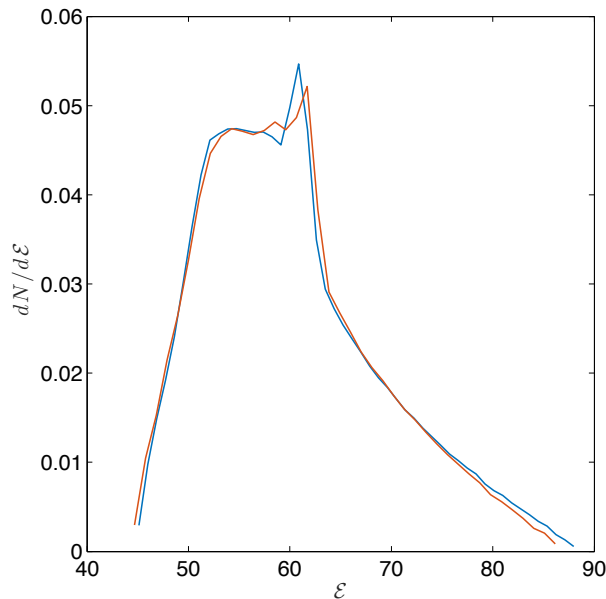
Figure 5.24: Kinetic energy spectra of the fast species for the same slab of Figs. 5.25 5.26, comparing results obtained with two different initial distributions of the ions (Gaussian and uniform).
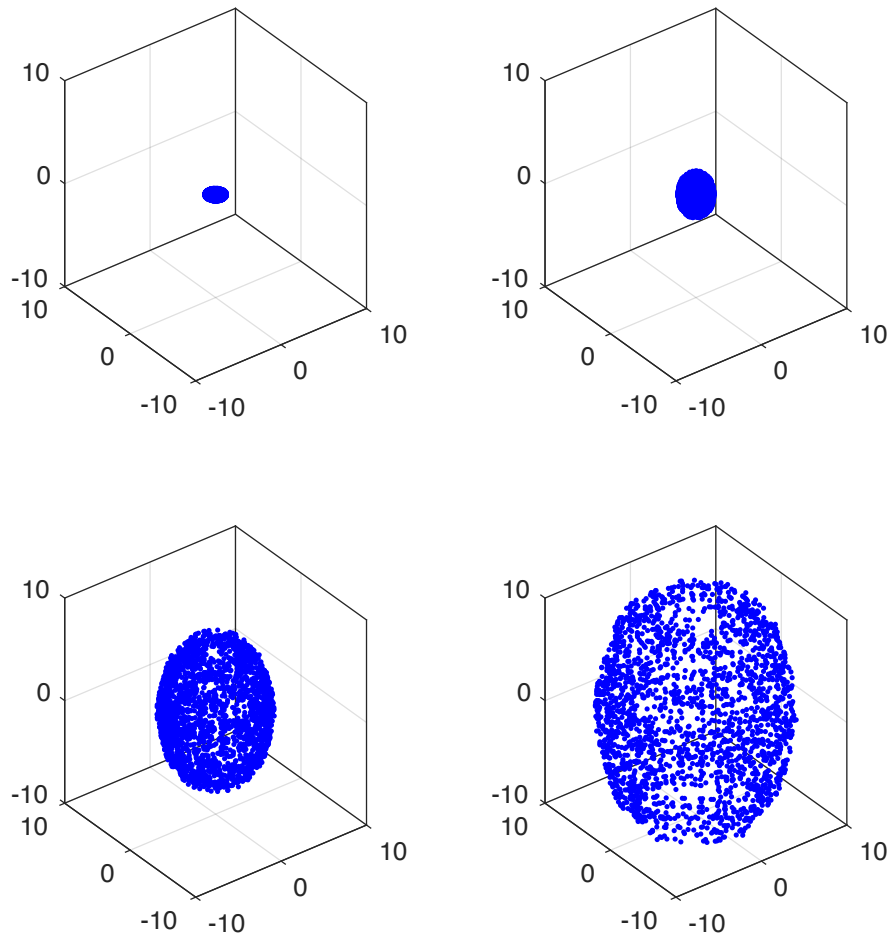
Figure 5.25: Evolution of the positions in a 3D representation for the light particles in a slab with Gaussian initial distribution, results obtained with the PIC code.
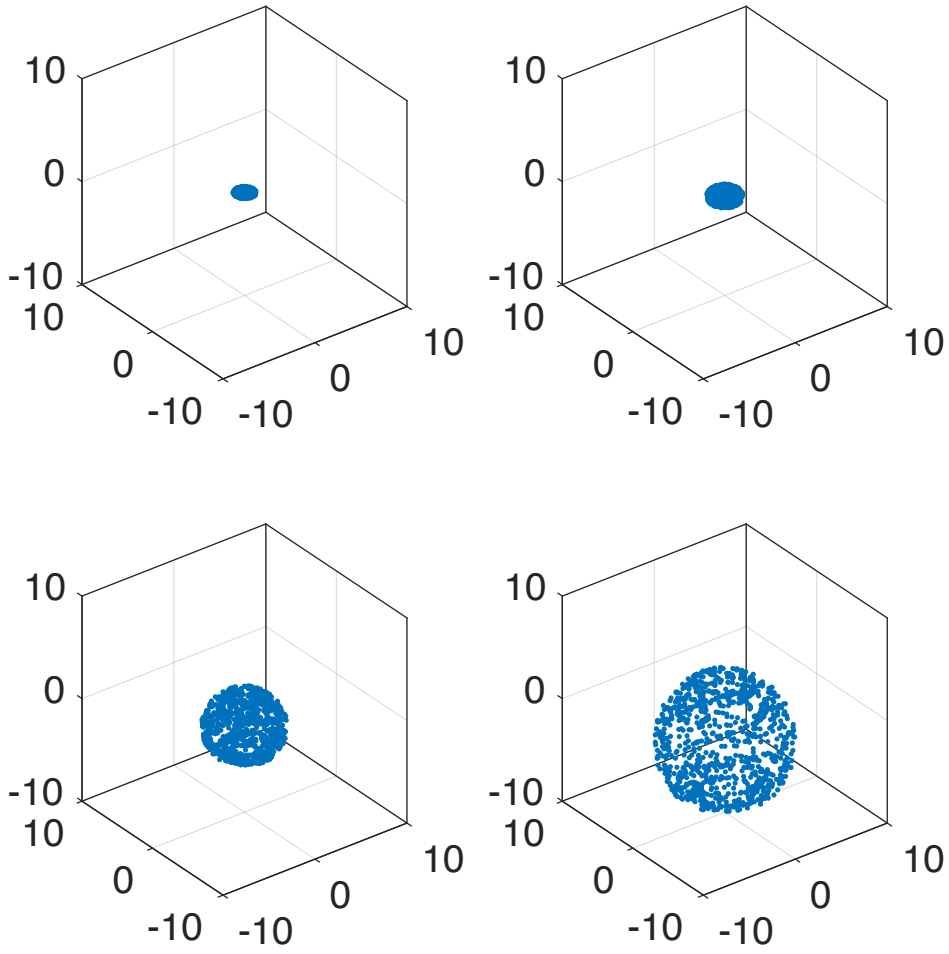
Figure 5.26: Evolution of the positions in a 3D representation for the light particles in a slab with uniform charge inside, results obtained with the PIC code.
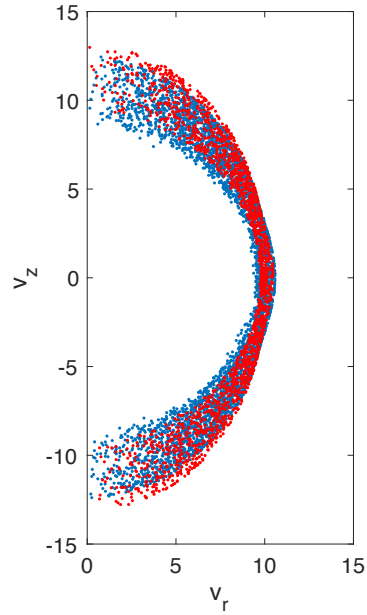
Figure 5.27: Comparison of the velocities distribution of the light species at $t = T_p/2$ for the slab with initial Gaussian distribution, (blue dots) and uniform initial distribution (red dots).
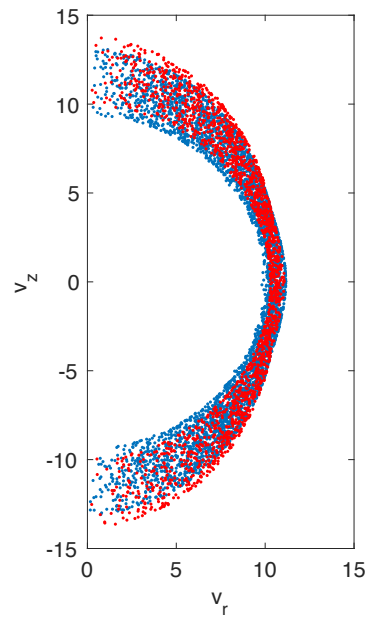
Figure 5.28: Comparison of the velocities distribution of the light species at $t = T_p$ for the slab with initial Gaussian distribution, (blue dots) and uniform initial distribution (red dots).

Chapter 6

Conclusions

In the present thesis, the dynamics of particles during the Coulomb explosion of single ion species and ion mixtures has been examined, paying particular attention to the energy spectrum of the component with the highest charge-to-mass ratio. We consider two possible configurations of the target: spherical nanoclusters and thin cylindrical targets.

In the first case, a theoretical model was developed, due to the radial direction of the motion and the possibility to approximate as a 1D phenomenon. Therefore, a simple way to detect the occurrence of overtakings between fast ions during the expansion was discussed, validating the existence, empirically deduced in a previous work (Li et al., 2007), of a limit value for the fast ions fraction, α_{crit}, under which shocks are present during the expansion. The analysis started with the limit situation of $m_s \to +\infty$ and the calculation of the Hamiltonian of fast particles, rigorously demonstrating the existence of α_{crit}. A discriminant condition was proposed on the derivative of the fast ions asymptotic energy, ϵ_∞, with respect to the initial ion position r_0: when this quantity is negative for some r_0, the hypothesis of no overtaking is no longer valid. When the value α reaches α_{crit} the spectrum becomes narrower and narrower, meaning that the ions tend to acquire very similar velocities, since the spectrum is mono-energetic. The condition $\alpha = \alpha_{crit}$ becomes also the limit situation for the appearing of shock shells. We have demonstrated that most of these considerations are valid also for the general case in which m_s is finite and, in particular, the value of α_{crit} is determinant in the shock rising. The important conclusion gained by this study is that a very narrow energy spectrum drives the occurring of shock shells and not vice versa. Another important feature of nanocluster expansions has been discussed: the mean value of asymptotic energy for the fast species seems to have a linear behavior in function of $\alpha$. Using an extrapolation technique, we demonstrated numerically that this function is not perfectly linear. Whenever a theoretical analysis was not possible, for the presence of overtakings, the shell method was successfully used to depict the expansion and the shock shells presence. The shell method provides exact results also in the presence

of shock shells, when in theory the density could become infinite in some points. The method was very useful in spherical symmetry to investigate the behavior of different mixtures, changing some characteristic parameters as the charge-to-mass ratio of both species and the fraction of fast particles, α. Different mixtures have been tested as H^+D^+, D^+T^+ and H^+C^{n+}; despite the high-quality energy spectrum obtained by the fast species ($\Delta\mathcal{E}/\mathcal{E}$ very low), the peak energy reached is not sufficient in case of practical applications as hadrontherapy, where proton beam at hundred of MeVs are required.

In the second part of the thesis, another type of targets has been studied: thin slab made by ion mixtures or double layer targets. The purpose was to simulate very thin cylindrical slab, with the radius correspondent to the focal spot of the laser which ionize the matter. In the case of cylindrical targets, a theoretical model is not applicable, but an axial symmetry has been supposed and proved to compare results by the three numerical methods developed: a 2D PIC code, a 3D N body algorithm (the Soft-Spheres method) and the 2D ring method. All the tests performed have been proved the effectiveness of the three computational techniques here proposed. In the Soft-Spheres method we do not consider point-like particles: the center of each sphere has tree degrees of freedom for moving, with a fixed value of the radius r_s. The number of soft-spheres used in the method is some order of magnitude smaller than the real particles number, but the formulation of the potential energy interaction between two soft-spheres, which can mutually interpenetrate, guarantees the non collisionality of the system. Despite of the high computational cost of the 3D method, it was advantageous when no hypothesis on the symmetry of the system could be made. In case of the necessity to use a gridless technique in a 2D approach the ring method was beneficial. The method could be completely deduced using a Hamiltonian approach and all the physical quantities (e.g., momentum, energy and angular momentum) are conserved exactly: the only errors are due to time discretization. In particular, the ring method can be very useful to obtain interesting results making use of a simple, easy-to-implement code, valid also when the physical region occupied by the plasma grows dramatically during the simulation. For these reasons, the method can be regarded as a useful tool, in particular to study laser-plasma interactions and to test ore complex codes. Finally, the EXPICYL PIC code was developed; to follow Coulomb explosion phenomena correctly in its formulation an expanding grid is considered and exact boundary conditions on the Poisson solver are imposed. The three numerical techniques were used to simulate different type of cylindrical slab expansions. Homogeneous targets have been considered modifying the aspect ratio of the initial slab, and demonstrating that in the case of thinner slab the preferential direction of expansion is parallel to the axis symmetry of the cylinder. Then, the Coulomb explosion of a homogeneous sphere was compared with the expansion of a cylinder with the same initial potential energy, seeing that after some plasma periods the velocities and positions distributions are similar. The same

result has been obtained for the kinetic energy spectrum. The analysis then focuses on heterogeneous cylindrical targets, made by a mixture of two types of ions. The initial aspect ratio and the fraction of fast particles on the total have been varied, comparing results by the 3D tool and the PIC method. Also in case of cylindrical slab decreasing the parameter α the spectrum becomes narrower. Then the ratio μ, between the two charge-to-mass ratios, was changed, achieving a higher energy peak of the spectrum when μ decreases, probably due to the enhanced acceleration of fast particles in case of heaviest slow ions. The single slab made by an ion mixture was compared with the double-layer target configuration, varying the initial aspect ratio. Results have shown a more peaked behavior of the kinetic energy spectrum in case of an ion mixture, while those types of targets are technologically more difficult to be produced. Finally, the possibility of a different initial charge density was considered, basing on the fact that the laser spot has a Gaussian distribution in space. Therefore, a Gaussian profile of the ions was simulated inside the initial slab. Regarding the kinetic energy spectrum, differences between the peak energy or the energy spread were not relevant.

In future investigations, it can be interesting to include in the analysis also the electron dynamics and the laser cluster interaction mechanism, to have a clearer picture of the explosion.

List of References

M. Abramowitz and I. Stegun. *Handbook of Mathematical Functions with Formulas, Graphs, and Mathematical Tables*. Dover, 1965.

A. A. Andreev, P. V. Nickles, and K. Y. Platonov. Quasi-coulomb explosion of multicomponent laser cluster plasma. *Physics of Plasmas*, 17:023110, 2010.

E. Boella, G. Coppa, A. D'Angola, F. Fiúza, and L. Silva. Use of the shell model for plasma physics simulation. 64th Gaseous Electronics Conference, Salt Lake City (Utah, USA), November 2011.

E. Boella, A. Peiretti Paradisi, B. D'Angola, L. O. Silva, and G. Coppa. Study on Coulomb explosions of ion mixtures. *Journal of Plasma Physics*, 82:905820110, 2016.

E. Boella, G. Coppa, A. D'Angola, and B. Peiretti Paradisi. Gridless particle technique for the Vlasov–Poisson system in problems with high degree of symmetry. *Computer Physics Communications*, 224:136 – 143, 2018.

S. Bulanov, T. Esirkepov, V. Khoroshkov, A. Kuznetsov, and F. Pegoraro. Oncologic al hadrontherapy with laser ion accelerators. *Physics letters A*, 299:240, 2002.

S. Bulanov, A. Brantovand, V. Bychenkov, et al. Accelerating monoenergetic protons from ultrathin foils by flat-top laser pulses in the directed-coulomb-explosion regime. *Physical Review E*, 78:026412, 2008.

S. Bulanov, A. Brantovand, V. Bychenkov, et al. Accelerating protons to therapeutic energies with ultraintense, ultraclean, and ultrashort laser pulse. *Medical Physics*, 35:1770, 2009.

V. N. Bychenkov, V. Yu. Novikov, D. Batani, V. T. Tikhonchuk, and B. S. D. Ion acceleration in expanding multispecies plasmas. *Physics of plasmas*, 11(6):3242, 2004.

V. Y. Bychenkov and V. Kovalev. On the maximum energy of ions in a disintegrating ultrathin foil irradiated by a high-power ultrashort laser pulse. *Quantum Electronics*, 35(12):1143, 2005a.

V. Y. Bychenkov and V. Kovalev. Coulomb explosion in a cluster plasma. *Plasma Physics Reports*, 31(2):178–183, 2005b.

A. D'Angola, E. Boella, and G. Coppa. On the applicability of the collisionless kinetic theory to the study of nanoplasmas. *Physics of Plasmas*, 21:82116, 2014.

J. Dawson. One-dimensional plasma model. *The Physics of Fluids*, 5:445, 1962.

T. Ditmire, T. Donnelly, A. M. Rubenchik, R. W. Falcone, and M. D. Perry. Interaction of intense laser pulses with atomic clusters. *Physical Review A*, 53:3379, 1996.

T. Ditmire, J. W. G. Tisch, E. Springate, M. B. Mason, N. Hay, R. A. Smith, J. Marangos, and M. H. R. Hutchinson. High–energy ions produced in explosions of superheated atomic clusters. *Nature*, 386:54, 1997.

T. Ditmire, J. Zweiback, V. P. Yanovsky, T. E. Cowan, G. Hays, and K. B. Wharton. Nuclear fusion from explosions of femtosecond laser–heated deuterium clusters. *Nature*, 398:489, 1999.

O. Eldridge and M. Feix. One-dimensional plasma model at thermodynamic equilibrium. *The Physics of Fluids*, 5:1076, 1962.

T. Esirkepov, S. Bulanov, et al. Proposed double-later target for the generation of high-quality laser-accelerated ion beams. *Physical review letters*, 89:175003, 2002.

T. Esirkepov, M. Borghesi, S. Bulanov, G. Mourou, and T. Tajima. Highly efficient relativistic-ion generation in the laser-piston regime. *Physical Review Letters*, 92 (17):175003, 2004.

E. Fourkal, I. Velchev, and C. Ma. Coulomb explosion effect and the maximum energy of protons accelerated by high-power lasers. *Phys Rev E, Stat Nonlin Soft Matter Phys*, 2005.

M. Hohenberger, D. R. Symes, K. W. Madison, A. Sumeruk, G. Dyer, A. Edens, W. Grigsby, G. Hays, M. Teichmann, and T. Ditmire. Dynamic acceleration effects in explosions of laser-irradiated heteronuclear clusters. *Physical Review Letters*, 95:195003, 2005.

L. Karsch, E. Beyreuther, W. Enghardt, M. Gotz, U. Masood, U. Schramm, K. Zeil, and J. Pawelke. Towards ion beam therapy based on laser plasma accelerators. *Acta Oncologica*, 56(11):1359–1366, 2017.

V. P. Krainov and A. S. Roshchupkin. Dynamics of the coulomb explosion of large hydrogen iodide clusters irradiated by superintense ultrashort laser pulses. *Physical Review A*, 64:063204, 2001.

L. Landau and E. Lifshitz. *Electrodynamics of Continuous Media, Sect. 2.2.* Pergamon Press, 1984.

I. Last and J. Jortner. Nuclear fusion driven by coulomb explosion of homonuclear and heteronuclear deuterium- and tritium-containing clusters. *Physical Review A*, 64:063201, 2001a.

I. Last and J. Jortner. Nuclear fusion induced by coulomb explosion of heteronuclear clusters. *Physical Review Letters*, 87:033401, 2001b.

I. Last and J. Jortner. Ultrafast high-energy dynamics of thin spherical shells of light ions in the coulomb explosion of heteroclusters. *Physical Review A*, 71:063204, 2005.

H. Li, J. Liu, C. Wang, G. Ni, C. J. Kim, R. Li, and Z. Xu. Two overrun phenomena and their effects on fusion yield in the coulomb explosion of heteronuclear clusters. *Journal of Physics B: Atomic, Molecular and Optical Physics*, 40(19):3941, 2007.

P. Mora. Plasma expansion into a vacuum. *Physical Review Letters*, 90:185002, 2003.

T. Morita, S. V. Bulanov, T. Z. Esirkepov, J. Koga, and M. Kando. Proton acceleration due to anisotropic coulomb explosion of a double-layer target irradiated by an intense laser pulse. *Journal of the Physical Society of Japan*, 81:024501, 2012.

M. Murakami and M. Tanaka. Nanocluster explosions and quasimonoenergetic spectra by homogeneously distributed impurity ions. *Physics of Plasmas*, 15:082702, 2008.

R. Neutze, R. Wouts, D. van der Spoel, E. Weckert, and J. Hajdu. Potential for biomolecular imaging with femtosecond x-ray pulses. *Nature*, 406:752, 2000.

F. Peano, R. Fonseca, and L. O. Silva. Dynamics and control of shock shells in the Coulomb explosion of very large deuterium clusters. *Phys. Rev. Lett.*, 94(3):033401, 2005.

F. Peano, F. Peinetti, R. Mulas, G. Coppa, and L. O. Silva. Kinetics of the collisionless expansion of spherical nanoplasma. *Physical Review Letters*, 96:175002, 2006.

F. Peano, G. Coppa, F. Peinetti, R. Mulas, and L. O. Silva. Ergodic model for the expansion of spherical nanoplasmas. *Physical Review E*, 75:066403, 2007.

K. I. Popov, V. Y. Bychenkov, W. Rozmus, and L. Ramunno. A detailed study of collisionless explosion of single- and two-ion-species spherical nanoplasmas. *Physics of Plasmas*, 17:083110, 2010.

M. Roth, T. Cowan, et al. Fast ignition by intense laser-accelerated proton beams. *Physical review letters*, 86:436, 2001.

Appendix A

This Annex lists the papers published during the Ph.D. activity that have been relevant for the thesis activity. Then, a summary of a side activity of the PhD on metabolic radiotherapy is presented.

Declarations I hereby declare that, the contents and organisation of this dissertation constitute my own original work and does not compromise in any way the rights of third parties, including those relating to the security of personal data. Part of the work described in this Ph.D. dissertation was also previously published in the following Journals.

Study on Coulomb explosions of ion mixtures

E. Boella[1], B. Peiretti Paradisi[2], A. D'Angola[3], G. Coppa[2] and L. O. Silva[1]

[1]GoLP/Instituto de Plasmas e Fusao Nuclear, Instituto Superior Tecnico, Universidade de Lisboa, Avenida Rovisco Pais, 1, Lisbon, Portugal
[2]Dipartimento Energia, Politecnico di Torino, corso Duca degli Abruzzi, 24, Torino, Italy
[3]Scuola di Ingegneria, Universita della Basilicata, via dell'Ateneo Lucano, 10, Potenza, Italy

Abstract

The paper presents a theoretical work on the dynamics of Coulomb explosion for spherical nanoplasmas composed by two different ion species. Particular attention has been dedicated to study the energy spectra of the ions with the larger charge-to-mass ratio. The connection between the formation of shock shells and the energy spread of the ions has been the object of a detailed analysis, showing that under particular conditions the width of the asymptotic energy spectrum tends to become very narrow, which leads to a multi-valued ion phase-space. The conditions to generate a quasi mono-energetic ion spectrum have been rigorously demonstrated and verified by numerical simulations, using a technique that, exploiting the spherical symmetry of the problem, allows one to obtain very accurate and precise results.

1 Introduction

The interaction between sufficiently intense laser pulses and spherical nanoclusters can lead to the complete expulsion of all the electrons from the cluster, as discussed in (Ditmire *et al.*, 1996; Murakami & Mima, 2009; Coppa *et al.*, 2011), and to a consequently rapid explosion of the left-behind ion cloud. The process is a well known mechanism of ion acceleration (Ditmire *et al.*, 1997) with many potential applications, ranging from fusion research (Ditmire *et al.*, 1999) to biomolecular imaging (Neutze *et al.*, 2000). While the explosion of a single species ion plasma leads to a broad energy spectrum (Last & Jortner, 2001*a*; Krainov & Roshchupkin, 2001), it has been verified that in the presence of ion mixtures conditions exist producing a quasi-monoenergetic distribution of

the species having the larger charge-to-mass ratio (Last & Jortner, 2001b, 2005; Hohenberger *et al.*, 2005; Murakami & Tanaka, 2008; Andreev *et al.*, 2010; Last *et al.*, 2009, 2010b). Numerical simulations also pointed out a connection between the monochromaticity of the spectrum and the occurrence of overtakings among faster ions, leading to the formation of shock shells (Popov *et al.*, 2010; Li *et al.*, 2007; Last *et al.*, 2010a).

The present work investigates in detail and from a theoretical point of view the energy spectrum of charged particles accelerated during the Coulomb explosion of ion mixtures. In particular, a mixture composed by two types of ions uniformly distributed is considered. The ions of the two species have masses m_s, m_f and electric charges q_s, q_f, with

$$\gamma = \frac{q_s/m_s}{q_f/m_f} < 1 \ . \tag{1}$$

The ions, which are initially at rest, start moving under the influence of the repulsive electrostatic forces, and the species with a larger charge-to-mass ratio moves faster. In this way, two concentric spherical regions, S_f and S_s, are created having radius $R_f(t)$ and $R_s(t)$ respectively, with $R_s \leqslant R_f$. The sphere S_s contains fast and slow particles and R_s represents the frontline of the slow ions; instead, the spherical shell in S_f outside S_s contains only fast particles. The ion dynamics is different in these two regions, and it is studied in detail in Sect. 2 (inner region) and in Sect. 3 (outer region). The dynamics of the explosion depends strongly on the presence of shock shells. It is proved rigorously that the appearance of shocks depends only on the ratio between the total charge of the fast ions and the one of the slow ions, and not on their masses (Sect. 4). In Sect. 5, by using a Hamiltonian approach the properties of the energy spectra are studied analytically. In particular, a rigorous proof is provided for the existence of a threshold for the generation of shock shells (previously this proof was known only for the limit situation of $m_s \to +\infty$ (Li *et al.*, 2007)), so confirming the results of numerical simulations (Murakami & Mima, 2009). Finally, some conclusions are reported in Sect. 6.

Whenever possible, the properties of the explosions have been deduced analytically, otherwise the study has been performed numerically with the so called "shell method" (Boella *et al.*, 2011; D'Angola *et al.*, 2014), which provides extremely precise results by exploiting the spherical symmetry of the problem.

2   Ion expansion in the inner zone

Initially, all the ions are uniformly distributed inside a sphere of radius R. As the charge density is constant, the radial electric field is linear. Therefore, there will be a uniform expansion for both slow and fast ions, and consequently the charge density will remain constant inside the sphere S_s, producing again a linear behaviour of the electric field. From this consideration, one can infer that the electric field inside S_s remains a linear function of the radius r at any

time:
$$E(r,t) = A(t)r \quad \text{for} \quad r \leqslant R_s(t). \tag{2}$$

Under this assumption, the equations of motion for the fast and the slow ions inside S_s can be written in a simple way. The uniform expansion can be described by introducing two functions, $\xi_s(t)$ and $\xi_f(t)$, such that slow ions and fast ions initially at $r = r_0$ are moved at time t to $r = r_0\xi_s(t)$ and $r = r_0\xi_f(t)$, respectively. Moreover, the initial densities of the two species, $n_{s,0}$ and $n_{f,0}$, evolve in time as

$$n_s(t) = \frac{n_{s,0}}{\xi_s^3(t)}, \; n_f(t) = \frac{n_{f,0}}{\xi_f^3(t)}. \tag{3}$$

Using Gauss's law, the electric field inside the sphere S_s can be written as:

$$E(r,t) = \frac{4\pi}{3}\left(\frac{q_f n_{f,0}}{\xi_f^3(t)} + \frac{q_s n_{s,0}}{\xi_s^3(t)}\right)r, \tag{4}$$

which has the correct dependence on r, as in Eq. (2). After introducing expression (4) into the equations of the motion for fast and slow ions, by writing the acceleration of the ions of the two species as $r_0 d^2\xi_f/dt^2$ and $r_0 d^2\xi_s/dt^2$, one finally obtains

$$\begin{cases} \dfrac{d^2\xi_f}{dt^2} &= \dfrac{4\pi}{3}\dfrac{q_f}{m_f}\left(\dfrac{q_f n_{f,0}}{\xi_f^3} + \dfrac{q_s n_{s,0}}{\xi_s^3}\right)\xi_f, \\[4mm] \dfrac{d^2\xi_s}{dt^2} &= \dfrac{4\pi}{3}\dfrac{q_s}{m_s}\left(\dfrac{q_f n_{f,0}}{\xi_f^3} + \dfrac{q_s n_{s,0}}{\xi_s^3}\right)\xi_s, \end{cases} \tag{5}$$

in which r_0 does not appear.

Equations (5) can be rewritten in a more compact way, as

$$\begin{cases} \dfrac{d^2\xi_f}{dt^2} &= \nu^2\left(\dfrac{\alpha}{\xi_f^3} + \dfrac{\beta(1-\alpha)}{\xi_s^3}\right)\xi_f, \qquad \xi_f(0) = 1, \qquad \dfrac{d\xi_f}{dt}(0) = 0 \\[4mm] \dfrac{d^2\xi_s}{dt^2} &= \nu^2\gamma\left(\dfrac{\alpha}{\xi_f^3} + \dfrac{\beta(1-\alpha)}{\xi_s^3}\right)\xi_s, \qquad \xi_s(0) = 1, \qquad \dfrac{d\xi_s}{dt}(0) = 0 \end{cases} \tag{6}$$

being

$$\nu = \left[\frac{4\pi q_f^2(n_{f,0} + n_{s,0})}{3m_f}\right]^{1/2}, \quad \alpha = \frac{n_{f,0}}{n_{f,0} + n_{s,0}}, \quad \beta = \frac{q_s}{q_f}. \tag{7}$$

The quantity ν represents a characteristic frequency for the fast ion expansion, while $\alpha \in (0,1)$ is the fraction of fast ions in the cluster.

3   Expansion in the outer zone and shock shells

The system of equations (6) describes the dynamics of slow ions during the whole explosion and the motion of fast ions as long as they are inside S_s. A fast ion, initially at $r = r_0 \leq R$, reaches the border of the inner region when $r_0 \xi_f(t) = R\xi_s(t)$. The time the ion crosses the sphere S_s, indicated in the following as $\tau(r_0)$, is obtained by solving the equation

$$\frac{\xi_s(\tau)}{\xi_f(\tau)} = \frac{r_0}{R}. \tag{8}$$

Considering a fast ion initially at r_0, the electric field for $r \geqslant R_s$ can be written as $Q(r,t)/r^2$, where $Q(r,t)$ is the charge in the sphere of radius r at time t; as long as overtakings between fast ions do not occur, $Q(r,t)$ is the sum of the total charge of slow ions and the charge of the fast ions initially inside a sphere of radius r_0:

$$Q(r,t) = Q(r_0,t) = \frac{4\pi}{3}\left(q_s n_{s,0} R^3 + q_f n_{f,0} r_0^3\right). \tag{9}$$

Consequently, for $t > \tau(r_0)$, the equation of motion for a fast ion outside S_s is

$$m_f \frac{\mathrm{d}^2 r}{\mathrm{d}t^2} = -\frac{\partial}{\partial r}\left(\frac{q_f Q(r_0)}{r}\right), \quad r(\tau) = \xi_f(\tau) r_0, \quad \frac{\mathrm{d}r}{\mathrm{d}t}(\tau) = \frac{\mathrm{d}\xi_f}{\mathrm{d}t}(\tau) r_0. \tag{10}$$

Equation (10) can be integrated in order to obtain the asymptotic kinetic energy of the fast ions, ϵ_∞, as

$$\epsilon_\infty = \frac{1}{2} m_f \left\{\frac{\mathrm{d}\xi_f}{\mathrm{d}t}(\tau(r_0)) r_0\right\}^2 + \frac{q_f Q(r_0)}{\xi_f(\tau) r_0}. \tag{11}$$

The energy spectrum of the fast ions, ρ_ϵ, can be written as

$$\rho_\epsilon = \frac{1}{N_f} \frac{\mathrm{d}N_f}{\mathrm{d}\epsilon_\infty} \tag{12}$$

where N_f is the total number of fast ions, while $\mathrm{d}N_f$ represents the number of ions having asymptotic energy in the interval $\mathrm{d}\epsilon_\infty$. Making use of Eqs. (8) and (11), the spectrum can be expressed parametrically as a function of τ, as:

$$\rho_\epsilon(\epsilon_\infty(\tau)) = \frac{4\pi r_0^2(\tau) n_{f,0}}{N_f} \frac{\mathrm{d}r_0/\mathrm{d}\tau}{\mathrm{d}\epsilon_\infty/\mathrm{d}\tau}. \tag{13}$$

As pointed out in a previous work (Li *et al.*, 2007), shock shells arise when the fraction of fast ions, α, is smaller than a critical value, α_{crit}. Typical phase-space evolutions of the fast ions are showed in Fig. 1 for $\alpha > \alpha_{crit}$ and in Fig. 2 for $\alpha < \alpha_{crit}$. In particular, the curves in Fig. 2 show the typical wave-breaking behaviour that indicates the presence of a shock (Kaplan *et al.*, 2003).
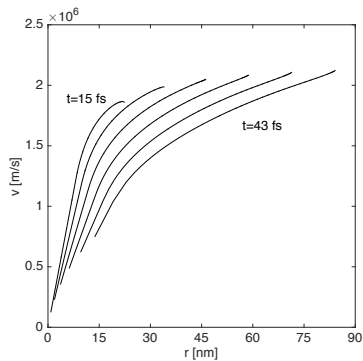
Figure 1: Time evolution of the phase space distribution of fast ions in a mixture C^+H^+ with $\alpha = 0.4$, for t in the range 15-43 fs. A cluster with ion density $n_{f,0}+n_{s,0}=10^{23}$ cm^{-3} and $R = 6.5$ nm has been considered.
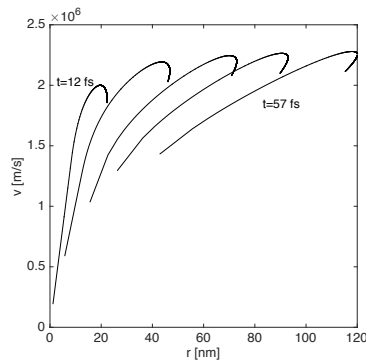
Figure 2: Time evolution of the phase space distribution of fast ions in a mixture C^+H^+ with $\alpha = 0.2$, for t in the range 12-57 fs. A cluster with ion density $n_{f,0}+n_{s,0}=10^{23}$ cm^{-3} and $R = 6.5$ nm has been considered.

In fact, there is a simple way to discriminate Coulomb explosions without shocks from the ones in which this phenomenon appears without requiring a full numerical simulation of the explosion. Starting from Eq. (11), which, in principle, is valid only when shocks are absent, the derivative of ϵ_∞ with respect to r_0 is calculated. If the condition

$$\frac{\mathrm{d}\epsilon_\infty}{\mathrm{d}r_0} > 0 \tag{14}$$

is verified for every $r_0 \in [0, R]$, inner ions take a slower velocity respect to the ones in the outer zones and cannot reach them. In this case, no overtaking is present. Instead, if $\mathrm{d}\epsilon_\infty/\mathrm{d}r_0$ is negative for some r_0, in principle there will be overtakings. Of course, Eq. (11) is no longer valid in this case and it cannot be used to calculate the energy spectrum of fast ions, whose dynamics can be solved only numerically. Using this criterion, the existence of a limit value for α can be readily verified numerically. In general, if $\alpha \in (\alpha_{crit}, 1)$ the derivative $\mathrm{d}\epsilon_\infty/\mathrm{d}r_0$ remains positive and no shock is formed; for $\alpha \in (0, \alpha_{crit})$, $\mathrm{d}\epsilon_\infty/\mathrm{d}r_0$ changes its sign, meaning that the fast particles overtake each other, giving rise to shock shells. The calculations show that α_{crit} depends only on the ratio between the ions charges and it is independent of their masses (Li *et al.*, 2007). In particular, $\alpha_{crit} = 1/3$ for mixtures HD, HT, DT and HC^+.

4 Theoretical derivation of α_{crit}

Starting with the case of no shock, by indicating with Q_s and Q_f the total charge of slow and fast ions, the dynamics of a fast ion initially at $r = r_0$ is governed by the Hamiltonian

$$\mathcal{H}(r, p_r; r_0) = \frac{p_r^2}{2m_f} + \frac{q_f Q_f}{r} \left(\frac{r_0}{R}\right)^3 + q_f \Phi_s(r, R_s(t)), \tag{15}$$

where $\Phi_s(r, \rho)$ is the electrostatic potential in r due to fixed ions uniformly distributed in a sphere of radius ρ:

$$\Phi_s(r, \rho) = \begin{cases} \dfrac{3Q_s}{2\rho} - \dfrac{Q_s r^2}{2\rho^3} & \text{for} \quad r \leqslant \rho, \\[3mm] \dfrac{Q_s}{r} & \text{for} \quad r \geqslant \rho. \end{cases} \tag{16}$$

In the limit situation $m_s \to +\infty$, $R_s(t)$ is constant and equal to R. Consequently, as $\mathcal{H}$ does not depend explicitly on time, it is a constant of motion, and the asymptotic energy ϵ_∞ expressed as a function of r_0 can be written immediately as

$$\epsilon_\infty(r_0) = q_f \left[\frac{Q_f - Q_s/2}{R^3} r_0^2 + \frac{3Q_s}{2R}\right], \tag{17}$$

from which the energy spectrum can be readily calculated (Li *et al.*, 2007; Murakami & Mima, 2009).

Two situations can occur, depending on the sign of $Q_f - Q_s/2$. If $Q_f > Q_s/2$ the ion velocity is an increasing function of r_0, so overtakings do not occur, and the analytic spectrum is correct, as shown in Fig. 3, curves a, b, c. When $Q_f < Q_s/2$, according to Eq. (17), ϵ_∞ is a decreasing function of r_0, but this implies that the ions closer to the center of the cluster are bound to overtake the ions close to the border of the sphere. In other words, the hypothesis of no overtakings, and consequently Eq. (17), are no longer valid. In Fig. 3, curves e, f, g, the energy spectra have been calculated correctly by using the shell method. The case $Q_f = Q_s/2$ (Fig. 3, curve d) can be considered as a limit for $Q_f - Q_s/2 \to 0^+$ and, consequently, Eq. (17) can still be used. In the general case, where the mass of slow ions is finite, in the Hamiltonian (15) the potential due to slow ions, Φ_s, is a function of time, as it depends on the frontline $R_s(t)$, and $\mathcal{H}$ is no longer a constant of motion:

$$\frac{d\mathcal{H}}{dt} = \frac{\partial \mathcal{H}}{\partial t} = q_f \frac{\partial \Phi_s}{\partial R_s} \frac{dR_s}{dt}. \tag{18}$$

In principle, the value of the asymptotic energy can be obtained by integrating Eq. (18) in time:

$$\epsilon_\infty = \mathcal{H}(t \to +\infty) = \mathcal{H}(t = 0) + q_f \int_0^{\tau(r_0)} \frac{\partial \Phi_s}{\partial R_s}(r(t), R_s(t)) \frac{dR_s}{dt} dt \tag{19}$$
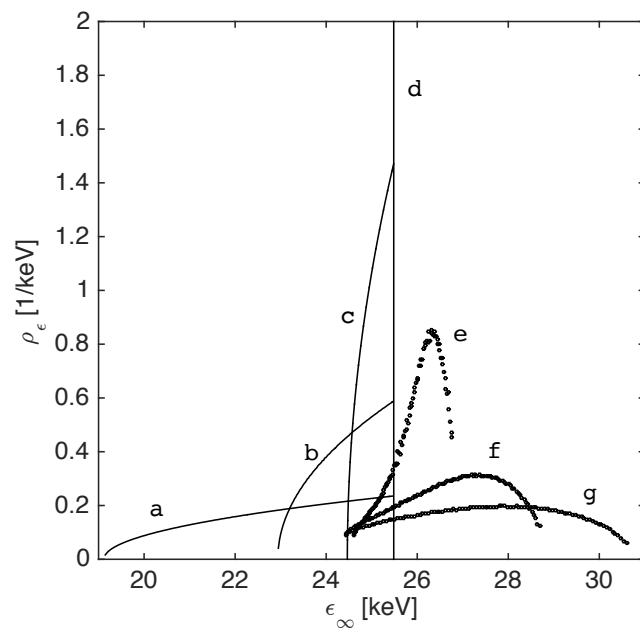
Figure 3: Energy spectra of a mixture with slow ions at rest ($m_s \to +\infty$) and Hydrogen ions, for different value of α in the range $[0.2, 0.5]$. The same initial density and radius as in Fig. 1 have been considered. Curves a, b and c represent mixtures with $\alpha > \alpha_{crit}$; in absence of shocks the numerical spectra correspond to the analytic curve. The limit case of $\alpha = \alpha_{crit}$ is shown in curve d, where the energy spectra is singular. Curves e, f and g display situations with $\alpha > \alpha_{crit}$, for which the spectra have been computed by means of the shell method.

where the upper integration limit can be set equal to $\tau(r_0)$, as for $t > \tau$ the ion is outside $S_s(t)$ and the term $\partial \Phi_s / \partial R_s$ vanishes. Noticing that $\mathscr{H}(t = 0)$ is equal to the asymptotic energy for fixed slow ions, Eq. (15), and expressing $r(t)$ and $R_s(t)$ as functions of ξ_f and ξ_s, one finally obtains

$$\epsilon_\infty = q_f \left[\frac{Q_f - Q_s/2}{R^3} r_0^2 + \frac{3Q_s}{2R} \right] - \frac{3Q_s q_f}{2R} I(r_0) \tag{20}$$

where $I(r_0)$ is defined as

$$I(r_0) = \int_0^{\tau(r_0)} \left[1 - \left(\frac{r_0 \xi_f(t)}{R \xi_s(t)} \right)^2 \right] \frac{\xi_s'(t)}{\xi_s^2(t)} \mathrm{d}t. \tag{21}$$

The quantity I is always non negative, and, in fact, the motion of slow ions takes some energy away from the fast ones.

The condition $\mathrm{d}\epsilon_\infty / \mathrm{d}r_0 > 0$ for $r_0 \in [0, R]$ is now investigated. Starting from Eq. (21), one obtains:

$$\frac{\mathrm{d}I}{\mathrm{d}r_0} = \frac{\xi_s'(\tau)}{\xi_s(\tau)^2} \left(1 - \frac{r_0^2 \xi_f(\tau)^2}{R^2 \xi_s(\tau)^2} \right) \frac{\mathrm{d}\tau}{\mathrm{d}r_0} - \int_0^{\tau(r_0)} \frac{2r_0 \xi_f^2 \xi_s'}{R^2 \xi_s^4} \mathrm{d}t. \tag{22}$$

From this formula, considering that $\mathrm{d}\tau / \mathrm{d}r_0 < 0$, one has

$$\frac{\mathrm{d}I}{\mathrm{d}r_0}(r_0) \leqslant 0 \quad \forall r_0 \in [0, R], \quad \frac{\mathrm{d}I}{\mathrm{d}r_0}(R) = 0. \tag{23}$$

Being

$$\frac{d\epsilon_\infty}{dr_0} = 2q_f \frac{Q_f - Q_s/2}{R^3} r_0 - \frac{3Q_s q_f}{2R} \frac{\mathrm{d}I}{\mathrm{d}r_0}, \tag{24}$$

if $Q_f > Q_s/2$ the derivative $\mathrm{d}\epsilon_\infty / \mathrm{d}r_0$ is always non negative, as it is the sum of two non-negative quantities. Instead, if $Q_f < Q_s/2$ a sum of a negative term and a non negative term is present in (24), and in principle nothing can be said about the sign of $\mathrm{d}\epsilon_\infty / \mathrm{d}r_0$ for a generic r_0. However, $\mathrm{d}I / \mathrm{d}r_0$ vanishes for $r_0 = R$, and therefore $\mathrm{d}\epsilon_\infty / \mathrm{d}r_0(R)$ must be negative; consequently, in this case there are overtakings.

In summary, the condition $Q_f = Q_s/2$ is valid in any case and can be used in order to discriminate between explosions with and without shocks. This is the rigorous proof of a property of the Coulomb explosions of mixtures that was found numerically in a previous work (Li *et al.*, 2007). The condition $Q_f = Q_s/2$ provides the critical value of α:

$$\alpha_{crit} = \frac{\beta}{2 + \beta} , \tag{25}$$

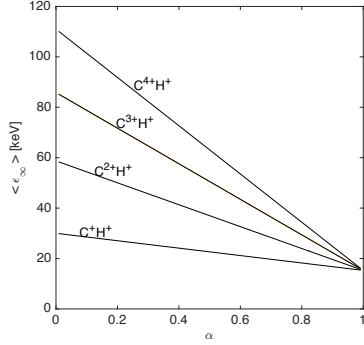which depends only on the charge ratio.

Figure 4: Mean value of the asymptotic energy for different mixtures Carbon-Hydrogen, as a function of the fraction of fast ions.
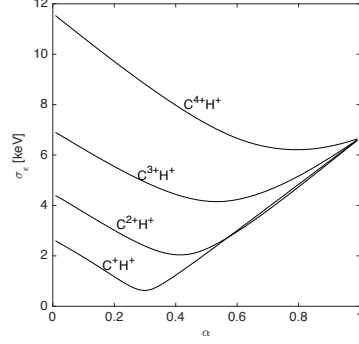
Figure 5: Standard deviation of the energy spectra as a function of the fraction of fast ions, for different mixtures Carbon-Hydrogen.

5 Energy spectrum of the fast ions

The analysis performed for the simplified situation of $m_s \to +\infty$ suggest that fast ion spectra could be particularly narrow when α approaches α_{crit}. To confirm that, a full set of calculations has been carried out for the mixtures C^+H^+, $C^{2+}H^+$, $C^{3+}H^+$ and $C^{4+}H^+$. Clusters with ion density $n_{f,0}+n_{s,0}=10^{23}$ cm^{-3} and $R = 6.5$ nm (as in Figs. 1-3) have been considered. In Figs. 4 and 5 the mean value of the energy and the energy spread have been calculated for each type of mixture for $\alpha \in (0,1)$. Moreover, in Figs. 6-9 the energy spectra are reported for each mixture for α close to α_{crit}. All the calculations have been performed with the shell method.

The plots of the mean ion energy, $\langle \epsilon_\infty \rangle = \int_0^{+\infty} \epsilon \rho_\epsilon(\epsilon) d\epsilon$, as function of α, show a linear behaviour. In fact, the total kinetic energy of the fast ions, $\mathscr{E}_f$, can be written as the difference between the potential energy at $t = 0$ ad the total kinetic energy of the slow ions

$$\mathscr{E}_f = \mathcal{U}(t=0) - \mathscr{E}_s = \frac{3(Q_s + Q_f)^2}{2R} - \frac{3}{5}N_s\frac{m_s}{2}[R\xi'_s(+\infty)]^2 \qquad (26)$$

and, therefore, it does not depend on the possible presence of shocks.

From the numerical solution of system (5), it has been found out that $[\xi'_s(+\infty)]^2$ depends linearly on α, and using this result the average kinetic energy $\langle \epsilon_\infty \rangle = \mathscr{E}_f/N_f$ becomes a linear function of α.

The standard deviation of the energy of fast ions, $\sigma_\epsilon = [\int_0^{+\infty} (\epsilon - \langle \epsilon_\infty \rangle)^2 \rho_\epsilon d\epsilon]^{1/2}$, presents a minimum for a value of α which is close to α_{crit} when $(m_s/q_s)/(m_f/q_f) \gg 1$. In fact, for $\alpha \simeq \alpha_{crit}$ the spectrum has a large plateau and a sharp peak.

Figure 6: Energy spectra of a mixture C^+H^+ with different values of α in the range $[0.2, 0.4]$. The thick curve indicates the distribution with the minimum value of σ_ϵ.
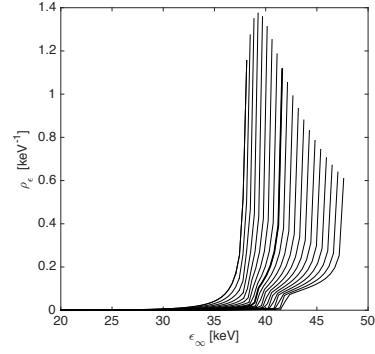
Figure 7: Energy spectra of a mixture $C^{2+}H^+$ with different values of α in the range $[0.3, 0.5]$. The thick curve indicates the distribution with the minimum value of σ_ϵ.

Figure 8: Energy spectra of a mixture $C^{3+}H^+$ with different values of α in the range $[0.45, 0.65]$. The thick curve indicates the distribution with the minimum value of σ_ϵ.
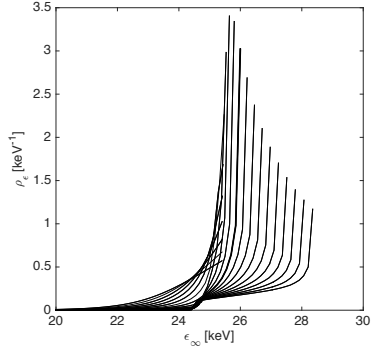

Figure 9: Energy spectra of a mixture $C^{4+}H^+$ with different values of α in the range $[0.7, 0.9]$. The thick curve indicates the distribution with the minimum value of σ_ϵ.
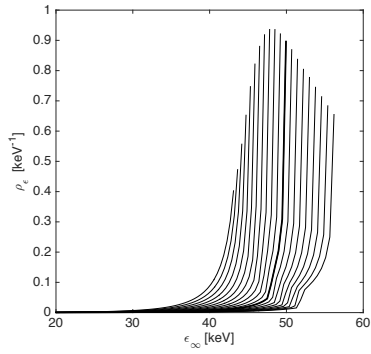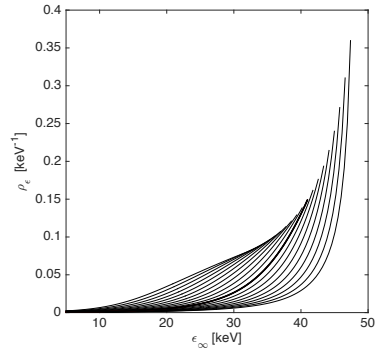
Probably, the plateau gives a non negligible contribution to σ_ϵ, while for practical applications the presence of the peak and its energy spread are more important.

6   Summary

In the paper, the dynamics of particles during the Coulomb explosion of ion mixtures has been investigated, with particular interest to the energy spectrum of the component with the larger charge-to-mass ratio. Exploiting the hypothesis of no overtakings among ions of the same species and the new approach based on the linear behavior for the electric field inside the inner sphere, S_s, containing both slow and fast ions, analytical formulas describing the acceleration both inside and outside S_s (where only fast ions are present), have been derived together with the energy spectrum. For the first time (at least to the Authors' knowledge), a simple way to deduce if overtakings between fast ions will take place during the expansion is presented and discussed, confirming the existence, empirically deduced in a previous work by using numerical simulations (Li et $al.$, 2007), of a limit value for the mixture composition, α_{crit}, above which no shocks are forming. The analysis here proposed is based on the calculation of the derivative of ϵ_∞ with respect to the initial ion position r_0: when this quantity is negative for some r_0, the hypothesis of no overtaking is no longer valid. Moreover, making use of the Hamiltonian of fast particles and starting with the simple case where the mass of the slow species is considered infinite, a rigorous proof of the existence of α_{crit}, which is valid for every value of m_f and m_s, has been obtained. In the limit situation of $m_s \to +\infty$, when $\alpha > \alpha_{crit}$ approaches the critical value, the energy spectrum becomes narrower and narrower, meaning that the ions tend to acquire very similar velocities, and for $\alpha = \alpha_{crit}$ the spectrum becomes monoenergetic. On the other hand, the condition $\alpha = \alpha_{crit}$ is the limit situation for the rising of shock shells. As most of these considerations are valid also for the general case in which m_s is finite, one can conclude that the rising of shock shells is induced by a very narrow energy spectrum, and not vice versa.

In conclusion, conditions to obtain nearly monoenergetic ions from Coulomb explosions of heteronuclear clusters have been individuated and supported by a rigorous theoretical analysis. The analysis has been carried out supposing that the electrons are completely expelled from the cluster; also in order to explain recent experimental results (Hohenberger et $al.$, 2005; Iwan et $al.$, 2012), future investigation should take into proper account also the electron dynamics and the laser-cluster interaction in order to have a clearer picture of the phenomenon.

Gridless particle technique for the Vlasov-Poisson system in problems with high degree of symmetry

E. Boella[1], G. Coppa[2], A. D'Angola[3], and B. Peiretti Paradisi[4]

[1]Center for Mathematical Plasma Astrophysics, KU Leuven, Leuven, Belgium
[2]Dipartimento di Elettronica e Telecomunicazioni, Politecnico di Torino, Torino, Italy
[3]Scuola di Ingegneria, Università della Basilicata, Potenza, Italy
[4]Dipartimento Energia, Politecnico di Torino, Torino, Italy

January 24, 2019

Abstract

In the paper, gridless particle techniques are presented in order to solve problems involving electrostatic, collisionless plasmas. The method makes use of computational particles having the shape of spherical shells or of rings, and can be used to study cases in which the plasma has spherical or axial symmetry, respectively. As a computational grid is absent, the technique is particularly suitable when the plasma occupies a rapidly changing space region.

1 Introduction

The work investigates the possibility of using gridless particle techniques [1, 2] in the study of plasmas which are produced by laser-matter interaction with the purpose of accelerating positive ions. Avoiding to introduce a computational grid is useful in situations (as for plasma expansions and explosions), in which the physical domain occupied by the particles increases rapidly in time. In this framework, in general situations one could employ a set of computational particles and directly calculate the electric field acting on each of them, as the sum of the contribution of the other particles. This requires an extremely high computational effort, unless the problem under exam presents some symmetry. In the work, the cases of spherical and axial symmetry are considered. In the first case (Sect. 2), the problem is essentially one dimensional and computational particles are in the shape of spherical shells. By using the Gauss's formula, the electric field is readily evaluated. For the second case (Sect. 3), particles are

123

modeled as thin circular rings, which are characterized by their radii and their axial coordinates. In this case, the evolution of the force acting on each particle requires necessarily the calculation of the sum of contributions due to the other particles. Although some advantages which are present in the spherical case are lost, the technique here presented conserves interesting features also in this case. Results for both cases are shown and they are compared with exact calculations (when available) or with Particle-In-Cell simulations.

2 The shell method

This Section presents in a complete, rigorous way the method of the shells, which was already introduced and employed with different formulations by other Authors (in particular, in refs. [1, 2, 3]).

2.1 First formulation

In its simplest formulation, a set of N computational particles is considered. After initializing their coordinates $\mathbf{x}_i$ and momenta $\mathbf{p}_i$, the particle are ordered according to their radial coordinates $r_i = |\mathbf{x}_i|$, so that $r_j > r_i$ if $j > i$. Then the radial electric field acting on each particle is evaluated simply as:

$$\mathbf{E}_i = \left(\sum_{j=1}^{i-1} q_j + \tfrac{1}{2} q_i \right) \frac{\mathbf{x}_i}{r_i^3},\tag{1}$$

by using the Gauss's formula and taking advantage of the spherical symmetry of the problem. The presence of the factor $\frac{1}{2}$ multiplying q_i can be explained in a simple way by considering that, for $r = r_i - \epsilon$ $(\epsilon \to 0^+)$ q_i does not contribute to the electric field, while for $r = r_i + \epsilon$ the total charge to be evaluated is $\sum_{j=1}^{i} q_j$. Thus, by supposing a linear behavior of $\mathbf{E}$ at the interface, the factor $\frac{1}{2}$ provides the correct value of the field (a rigorous proof of the formula is presented in Sect. 2.4). Finally, after evaluating $\mathbf{E}$ on each computational particle, the equations of motion:

$$\begin{cases} \frac{\mathrm{d}\mathbf{x}_i}{\mathrm{d}t} = \frac{\mathbf{p}_i}{m_i}, \\ \frac{\mathrm{d}\mathbf{p}_i}{\mathrm{d}t} = q_i \mathbf{E}_i(\mathbf{x}_1, \mathbf{x}_2, ..., \mathbf{x}_N), \end{cases}\tag{2}$$

can be solved by using a suitable numerical technique (e.g., the leapfrog or the Runge-Kutta method), using a time step much smaller with respect to the inverse of the plasma frequency.

2.2 Second formulation

The technique described above is very simple (for example, a MATLAB code can be implemented in few lines of program), but it is excessively memory and time consuming, as it does not take fully advantage of the symmetry of the problem.

In fact, in a central field of forces, the trajectory of each particle takes place on a plane. Therefore, the motion is essentially a two-dimensional problem. This fact suggests a new, simpler formulation of the method. After generating the initial 3D coordinates $\mathbf{x}_i$ and momenta $\mathbf{p}_i$, a set of 2D coordinates $\mathbf{X}_i$ and $\mathbf{P}_i$ is defined as

$$\begin{cases} \mathbf{X}_i = (r_i, 0), & i = 1, 2, ..., N, \\ \mathbf{P}_i = \left(\mathbf{p}_i \cdot \frac{\mathbf{x}_i}{r_i}, \left| \mathbf{p}_i - \left(\mathbf{p}_i \cdot \frac{\mathbf{x}_i}{r_i} \right) \frac{\mathbf{x}_i}{r_i} \right| \right). \end{cases} \tag{3}$$

After that, the method is completely identical to the previous formulation, but it uses only 2D vectors. More in detail, the particles are ordered according to the radial position $R_i = |\mathbf{X}_i|$, the electric field is evaluated as

$$\mathbf{E}_i = \left(\sum_{j=1}^{i-1} q_j + \tfrac{1}{2} q_i \right) \frac{\mathbf{X}_i}{R_i^3}, \tag{4}$$

and the evolution of the system is governed by the equations

$$\begin{cases} \frac{\mathrm{d}\mathbf{X}_i}{\mathrm{d}t} = \frac{\mathbf{P}_i}{m_i}, \\ \frac{\mathrm{d}\mathbf{P}_i}{\mathrm{d}t} = q_i \mathbf{E}_i(\mathbf{X}_1, \mathbf{X}_2, ..., \mathbf{X}_N). \end{cases} \tag{5}$$

2.3 Third formulation

Starting form the Lagrangian

$$\mathscr{L}(r, \varphi, \dot{r}, \dot{\varphi}, t) = \frac{m}{2} \left(\dot{r}^2 + r^2 \dot{\varphi}^2 \right) - q\Phi(r, t), \tag{6}$$

for a single particle in a central potential (Φ depends on t due to the interaction with the other particles of the plasma), one can obtain the Hamiltonian

$$\mathscr{H}(r, \varphi, p_r, p_\varphi, t) = \frac{1}{2m} \left(p_r^2 + \frac{p_\varphi^2}{r^2} \right) + q\Phi(r, t), \tag{7}$$

and the equations of the motion

$$\begin{cases} \frac{\mathrm{d}r}{\mathrm{d}t} = \frac{p_r}{m}, & \frac{\mathrm{d}\varphi}{\mathrm{d}t} = \frac{p_\varphi}{mr^2}, \\ \frac{\mathrm{d}p_r}{\mathrm{d}t} = -q\frac{\partial\Phi}{\partial r} + \frac{p_\varphi^2}{mr^3}, & \frac{\mathrm{d}p_\varphi}{\mathrm{d}t} = 0. \end{cases} \tag{8}$$

In other terms, as it is well known, for a central potential there is a constant of the motion, p_φ, which corresponds to the axial angular momentum, and the motion in radial direction is essentially one-dimensional. This suggests a third way of studying the dynamics of these systems. Starting again from the set $\{\mathbf{x}_i, \mathbf{p}_i\}$ one can calculate

$$r_i = |\mathbf{x}_i|, \qquad p_{r,i} = \mathbf{p}_i \cdot \frac{\mathbf{x}_i}{r_i}, \qquad p_{\varphi,i} = r_i \left| \mathbf{p}_i - p_{r,i} \frac{\mathbf{x}_i}{r_i} \right|. \tag{9}$$

Then, the radial electric field is evaluated as

$$E_{r,i} = \left(\sum_{j=1}^{i-1} q_j + \tfrac{1}{2} q_i \right) \frac{1}{r_i^2} \tag{10}$$

(of course, particles must be sorted according to r_i), and the equations of the motion assume the form:

$$\begin{cases} \frac{\mathrm{d}r_i}{\mathrm{d}t} = \frac{p_{r,i}}{m_i}, \\ \frac{\mathrm{d}p_{r,i}}{\mathrm{d}t} = q_i E_{r,i}(r_1, r_2, ..., r_N) + \frac{p_{\varphi,i}^2}{m_i r_i^3}, \end{cases} \tag{11}$$

in which the $p_{\varphi,i}$'s are constants of the motion and they are fixed by the initial conditions. This last formulation is the most convenient in terms of memory usage and computational effort. However, the presence of the term $p_\varphi^2/(mr^3)$ in Eqs. (11) require a special care when $r \to 0$. All things considered, the second formulation represents a good compromise in terms of computational efficiency and simplicity.

2.4 Interaction between shells

Due to symmetry, each computational particle can be regarded as a spherical surface (a "shell") on which the electric charge is distributed uniformly. The points on the surface move according to different trajectories, all sharing the same radial coordinate, $r(t)$, and the same angular momentum p_φ. For simplicity, a system made of only two shells (having charge q_1 and q_2 and radii r_1 and r_2, with $r_1 < r_2$) is considered now. As the electric field is given by

$$E(r) = \begin{cases} 0, & r < r_1, \\ \frac{q_1}{r^2}, & r_1 < r < r_2, \\ \frac{q_1 + q_2}{r^2}, & r > r_2, \end{cases} \tag{12}$$

the electrostatic energy U can be readily evaluated, as

$$U(r_1, r_2) = \int_{\mathbb{R}^3} \frac{E^2}{8\pi} \, \mathrm{d}^3\mathbf{x} = \frac{q_1^2}{2r_1} + \frac{q_2^2 + 2q_1 q_2}{2r_2}. \tag{13}$$

If r_1 is changed of δr_1, the change $-\delta U$ of the energy is equal to the work $q E_1 \cdot \delta r_1$ of the field on the shell itself. In other terms, one has:

$$E_1 = -\frac{1}{q_1} \frac{\partial U}{\partial r_1} = \frac{\tfrac{1}{2} q_1}{r_1^2}. \tag{14}$$

Similarly, the field acting on the second shell can be calculated as

$$E_2 = -\frac{1}{q_2} \frac{\partial U}{\partial r_2} = \frac{q_1 + \tfrac{1}{2} q_2}{r_2^2}. \tag{15}$$

In both cases, the value of the electric field is in agreement with the rule "$\sum\limits_{j=1}^{i-1} q_j + \frac{1}{2}q_i$", which was introduced previously.

Now the dynamics of the two shells is considered. If there is no crossing (i.e., no collisions) between shells, r_1 is always smaller than r_2 and one has

$$\frac{\mathrm{d}p_1}{\mathrm{d}t} = q_1 \frac{\frac{1}{2}q_1}{r_1^2} \quad , \quad \frac{\mathrm{d}p_2}{\mathrm{d}t} = q_2 \frac{q_1 + \frac{1}{2}q_2}{r_2^2}. \tag{16}$$

Here only radial motion is considered for simplicity (i.e., $p_\varphi = 0$ for both shells). The two equations (16) can be also written as

$$\begin{cases} \dfrac{\mathrm{d}p_1}{\mathrm{d}t} = -\dfrac{\partial}{\partial r_1}\left(\dfrac{\frac{1}{2}q_1^2}{r_1}\right), \\ \dfrac{\mathrm{d}p_2}{\mathrm{d}t} = -\dfrac{\partial}{\partial r_2}\left(\dfrac{q_1 q_2 + \frac{1}{2}q_2^2}{r_2}\right), \end{cases} \tag{17}$$

from which one immediately obtains

$$\begin{cases} \dfrac{p_1^2}{2m_1} + \dfrac{\frac{1}{2}q_1^2}{r_1} = \mathrm{Const}, \\ \dfrac{p_2^2}{2m_2} + \dfrac{q_1 q_2 + \frac{1}{2}q_2^2}{r_2} = \mathrm{Const}. \end{cases} \tag{18}$$

As the two shells continue to expand, the asymptotic kinetic energy for $t \to +\infty$, $\mathcal{E}(+\infty)$, of the two shells can be readily evaluated, as

$$\begin{cases} \mathcal{E}_1(+\infty) = \mathcal{E}_1(0) + \dfrac{\frac{1}{2}q_1^2}{r_1(0)}, \\ \mathcal{E}_2(+\infty) = \mathcal{E}_2(0) + \dfrac{q_1 q_2 + \frac{1}{2}q_2^2}{r_2(0)}. \end{cases} \tag{19}$$

Now, the case of collision is considered. When $t = t_c$ one has $r_1(t_c) = r_2(t_c) = r_c$, and for $t > t_c$ the shell #1 overtakes the shell #2. Therefore, Eqs. (16-18) are valid only for $t < t_c$. For $t > t_c$, Eqs. (16) must be replaced by

$$\begin{cases} \dfrac{\mathrm{d}p_1}{\mathrm{d}t} = q_1 \dfrac{q_2 + \frac{1}{2}q_1}{r_1^2}, \\ \dfrac{\mathrm{d}p_2}{\mathrm{d}t} = q_2 \dfrac{\frac{1}{2}q_2}{r_2^2} \end{cases} \tag{20}$$

(they are obtained by simply exchanging indices 1 and 2), from which one finally obtains

$$\begin{cases} \dfrac{p_1^2}{2m_1} + \dfrac{q_1 q_2 + \frac{1}{2}q_1^2}{r_1} = \mathrm{Const}, \\ \dfrac{p_2^2}{2m_2} + \dfrac{\frac{1}{2}q_2^2}{r_2} = \mathrm{Const}. \end{cases} \tag{21}$$

127

In the case of collision, in order to evaluate the new asymptotic energy, $\mathcal{E}'(+\infty)$, both Eqs. 18 (for $t < t_c$) and Eqs. 21 must be considered:

$$\begin{cases} \mathcal{E}'_1(t_c) = \mathcal{E}_1(0) + \dfrac{\frac{1}{2}q_1^2}{r_1} - \dfrac{\frac{1}{2}q_1^2}{r_c} = \mathcal{E}_1(+\infty) - \dfrac{\frac{1}{2}q_1^2}{r_c}, \\[4mm] \mathcal{E}'_2(t_c) = \mathcal{E}_2(0) + \dfrac{q_1 q_2 + \frac{1}{2}q_2^2}{r_2} - \dfrac{q_1 q_2 + \frac{1}{2}q_2^2}{r_c} = \mathcal{E}_2(+\infty) - \dfrac{q_1 q_2 + \frac{1}{2}q_2^2}{r_c}, \end{cases} \quad (22)$$

and

$$\begin{cases} \mathcal{E}'_1(+\infty) = \mathcal{E}'_1(t_c) + \dfrac{q_1 q_2 + \frac{1}{2}q_1^2}{r_c} = \mathcal{E}_1(+\infty) + \dfrac{q_1 q_2}{r_c}, \\[4mm] \mathcal{E}'_2(+\infty) = \mathcal{E}'_2(t_c) + \dfrac{\frac{1}{2}q_2^2}{r_c} = \mathcal{E}_2(+\infty) - \dfrac{q_1 q_2}{r_c}. \end{cases} \quad (23)$$

In other terms, the collision produces an increase $\Delta\mathcal{E} = q_1 q_2 / r_c$ in the energy of the shell #1, and a corresponding decrease $-\Delta\mathcal{E}$ for the shell #2. In a typical plasma expansion, the energy $\mathcal{E}$ of a shell is of the order of qQ/R, being Q the total charge and R the initial plasma radius. Being $\Delta\mathcal{E} \sim q^2/R$ for a single collision, one can conclude that the "plasma parameter" $\Delta\mathcal{E}/\mathcal{E}$ for a set on N shells will be of the order of $q/Q = 1/N$. In practice, for typical values of the number of computational particles, the system can always be regarded as collisionless.

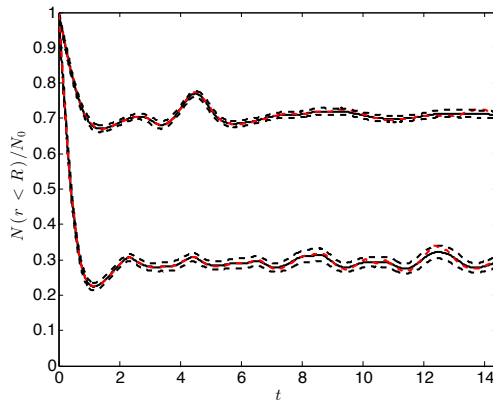
Figure 1: Time evolution of the fraction of electrons inside the ion sphere for two different normalized temperature, $T = 0.0431, 0.431$. For each value of T, ensemble averages (full black line) and standard deviation ranges (dashed black lines) are reported for $N = 10^3$ shells and 300 simulations with different initial conditions, together with reference results provided by a simulation with $N = 10^6$ shells (dashed red line).
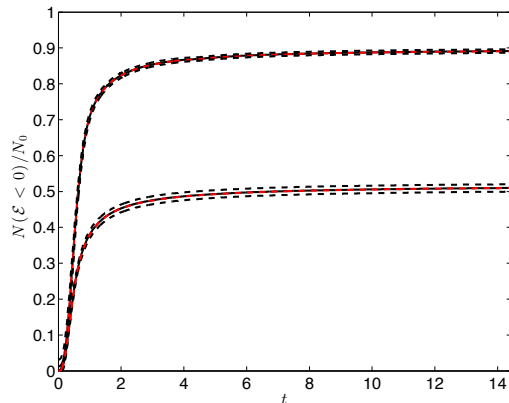
Figure 2: Time evolution of the fraction of trapped electrons for the same case of Fig. 1.

2.5 Results

Some typical results are reported in the following. In all the calculations, suitable normalization for the physical quantities has been used such that the total charge, the total mass of the plasma and the initial radius R are all equal to 1. Three cases are considered: 1) the electron expansion in a spherical plasma [4]; 2) the expansion of a plasma made of a mixture of two ion species [5]; 3) the formation of shocks in Coulomb explosions [6]. Figures 1 and 2 refer to the early stage of the electron expansion in a spherical plasma. It is assumed that electrons and positive ions are initially distributed uniformly in a sphere of radius R. Initially, electrons have Maxwellian velocity distribution with temperature T and positive ions are considered at rest during all the transient. Calculations have been performed both with a reduced ($N \simeq 10^3$) and with a high number of shells ($N \simeq 10^6$), in order to obtain reference results. The initial phase-space distribution of the electrons was generated by using random numbers, so for a small number of particles the results will depend on the particular choice of positions and velocities. For this reason, the same calculation has been repeated for 300 times (with different initial conditions, all corresponding to the same physical situation) in order to obtain the mean behavior and the distribution of the physical quantities (as performed in [7]). In Figs. 1 and 2, the time evolution of the number of electrons inside the ion sphere (i.e., with $r \leq R$) and of the fraction of trapped electrons (i.e., with total energy $\frac{p^2}{2m} - e\Phi(r) \leq 0$) are reported, respectively. As can be observed, the shell method provides excellent results, even with a reduced set of particles.

The second set of results (Figs. 3 and 4) refers to the acceleration of an
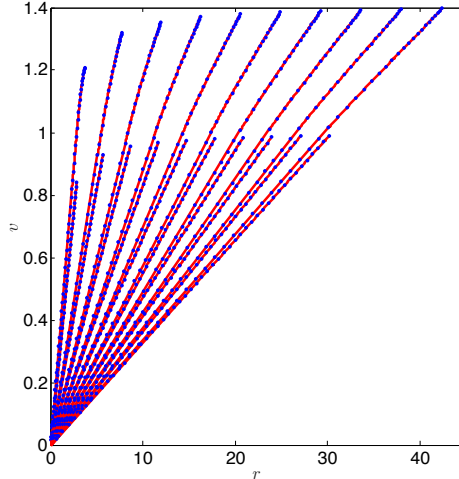
129

Figure 3: Phase-space distributions of a mixture with $m_1/m_2 = 2/3$ and $q_1 = q_2$ at different times ($t = 3 \div 31$). Results obtained with the shell method (blue dots) are compared with the analytic solution (red solid lines).

ion plasma made of a mixture of two different species. In this case, analytic solutions for the problem exist [5] and can be used as a reference. The two species ($m_1/m_2 = 2/3, q_1 = q_2$) are initially at rest and the ions are accelerated by electrostatic repulsion. In Fig. 3 the phase-space distribution for the two species, calculated with the shell method and using 10^3 computational particles, is reported at different times and compared with analytic results. Figure 4 shows $\mathcal{E}(t \to +\infty)/m$ of the light ions as a function of their initial radial coordinate, $r = r_0$. This curve is important in order to determine the asymptotic energy spectrum, $\frac{\mathrm{d}N}{\mathrm{d}\mathcal{E}}$, of the ions (considering that $\Delta\mathcal{E} = \frac{\mathrm{d}\mathcal{E}}{\mathrm{d}r_0}\Delta r_0$ and $\Delta N = 4\pi r_0^2 n_0 \Delta r_0$). The two figures show the excellent agreement between numerical and analytic results.

The third case here considered concerns the shock formation in a Coulomb explosion [4, 8]. The phenomenon arises when the initial ion distribution is not uniform, in particular if the inner density is larger respect to the outer one. In fact, in this case the electric field has a maximum inside the plasma region (while it depends linearly on r if the ion density is constant) and consequently inner particles acquire higher kinetic energy with respect to the outer ones and can "overtake" them. In the situation considered in Figs. 5 and 6, an ion plasma made of only one species presents two regions with different density for $t = 0$. Figure 5 reports the value of the radial coordinate $r(r_0, t)$ of the ions as a function of their initial radius, r_0, for different times, while in Fig. 6 the phase-space
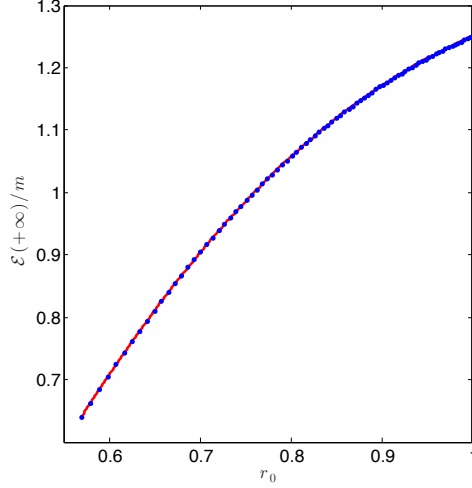
130

Figure 4: $\mathcal{E}(t \to +\infty)/m$ of the light ions as a function of their initial radial coordinate, r_0, for the case of Fig. 3. Results obtained with the shell method (blue dots) are compared with the analytic solution (red line).

distribution is plotted. The results here reported show the ability of the shell method to analyze cases in which the density, in theory, may become infinite in some point; in fact, results obtained with a relative low (10^4) and with a very large (10^6) number of shells are in perfect agreement.

3   The ring method

In the case of axial symmetry the fundamental "brick" for a N-body technique is a ring. More precisely, tori having circular cross section (of radius a) are considered here. The tori shares the same axis of symmetry (the z axis) and are characterized by their radii, R_i, and axial coordinates, z_i (as in Fig. 7). When N tori are considered, the electrostatic energy of the system can be written as:

$$U = \frac{1}{2} \sum_{i \neq j} q_i q_j \varphi_{ring}(R_i, R_j, z_i - z_j) + \sum_{i=1}^{N} q_i^2 U_{torus}(R_i, a), \qquad (24)$$

where $\varphi_{ring}(R, R', z')$ is the potential generated by a unit charge distributed on a ring (i.e., a torus with $a = 0$) of radius R laying on the xy plane in a point of polar coordinates (R', z'), while $U_{torus}(R, a)$ is the potential energy of a torus
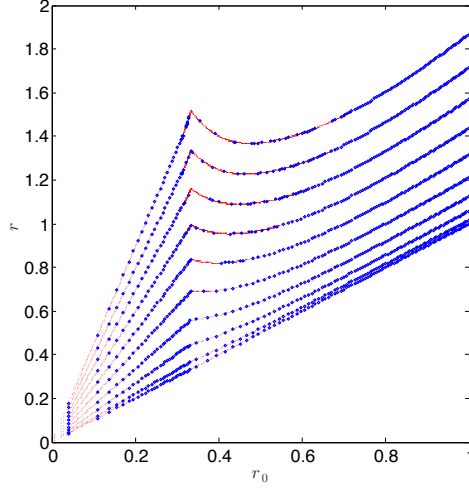
Figure 5: Radial coordinate, r, at different times ($t = 0 \div 1.47$) as a function of their initial position, r_0, for a single-species ion plasma with a non uniform initial density distribution. In the simulations, $n(r,0) = n_1$ when $r < R/3$ and n_2 when $r \in \left[\frac{R}{3}, R\right]$, with $n_1/n_2 = 8$. Results for 10^4 shells (blue dots) are compared with those obtained with 10^6 shells (red line).

of unitary charge. The potential $\varphi_{ring}(R; R', z')$ can be evaluated[1] in terms of the complete elliptic integral of the first kind [9]:

$$K[x] = \int_0^{\pi/2} \frac{\mathrm{d}\,\alpha}{(1 - x\sin^2\alpha)^{1/2}},\tag{27}$$

as

$$\varphi_{ring}(R; R', z') = \frac{2K[\xi]}{\pi s},\tag{28}$$

---

[1]As a generic point of the ring has coordinates $(R\cos(\vartheta), R\sin(\vartheta), 0)$ and the point where the potential has to be evaluated has coordinates $(R', 0, z')$, the potential φ_{ring} can be written as

$$\varphi_{ring} = \frac{1}{2\pi} \int_0^{2\pi} \frac{1}{(R^2 + R'^2 + z'^2 - 2RR'\cos\theta)^{1/2}}\,\mathrm{d}\,\theta,\tag{25}$$

By introducing the new integration variable $\alpha = \frac{\theta}{2} - \frac{\pi}{2}$, the formula for φ_{ring} becomes:

$$\varphi_{ring} = \frac{2q}{\pi} \int_0^{\pi/2} \frac{1}{\left[(R + R')^2 + z'^2 - 4RR'\sin^2\alpha\right]^{1/2}}\,\mathrm{d}\,\alpha,\tag{26}$$
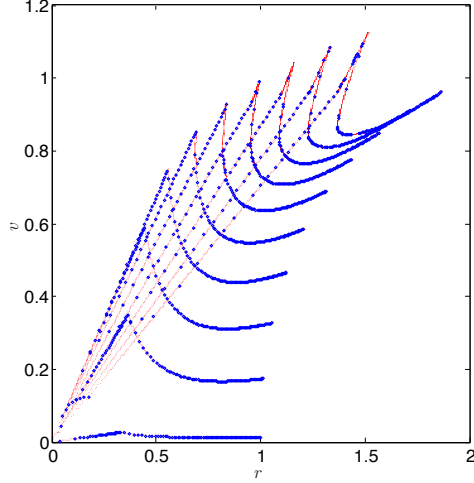
from which Eq. (28) immediately follows.

132

Figure 6: Ion phase-space distribution at different times ($t = 0 \div 1.47$) for the same case of Fig. 5. Results for 10^4 shells (blue dots) are compared with those obtained with 10^6 shells (red line).

being

$$s = [(R + R')^2 + z'^2]^{1/2}, \quad \xi = \frac{4RR'}{s^2}. \tag{29}$$

The calculation of $U_{torus}(R, a)$ is reported in detail in the Appendix. For the case of interest in which $a \ll R$, one has:

$$U_{torus}(R, a) \sim -\frac{1}{2\pi R} \left[\log\left(\frac{a}{8R}\right) - \frac{1}{4} \right]. \tag{30}$$

From Eq. (30), it can be noticed that U_{torus} diverges for $a \to 0$, and this is the reason why tori are considered and not simply rings. Instead, in calculating the interaction energy between tori, the value of φ_{ring} is employed, as it is supposed that when $a \ll R$ the energy of two tori or two rings is essentially the same. Now, the equations of the motion for the set of rings are derived. In order to write the Lagrangian of the system, the kinetic energy

$$\sum_{i=1}^{N} \frac{m_i}{2} \left(\dot{R}_i^2 + \dot{z}_i^2 + R_i^2 \dot{\varphi}_i^2 \right) \tag{31}$$

must be considered. By introducing the momenta $p_{R,i}$, $p_{z,i}$, and $p_{\varphi,i}$:

$$p_{R,i} = m_i \dot{R}_i, \qquad p_{z,i} = m_i \dot{z}_i, \qquad p_{\varphi,i} = m_i R_i^2 \dot{\varphi}_i, \tag{32}$$
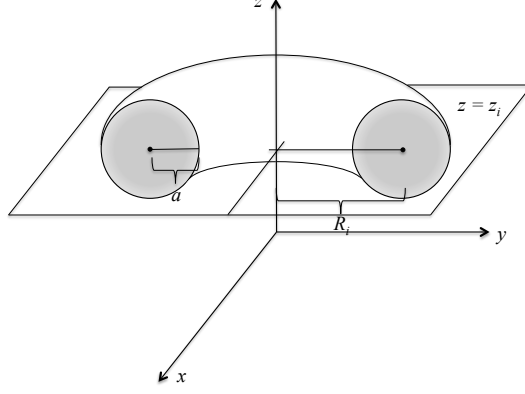
133

Figure 7: Scheme of a torus.

one finally obtains the Hamiltonian $\mathscr{H}$ of the N interacting rings as:

$$\mathscr{H} = \sum_{i=1}^{N} \frac{1}{2m_i}\left(p_{R,i}^2 + p_{z,i}^2 + \frac{p_{\varphi,i}^2}{R_i^2}\right) + \frac{1}{2}\sum_{i\neq j} q_i q_j \varphi_{ring}(R_i, R_j, z_i - z_j) + \sum_{i=1}^{N} q_i^2 U_{torus}(R_i, a),$$

(33)

and the equations of the motion:

$$\begin{cases} \dfrac{\mathrm{d}\,R_\alpha}{\mathrm{d}\,t} = \dfrac{p_{R,\alpha}}{m_\alpha}, \qquad \dfrac{\mathrm{d}\,z_\alpha}{\mathrm{d}\,t} = \dfrac{p_{z,\alpha}}{m_\alpha}, \\[3mm] \dfrac{\mathrm{d}\,p_{R,\alpha}}{\mathrm{d}\,t} = \dfrac{p_{\varphi,\alpha}^2}{m_\alpha R_\alpha^3} - \sum_{\beta\neq\alpha} q_\alpha q_\beta \dfrac{\partial}{\partial R_\alpha}\varphi_{ring}(R_\alpha, R_\beta, z_\alpha - z_\beta) - q_\alpha^2 \dfrac{\partial}{\partial R_\alpha} U_{torus}(R_\alpha; a), \\[3mm] \dfrac{\mathrm{d}\,p_{z,\alpha}}{\mathrm{d}\,t} = -\sum_{\beta\neq\alpha} q_\alpha q_\beta \dfrac{\partial}{\partial z_\alpha}\varphi_{ring}(R_\alpha, R_\beta, z_\alpha - z_\beta). \end{cases}$$

(34)

The angular momenta $p_{\varphi,\alpha}$ are constants of the motion. The partial derivatives of φ_{ring} can be readily evaluated considering that:

$$\frac{\mathrm{d}\,K[x]}{\mathrm{d}\,x} = \frac{E[x] - (1-x)K[x]}{2x(1-x)},$$

(35)

being $E[x] = \int_0^{\pi/2}(1 - x\sin^2\alpha)^{1/2}\mathrm{d}\alpha$ the complete elliptic integral of the second kind [9]. Equations (34) have been deduced by considering only electrostatic interaction in non relativistic limit. In principle, the method can be readily extended to include relativistic particles and magnetic field (with axial symmetry). To test its accuracy, the ring method has been employed to simulate the
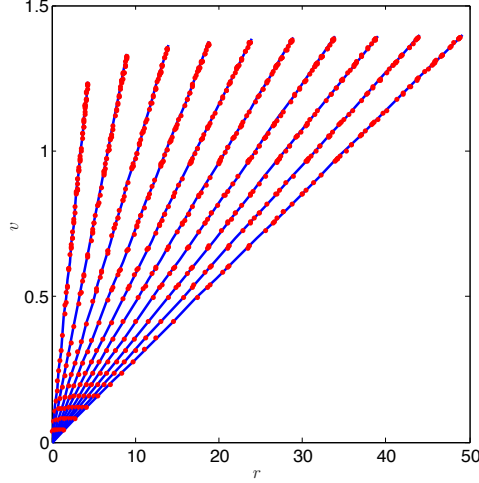
Figure 8: Phase-space distribution at different times ($t = 4 \div 36$) of a spherical ion plasma in the case of ring loading with method 1. Results obtained with the ring method (blue dots) are compared with the analytic solution (red lines).

expansion of an ion sphere of uniform density, for which a simple analytic solution exists. The same normalizaion of the physical quantities of Sect. 2.5 is used here. The initial ring distribution $\{R_i, z_i\}$ has been generated in two different ways: 1) by dividing the initial $[R, z]$ domain (i.e., a half circle of radius R_0) into a number N of small squares, each corresponding to the cross section of a ring; 2) by suitably taking a set of $\{R_i, z_i\}$ in a random way in order to obtain a uniform charge density. The radius a_i of the section of each ring has been chosen as proportional to R_i, i.e., $a_i = k \cdot R_i$. The constant k has been determined by requiring the potential energy of the set of the rings to be equal to the exact value of the energy of the sphere. Figures 8, 9 and 10, 11 refer to method 1 and method 2, for ring loading, respectively. In Figs. 8 and 9 the time evolution of the phase-space distribution, as obtained with the ring method, is shown and it is compared with its analytical behavior. Figures 10 and 11 show the total kinetic energy of the ions, $\mathcal{E} = \sum_{i=1}^{N} \frac{m_i}{2} \mathbf{v}_i^2(t)$, as a function of t; moreover, the behavior of $[\mathcal{E}^{(t)} - \mathcal{E}_r(t)]/\mathcal{E}$, where $\mathcal{E}_r(t) = \sum_{i=1}^{N} \frac{m_i}{2} \left[\mathbf{v}_i^2(t) \cdot \mathbf{e}_{r,i}(t) \right]$ is the kinetic energy due to the motion in radial direction, is also presented. Obviously, in the exact solution $\mathcal{E}_r(t) \equiv \mathcal{E}(t)$, so a value of $\left| \frac{\mathcal{E} - \mathcal{E}_r(t)}{\mathcal{E}} \right| \ll 1$ is expected. All the numerical results presented in Figs. 8, 9, 10, 11 are in excellent agreement with the theory.

The second group of results here presented concerns the Coulomb explosion of an ion plasma having initially a cylindrical form. These are cases of practical
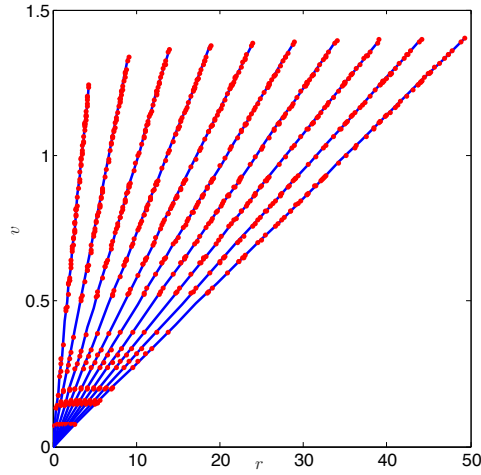
Figure 9: Same as Fig. 8 in the case of ring loading with method 2 ($t = 4 \div 36$). Results obtained with the ring method (blue dots) are compared with the analytic solutions (red lines).
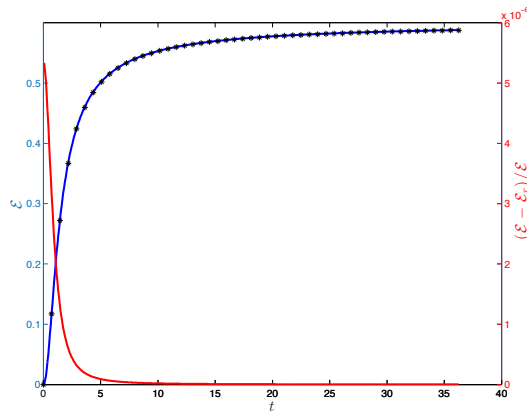

Figure 10: Time evolution of the total kinetic energy of the ions (blue line) and of the fraction of the perpendicular kinetic energy (red line) obtained with the ring method for the same case of Fig. 8 (method 1 for ring loading). Results obtained with the ring method are compared with the analytic solutions (black stars).
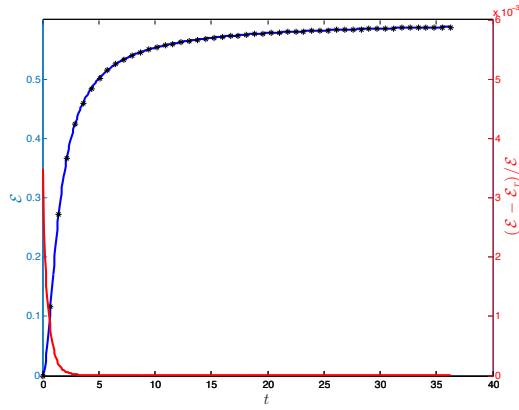
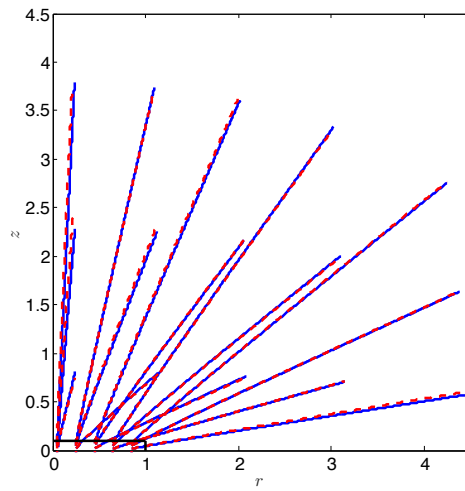Figure 11: Same as Fig. 10, using method 2 for ring loading.

Figure 12: Particle trajectories for the Coulomb explosion of an ion plasma having initially a cylindrical shape (the ratio between initial radius R and height H is equal to 0.1) for $t = 0 \div 4$. Results obtained with the ring method (blue lines) are compared with those obtained with the PIC method (red dotted lines).
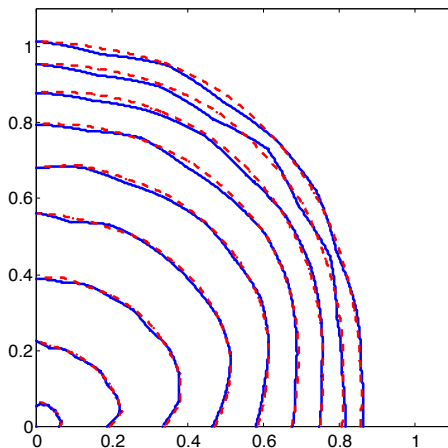
137

Figure 13: Angular distribution of $\mathcal{E}/m$ for the case of Fig. 12 for $t = 0 \div 4$. Results obtained with the ring method (blue lines) are compared with those obtained with the PIC method (red dotted lines).

interest, as they simulate the ion acceleration of the positive ions of a thin solid target after interaction with a ultra intense laser pulse. Two cases are considered, in which the cylinder has different aspect ratio. Figures 12 and 13 show the trajectories of the ions and the angular distribution of the kinetic energies for the first case. The same physical quantities are presented in Figs. 14 and 15 for the second case. In the Figures, the results of the ring method are compared with those obtained by using a PIC code developed by the Authors [2]. The agreement between the two techniques is excellent.

4   Final considerations

The results presented in the paper and all the tests that have been performed prove the effectiveness of the numerical technique here proposed. The interaction between computational particles is not mediated by a grid and, as shown in Sects. 2 and 3, the method can be deduced by using a Hamiltonian approach. Consequently, all the physical quantities of interest (e.g., momentum, energy and angular momentum) are conserved exactly by the method, and the only

---

[2]The code makes use of an (R, z) uniform grid that is expanding in order to follow the motion of the particles. Moreover, the electrostatic potential is calculated at the border of the computational domain by summing the contributions due to all the rings; in this way, "exact" boundary conditions are provided for the solver of the Poisson's equation.
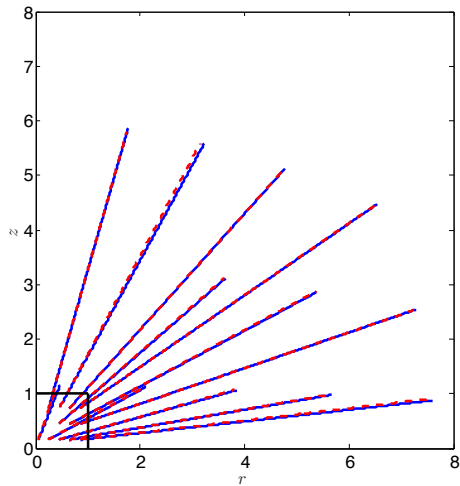
Figure 14: Same as Fig. 12, but for a cylinder with $H/R = 1$ for $t = 0 \div 10$. Results obtained with the ring method (blue lines) are compared with those obtained with the PIC method (red dotted lines).
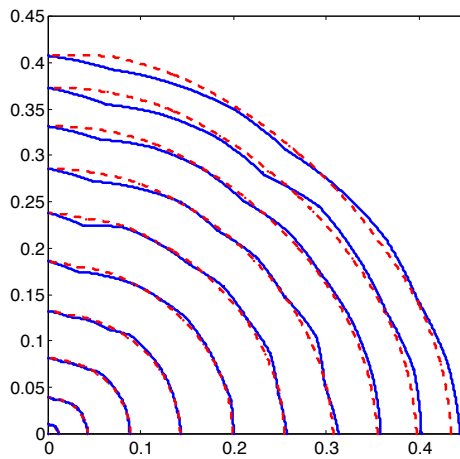

Figure 15: Same as Fig. 13, but for a cylinder with $H/R = 1$ for $t = 0 \div 10$.

139

errors are due to time discretization. This properly represents an important feature of the method. When the problem has the required degree of symmetry, the methods of shells and of rings can be usefully employed in two cases: 1) to obtain results making use of a simple, easy-to-implement code; 2) to have reference results to test more complex codes, in particular when the physical region occupied by the plasma grows dramatically during the simulation. For these reasons, in the Authors' opinion the method can be regarded as a useful tool, in particular in the study of laser-plasma interaction.

A   Electrostatic energy of a torus with $a \ll R$

With reference to Figure 16, the electrostatic energy of a torus can be calculated by dividing the cross section S in a large number of subdomains. Each of them generates an electrostatic potential that can be approximated as the one of a ring. Indicating by Δq_i the charge of the i-th subdomain and by $\varphi_{ring}(\mathbf{x}_i; \mathbf{x}_j)$ the potential in $\mathbf{x}_i$ due to a unitary charge in $\mathbf{x}_j$, the energy of the torus can be approximated by
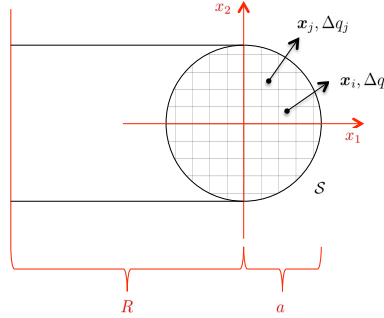
Figure 16: Cross section of a torus and coordinates employed in the calculation.

$$U \simeq \frac{1}{2} \sum_{i \neq j} \Delta q_i \Delta q_j \varphi_{ring}(\mathbf{x}_i, \mathbf{x}_j). \tag{36}$$

In the limit when the size of the subdomains tends to zero, one obtains

$$U = \int_{\mathscr{S}} \mathrm{d}^2 x_Q \int_{\mathscr{S}} \mathrm{d}^2 x_P \sigma(\mathbf{x}_Q) \sigma(\mathbf{x}_P) \varphi_{ring}(\mathbf{x}_P, \mathbf{x}_Q), \tag{37}$$

where $\sigma(\mathbf{x})$ is the charge density for a unit cross section. If the torus is uniformly charged and if $a \ll R$, one can assume

$$\sigma \simeq \frac{q}{\pi a^2} = \text{Const.} \tag{38}$$

140

In order to evaluate $\varphi_{ring}(\mathbf{x}_P, \mathbf{x}_Q)$, the parameters s and ξ, defined in Eq. (29), must be evaluated. One has:

$$\xi = \frac{4(R + x_{1,P})(R + x_{1,Q})}{s^2}, \qquad s = \left[(R + x_{1,P} + R + x_{1,Q})^2 + (x_{2,P} - x_{2,Q})^2\right]^{1/2}. \tag{39}$$

It turns out useful to introduce the quantity $\eta = R + \frac{x_{1,P} + x_{1,Q}}{2}$, such that $R + x_{1,P} = \eta + \frac{x_{1,P} - x_{1,Q}}{2}$, $R + x_{1,Q} = \eta - \frac{x_{1,P} - x_{1,Q}}{2}$. In this way, ξ can be written as:

$$\xi = \frac{1 - \left(\frac{x_{1,P} - x_{1,Q}}{2\eta}\right)^2}{1 + \left(\frac{x_{2,P} - x_{2,Q}}{2\eta}\right)^2} \simeq 1 - \left(\frac{r_{PQ}}{2R}\right)^2, \tag{40}$$

with $r_{PQ}^2 = (\mathbf{x}_P - \mathbf{x}_Q)^2$. In fact, η is much larger with respect to $|x_{2,P} - x_{2,Q}| \leq a$, so the approximation $\frac{1}{1+\epsilon} \simeq 1 - \epsilon$ can be used; moreover, η can be approximated by R. Making use of the asymptotic behavior of $K[\xi]$ for $\xi \to 1$:

$$K[\xi] \underset{\xi \to 1}{\sim} -\frac{1}{2} \log(1 - \xi) + \log 4, \tag{41}$$

and assuming that $s \simeq 2R$, the following expression for $\varphi_{ring}(\mathbf{x}_P, \mathbf{x}_Q)$ is obtained:

$$\varphi_{ring}(\mathbf{x}_P, \mathbf{x}_Q) = -\frac{1}{\pi R} \log\left(\frac{r_{PQ}}{8R}\right). \tag{42}$$

Equation (42) can be employed in Eq. (36), which can be rewritten as

$$U = \frac{\sigma^2}{2} \int_{\mathscr{S}} \mathrm{d}^2 x_Q \varphi_{torus}(\mathbf{x}_Q), \tag{43}$$

being

$$\varphi_{torus}(\mathbf{x}_Q) = -\frac{1}{\pi R} \int_{\mathscr{S}} \mathrm{d}^2 x_P \log\left(\frac{r_{PQ}}{8R}\right). \tag{44}$$

For $\mathbf{x}_Q = 0$, φ_{torus} is readily evaluated:

$$\varphi_{torus}(0) = -\frac{1}{\pi R} \int_0^a 2\pi r \, dr \log\left(\frac{r}{8R}\right) = -\frac{a^2}{R}\left[\log\left(\frac{a}{8R}\right) - \frac{1}{2}\right]. \tag{45}$$

To calculate φ_{torus} for a generic $\mathbf{x}_Q \in S$, one can start by noticing that $\log(r_{PQ})$ is proportional to the Green function for the two-dimensional Poisson's equation:

$$\nabla_Q^2 \log r_{PQ} = 2\pi \delta\left(\mathbf{x}_Q - \mathbf{x}_P\right). \tag{46}$$

So, by applying the Laplacian operator ∇_Q^2 to Eq. (44), one obtains

$$\nabla_Q^2 \varphi_{torus} = -\frac{1}{\pi R} \int_S \mathrm{d}^2 x_P \cdot 2\pi \delta\left(\mathbf{x}_P - \mathbf{x}_Q\right) = -\frac{2}{R}. \tag{47}$$

141

Due to the symmetry of the problem, φ_{torus} is a function of $r_Q = |\mathbf{x}_Q|$, and the Laplacian operator can be written as $\nabla_Q^2 = \frac{1}{r_Q}\frac{\mathrm{d}}{\mathrm{d}\,r_Q}r_Q\frac{\mathrm{d}}{\mathrm{d}\,r_Q}$. Therefore, Eq. (47) can be immediately solved, so obtaining

$$\varphi_{torus}(\mathbf{r}_Q) = \varphi_{torus}(0) - \frac{r_Q^2}{2R}. \tag{48}$$

Finally, the energy of the torus can be calculated by using Eq. (43):

$$U = \frac{q^2}{2\pi^2 a^4} \cdot 2\pi \int_0^a r_Q \mathrm{d}r_Q \left[\varphi_{torus}(0) - \frac{r_Q^2}{2R}\right] = -\frac{q^2}{2\pi R}\left[\log\left(\frac{a}{8R}\right) - \frac{1}{4}\right]. \tag{49}$$

Formula (49) is very accurate for $a \ll R$. If compared with the value of U obtained from numerical integration of Eq. (36), the relative error is less than 0.5% for $a/R < 0.2$. A similar formula (without the term -1/4) has been deduced in a concise, brilliant way in [10] by using the technique of asymptotic matching.

Lesion dosimetry in metastatic thyroid cancer treated with [131]I: standardization of SPECT-TC calculation method with an in-house software tool

Introduction

The treatment of metastatic thyroid cancer with high ^{131}I activity is a safe and effective therapeutic option when a radioiodine uptake into lesions is present. To maximize the efficacy of the administration, one high ^{131}I activity treatment is preferable, while repeated lower activity treatments seem to be less effective due to the decreasing lesions uptake as reported by Lee [4]. The ^{131}I therapy employing ionizing radiation is analog to any external beam radiation therapy. For this reason, the calculation of the dose to the target (remnant thyroid or metastasis) and the organ at risk (red marrow, salivary glands, lungs) should be mandatory as reported by the national (D.Lgs 187/2000) and European (EU Directive 59/2013) regulations. Particularly, when high activities are administered to the patients, the dose estimation becomes relevant. A first dosimetric goal is to avoid severe patient's toxicity delivering less than 2 Gy to red marrow as reported by literature data [5, 6]. The correlation between dose to metastasis and clinical response is indicated by Maxon and Dorn [7,8],+ but the efficacy of a dosimetric approach compared to the fixed activity one is still under debate [9, 10]. The best effective dose to be delivered to the target in advanced metastatic patients (80-100 Gy to lymphnodes lesions and more than 300-400 Gy to bone metastasis [11]) as well as salivary gland dose limits should be confirmed by extensive clinical trials [12]. This could be achieved only when lesion dosimetry will be performed in most nuclear medicine therapeutic departments, increasing the number of patients' dataset. The advanced metastatic patients are rare and represent a minority compared to all thyroid patients treated with radioiodine. To perform ^{131}I lesion dosimetry, some post administration emissive acquisitions (planar or tomographic) are necessary to estimate the radiopharmaceutical biodistribution in each lesion that must be converted in dose using a specific calibration. This can represent an issue (radiation exposure of the nuclear medicine personal staff, time to perform the calibration and patient's acquisitions) and many centres were discouraged from following this dosimetric approach, encouraged by the belief that the metastatic thyroid patients have a prolonged survival generally. This is true for most of the patients, but a percentage of them have a poor prognosis, however. The available commercial nuclear medicine dosimetric software supply the dose calculation for many radionuclides (i.e. [90]Y or ^{177}Lu), but no one is available for the [131]I. The recent improvement of the SPECT-TC technology has made possible the direct quantification of the activity into the lesions also for this type of radioisotope simplifying the activity-curve analysis, but the co-registration of the different acquisitions, the

volumes contouring and the conversion from integrated activity to dose remain an issue. The mathematical model is clear and shared in the scientific community, but the standardization in the practical aspects of the ^{131}I dose calculation is needed as suggested by the Internal dosimetry group of the Italian Association of Medical Physics (AIFM) [11]. The aim of this study is to verify the robustness of an in-house dosimetry software tool created at Mauriziano Hospital of Turin to calculate the dose to the lesion of metastatic thyroid patients treated with high ^{131}I activity. The standard dose calculation method is compared to the automated software one both on phantom and patient acquisitions to check the accuracy in term of cumulated activity and dose.

Materials and methods

^{131}I lesion dosimetry with SPECT-TC technique

To calculate the dose at first, the ^{131}I activity must be estimated into the lesion.

Absolute calibration. The lesion is defined by drawing a Volume of Interest (VOI) that enclose the whole metastasis. The counts into the VOI are converted to MBq applying an absolute calibration factor CF [MBq/counts]. This CF factor is obtained by acquiring a SPECT-TC uniform phantom filled with known liquid ^{131}I activity. The total counts into the phantom are divided by the total activity (MBq), and this ratio represents the CF. The volume of the uniform phantom must be larger enough to avoid partial volume effects and without dead time count loss effects.

Partial Volume Effects. The partial volume effect (PVE) is a well-known effect in the SPECT-TC acquisition technique that consists of a loss of counts when small volumes are acquired. To correct the PVE a recovery coefficient curve must be calculated to correlate the volume with the percentage of count loss. To this aim, a phantom with spheres of different volumes can be employed. The spheres are filled with a known liquid ^{131}I activity, A_{true}. The counts in each sphere are converted with the absolute K factor into activity, $A_{measured}$. The measured value is compared to the true expected activity value A_{true}. The PVE correction factor is calculated as the ratio between $A_{measured}$ and A_{true} : PVE $= A_{measured}/A_{true}$. The PVE factor is calculated for each sphere. The smaller is the volume the nearest to zero is the PVE coefficient. For larger volumes the effect becomes negligible and the PVE factor is equal to 1. A curve (PVE versus volume) is plotted and fitted with the equation $f(PVE) = a + b \exp(c\ volume)$ to obtain the function PVE-volume. When a lesion is evaluated, the volume of the lesion is set into the function f (PVE) and the relative PVE factor is obtained.

Dead time correction. In the patient's body, the amount of ^{131}I activity after the therapeutic administration can consist in a high quantity of MBq, especially in the first days, because the radioiodine is cumulated not only into the metastasis but also in the organs at risk (i.e. bladder, stomach, salivary glands). For this reason, when an early SPECT-TC acquisition is performed the quantity of ^{131}I activity can be so high to produce a count loss due to dead time events. The SPECT-TC detector receives too many photons and is not able to count it all. This phenomenon is higher in the first acquisition and becomes lower and then negligible if the SPEC-TC acquisition is performed in the following days after the therapy. A dead time correction factor is needed to take into account the dead time correction. To this aim, the uniform phantom was filled with a high ^{131}I liquid activity to present dead time condition. Several SPECT-TC acquisitions were acquired and the dead time index DT supplied by the gamma camera equipment was noticed for every acquisition. In the last day of acquisition, the dead time was negligible and the counts in the volume of the uniform phantom can be considered as true, without loss due to dead time effect. The counts measured in each acquisition were than related to the true counts expected, at a determined acquisition time, without dead time effect. The dead time correction factor K_{DT} was also obtained as K_{DT} = counts$_{measured}$ / counts$_{true}$. This factor, calculated for each SPECT-TC acquisition, was then related to the empirical DT factor that is available during the SPECT-TC on the workstation acquisition. A relationship between K_{DT} and DT was fount: $K_{DT} = a \cdot DT^2 + b$. When a patient SPECT-TC is acquired the DT value is noticed (the mean value among all the views is considered) and trough the polynomial relationship the corresponding K_{DT} factor is obtained.

Considering all the above mentioned converting and correction factors the activity in the VOI is obtained with the formula:

$$Activity = cts_{ROI} \cdot \frac{K_{DT}}{PVE\ RC} \cdot CF \quad [1]$$

Activity - Time curve The activity into the lesion is calculated for each of the 4 SPECT-TC (at 4, 24, 48, 96 h) acquired after the therapeutic ^{131}I administration. The activity [MBq] is plotted as a function of the time [h] to obtain the Activity-Time curve. The curve fitting with a bi-exponential function Activity [MBq] = A*(EXP(B*time(h))-EXP(C*time(h))) is integrated [0, ∞] to calculate the area under the curve (undefined integral = A/B-A/C) that corresponds to the cumulated activity, $\tilde{A}$ [MBq · h], in the lesion.

Lesion mass The lesion mass [g] is calculated from the lesion volume V [cc] and the lesion density [g/c^3]   Lesion mass [g] = lesion volume [cm^3] x density [g/cm^3].

The lesion density (g/c^3) was obtained from the Hounsfield Unit HU in the VOI converted to density [g/cm^3]. The SPECT-TC was calibrated with a HU-density curve.

Lesion Mean Dose The mean dose to the lesion is finally calculated with the MIRD sphere model [xx] with the formula

$$\text{Dose [mGy]} = S \text{ [mGy/MBq h]} \times \tilde{A} \text{ [MBq} \cdot \text{h]}. \qquad [2]$$

The S factors are tabulated in the OLINDA/EXM Model. A fit to obtain the correct S factor corresponding to the lesion mass was employed:

S (mGy/MBq h) = 110.02 / m$^{0.9734}$ for lesion mass < 10 g

S (mGy/MBq h) = 107.8 / m$^{0.9673}$ for lesion mass 10 g < m < 100 g

S (mGy/MBq h) = 97.1 / m$^{0.944}$ for lesion mass > 100 g.

SPECT-TC calibration with ^{131}I phantom measurements

To obtain the absolute calibration factor K, the partial volume effects correction factors PVE and dead time correction factors $K_{DT,}$ a NEMA PET-CT sphere phantom was used. The spheres (10.7cc, 5.44cc and 1.2cc) placed in the upper part and the cylinder (130 cc) positioned in the lower part are were filled with liquid ^{131} I with a well-known activity (initial ^{131}I concentration 13.7 MBq/ml). The surrounding volume was filled with not radioactive water. As reported in Figure 1, there is no overlapping between the volume of the cylinder and the volume of the spheres that are positioned in separate z-plane.

Figure 1 NEMA PET-TC phantom

A SPECT-TC (Siemens Intevo T2) acquisition of the NEMA PET-TC phantom was performed (HEHR collimators, 256x256 matrix, voxel size 4.8 mm, 64 views, 20 s/views, circular orbit Radius = 25 cm, 28 cm, 33 cm); images were corrected by scattering and CT-attenuation, then reconstructed with an Iterative Algorithm (RR, Flash3D). The acquisition was repeated 9 times, immediately after the phantom preparation and in the following days [0 ÷ 40 days]. Dead time DT values were noticed for each acquisition and reported in Table 1 where different values of activity from the preparation of the phantom up to the last acquisition are also shown. Acquisitions were stopped when the dead time became negligible.

SPECT-TC acquisition time [days]	Volume [ml]	Activity [MBq]	Dead time index DT [%]
0	Sphere 1 : 11,5	150	26
	Sphere 2 : 5,6	75	
	Sphere 3 : 1,1	15	
	Cylinder : 130	1710	
20	Sphere 1 : 11,5	25	5
	Sphere 2 : 5,6	12	
	Sphere 3 : 1,1	2,5	
	Cylinder : 130	280	
40	Sphere 1 : 11,5	5	0,5
	Sphere 2 : 5,6	2,5	
	Sphere 3 : 1,1	0,5	
	Cylinder : 130	55	

Table 1: Volumes and correspondent activities inside the NEMA phantom at the preparation time and after 20 and 40 days, when the dead time became negligible.

The absolute calibration factor K was calculated on the larger volume (cylinder) of the phantom to avoid PVE effects and in the last acquisition day, to be far from dead time count loss. In Figure 2 the sagittal view of the NEMA PET phantom is reported: cylinder and spheres are visible.
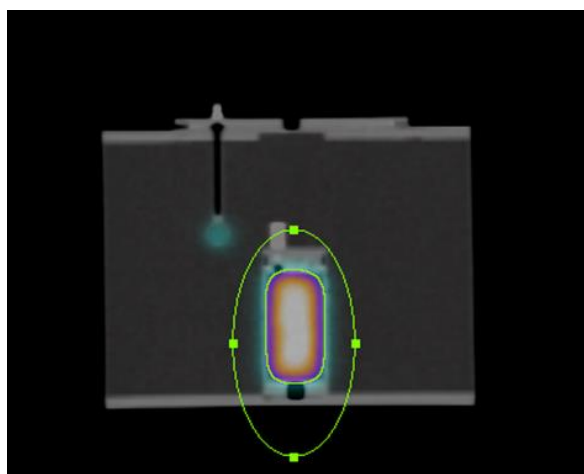
Figure 2 Sagittal view of the NEMA PET Phantom: the ^{131}I activity is visible inside the cylinder and the spheres.

Partial Volume Effect (PVE) curves were obtained on the spheres volumes (10.7cc, 5.44cc and 1.2cc) while for the cylinder (130 cc) the volume is large enough to avoid partial volume effects. The analysis was performed on the last SPECT-TC acquisition to be far from dead time effects. The PVE ratio was plotted as a function of the volume (spheres and cylinder are reported). The trend is reported for the 3 detector radius (25, 28, 33 cm) and is similar to literature data as well as the fitting curves. The curves were employed to calculate, from the volume of the lesion, the corresponding PVE correction factor.

Dead time correction curve was evaluated on the cylinder volume. The curve that correlates the DT coefficient to the K_{DT} correction factor was obtained.

Verification of the ^{131}I SPECT-TC calibration

To verify the ^{131}I SPECT-TC calibration the NEMA PET phantom was set-up a second time: spheres and cylinder were filled with a known activity of liquid ^{131}I (10,11 MBq/ml) and surrounded by water. 4 SPECT-TC acquisitions were performed (same acquisition protocol used for the calibration). The 4 acquisitions were analysed to obtain the activity into the volumes with the formula [1]. The absolute calculated activities [MBq] were compared to the theoretical values. By fitting the Time-Activity curves, the mean dose for each VOIs was calculated with the formula [2]

and compared to the theoretical value. Percentage dose differences were calculated for activities and dose values to estimate the accuracy of the dosimetric method.

Patient ^{131}I lesion dosimetry

After the calibration of the SPECT-TC system, the dosimetric protocol was applied to patients hospitalized for the therapeutic administration of ^{131}I at Nuclear Medicine Department. After the radioiodine administration, the first SPECT-TC acquisition was performed within 4-5 h (patient was encouraged to void bladder before the scan). The following SPECT-TC acquisitions were performed at 24, 72 and 96 h post administration.

A group of 6 metastatic thyroid patients was considered (3 F, 3 M, age $41 \div 71.4$ year, histopathology % papillary, % follicular). The ^{131}I activity was administered from 20xx to 201yy (7.1 MBq [$3.7 \div 11.2$]). The value of activity [MBq] for each lesion of the patient was segmented on the SPECT-CT reconstructed images by means of the contouring software (Volumetrix @Siemens on the e-soft workstation). The lesions were contoured on CT basis, taking into account the uptake (a threshold segmentation method was used on the counts image). This process is necessary for each SPECT-TC acquisition and it is extremely time-consuming and can be affected by operator interpretation and errors. The contouring must be performed on the all 4 SPECT-TC maintaining the lesion VOIs equal. To calculate the dose with the standard method the counts data of each VOIs were entered on a dedicated electronic sheet that calculates the activity. The fit of the time-activity curve was performed with a external software (@LabFit) to calculate the mean dose to the lesion.

[131]I Lesion dosimetry with a 3D in-house dedicated software

An in-house software has been developed (®MatLab) with the aim to become the dosimetric calculation process more automatized and standardized. The intent was to process the SPECT-CT images automatically. The iterative (IT_SCAC) SPECT reconstructed images were imported on the MatLab workspace. The SPECT count matrix was imported and the registration with the CT was achieved considering that the two matrices have the same sagittal heights, and the transversal images have the same centre coordinates. For these reasons, the cranio-caudal CT scan must be always equal to the SPECT emissive scan. The voxel size of the SPECT image was fixed (4.8 mm) and the voxel size of the CT was adapted to have the same number of rows and columns of the SPECT matrix, considering that after the registration the real dimensions of the 3D images are the same. The SPECT-TC are visualized in the transversal, longitudinal and sagittal planes (Fig. 3). A colormap predefined in MatLab was applied, subdivided in 1000 colour shades, and the windowing

can be modified to identify the lesions better. Then, different sections of interest are identified on the z-plane to be analysed. To define the lesion Volume of Interest (VOIs) three different segmentation methods are available: free-hand manual, 2D single slice threshold and 3D threshold. The more useful is the 3D threshold method where the VOI is obtained as a percentage of the maximum in the region of the lesion. This is the first stage of the method, represented in Fig. 4. Secondly, all the slices belonging to the chosen lesion are analysed with the possibility to change the contour of the tumor if some errors occurred, Fig. 5.
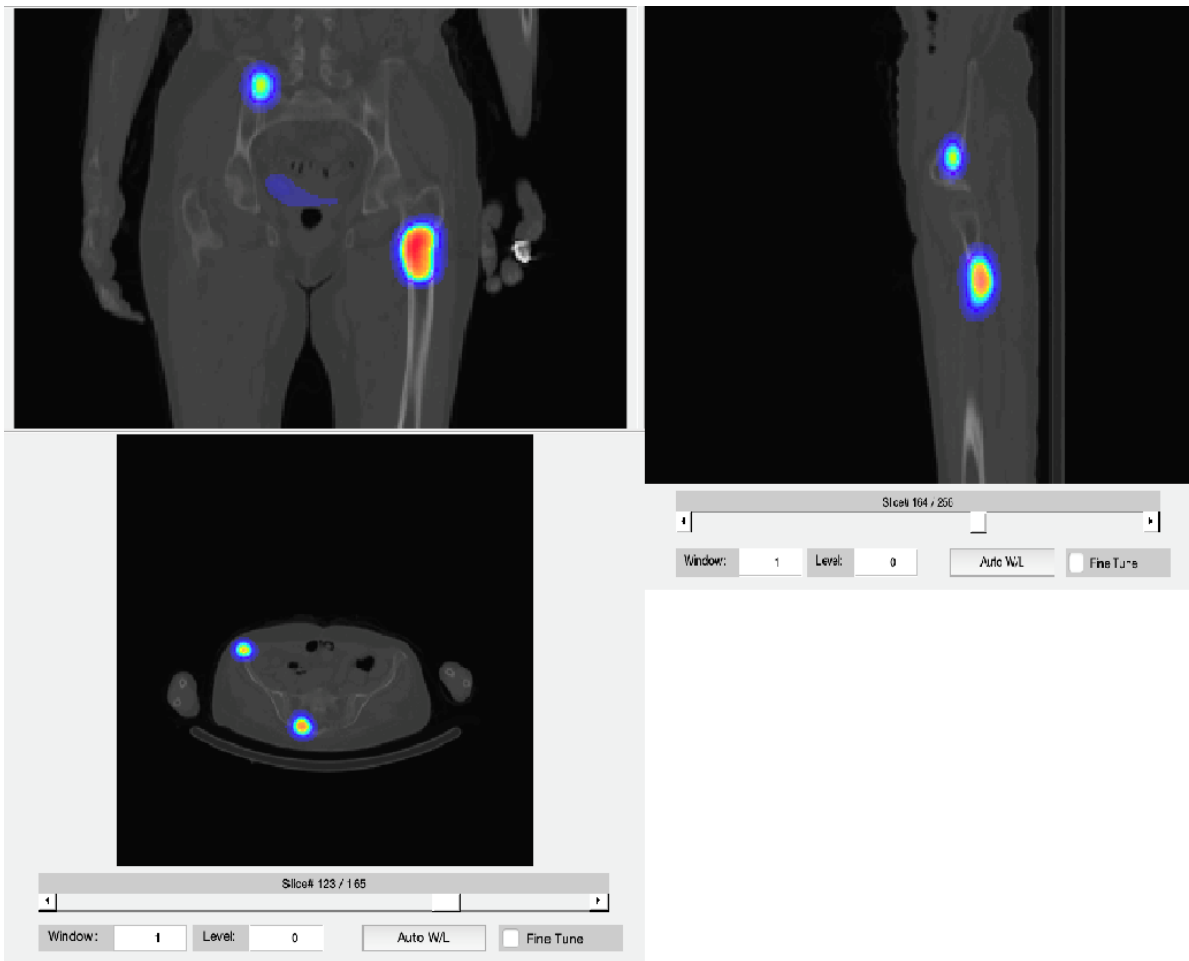

Figure 3: First stage of the 3D threshold method, changing the value of the threshold the corresponding volume of the lesion is visualized.
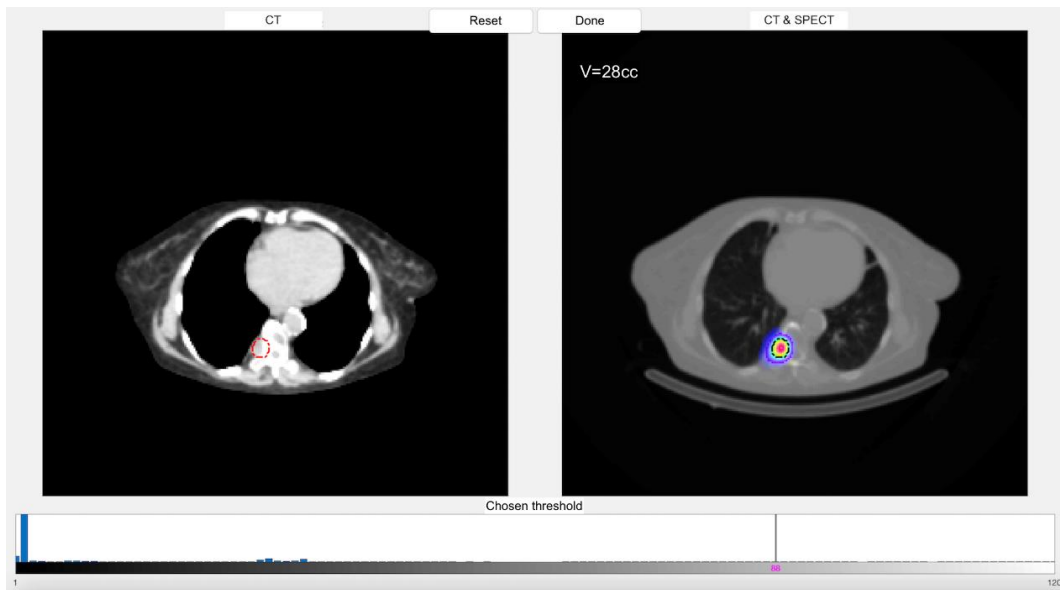
Figure 4: First stage of the 3D threshold method, changing the value of the threshold the corresponding volume of the lesion is visualized.
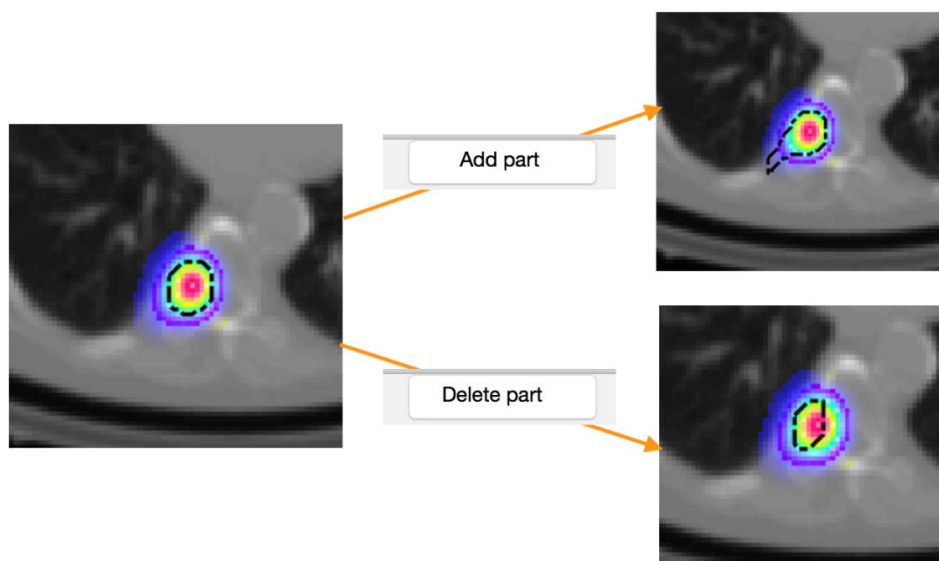

Figure 5: Second stage of the 3D method, all the slices of the lesion are analysed and it contour can be modified.

To apply this segmentation method the lesion volume must be known. For this reason, each tumor lesion is a priori analysed on the processing Siemens workstation (e.soft) and the volume of the metastasis is defined on SPECT and CT basis. Once the volume is set, this value is applied to the 3D MatLab tool, that automatically chooses the threshold value to obtain the exact value of volume (ml). The operator draws the lesion VOI only on one SPECT-TC (usually the second or the third

acquisition, where the lesions are more visible, due to the higher uptake). The MatLab code automatically draws the same VOIs on the other 3 available SPECT-TC. This is achieved in an automatized manner: the software changes the threshold to maintain the volume of the VOI equal in all the 4 SPECT-TC acquisitions. In case of particular geometric shape or location of the lesion a 2D single slice threshold method is always possible, inspecting all the slices of the considered section and correcting manually the volume automatically fixed by the 3D method. Also, the free-hand method of segmentation is available, but the 3D threshold method is preferred because of a more robust standardization and independence from the operator. After the contouring process the total counts inside each lesion, for each SPECT-TC acquisition, are automatically obtained from the counts matrix. To convert the counts to the activity (MBq) using the equation [1] the time per views (s/views), detector radius (25, 28 or 33 cm) and the mean dead time (DT) of each SPECT-TC must be taped as input into the software that ask for these values. The activity of each VOIs is than related to the acquisition time (derived automatically from the SPECT-TC header-DICOM). The activity-time curve is obtained for each lesion and plotted. A curve fitting model is performed by choosing between mono or bi-exponential [Activity [MBq] = A*(EXP(B*time(h))-EXP(C*time(h))] and the activity-time curve and the cumulated activity is obtained [MBq · h]. To convert the lesion volume into a mass (g) the HU lesion value is automatically obtained from the CT image and converted in mass with the calibration curve. Then, the mean dose is calculated with the equation [2].

Validation of the 3D in-house dosimetric software

Phantom acquisition As reported the SPECT-TC calibration was verified with a ^{131}I phantom acquisition: activity and dose into the spheres and cylinder were at first calculated with the standard method (electronic sheet). The 4 SPECT-TC were than analysed also with the 3D dosimetric software (a mono-exponential fit was chosen due to only physical decay). The theoretical activity values, as well as the doses, were compared to the calculated results both with standard and with 3D software ones.

Patients acquisition Also for the 6 patients the same verification was performed. The lesion dosimetry obtained with standard method was compared to results obtained by analysing the SPECT-TC with 3D software (in this case the bi-exponential fit was employed to take into account also the biological discharge). The results are shown in the following tables.

Results

Absolute calibration

The absolute calibration factor (CF), converting counts to MBq was $CF = 4 \cdot 10^{-5} \frac{counts}{MBq}$.

Partial Volume Effects

Partial volume effect curves are reported in Figure 6 for the 3 different circular acquisition radius values. The fit $f(PVE) = a + b \exp(c\ volume)$ is reported in Table 2. These curves were applied to obtain the PVE correction factor when phantom verification and lesion dosimetry are performed.

$f(PVE) = a + b \exp(c\ volume)$			
Circular Detector Radius (cm)	Fit Coefficient a	Fit Coefficient b	Fit Coefficient c
25	98,54	-109,4	-0,1638
28	99,5	-107,6	-0,1430
33	99,58	-106,3	-0,1067

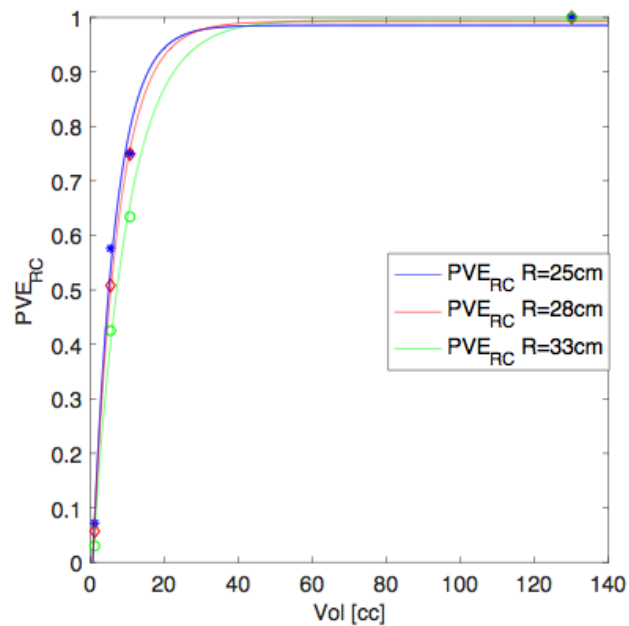Table 2: Coefficients for the fitting curve of the PVE coefficient.

Figure 6: PVE coefficient (dots) are reported as a function of the volume (XXX ml sphere e 130 ml cylinder). 3 different detector radius value were analysed. Curve fit (lines) are also reported.

Dead time correction

The DT index (mean value into the all SPECT-TC views) are reported and the corresponding K_{DT} factor is also shown in Table 3:

DT index [%]	K_{DT}
1	1,0013
2	1,0020
3	1,0033
5	1,0073
8	1,0172
13	1,0438
17	1,0741
22	1,1235
26	1,1720
$K_{DT} = $ a·DT^2+b	

Table 3: K_{DT} obtained in function of the DT indexes detected by the SPECT-TC device.

The K_{DT} data are plotted in Fig. 7 as a function of the DT values (dots) and the parabolic fit $K_{DT} = $ a·DT^2+b is shown (line). The strong relationship between DT and K_{DT} is evident and it is confirmed that the DT index reported on the acquisition Siemens workstation is related to the dead time correction factor K_{DT}. The fit was employed from the DT mean value of the SPECT-TC to obtain the corresponding K_{DT} value in the lesion dosimetry. This dead time correction method is a simplified method. The best solution would be to correct each SPECT-CT view for the corresponding dead time values. This is possible only modifying the raw data during the acquisition because the DT indexes are displayed just in the time of the acquisition process. This solution is not feasible without access to the raw data that was at the moment not possible. For these reasons, the mean value was chosen as reference.
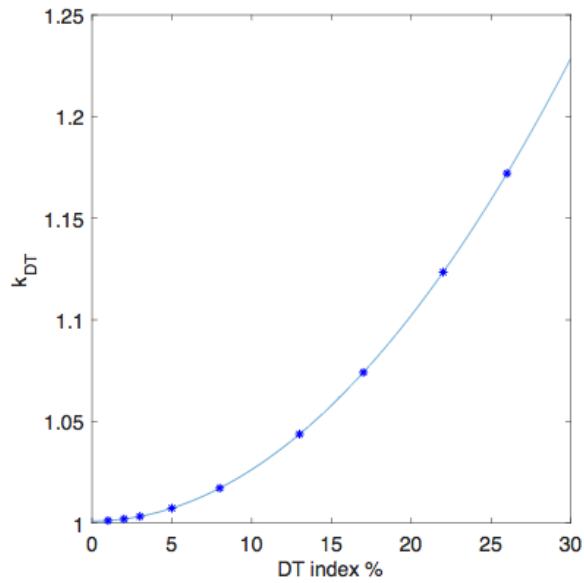
Figure 7: Fitting curve for the K_{DT} coefficient in function of DT index, with the empirical function in Eq. 5.

Activity - Time curve

A typical activity-time curve both for the cylinder (where only physical decay is present) and for a lesion are reported in Figs 8-9. The first point for lesions is set at zero and the second is in the increasing phase of the uptake, while the following points are in the decreasing phase. The coefficients of the fit curve: Activity [MBq] = A*(EXP(B*time(h))-EXP(C*time(h))) referred to the lesion in example is reported in Tab. 4.
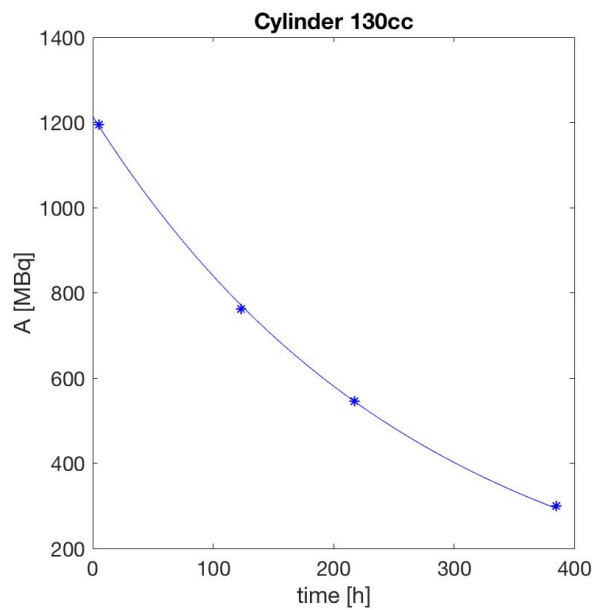

Figure 8: Activity curve for the cylinder inside the water phantom, only physical decay present.
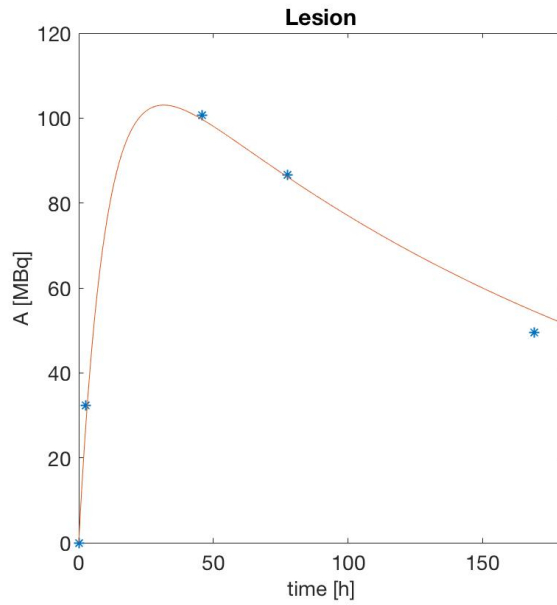
Figure 9: Example of Lesion-Activity curve for a lesion inside a real patient.

Time - Activity Curve		
A	B	C
-127	-0,107	-5,6e-3
Area under the curve [MBq · h] = 21212		

Table 4: Example of coefficients for the Time-Activity biexponential curve, Activity [MBq] = A*(EXP(B*time(h))-EXP(C*time(h))), typical of a lesion.

Lesion mass

The lesion mass is obtained from the mean Hounsfield Unit (HU) into the lesion. A calibration curve was obtained with a CT-Phantom, to convert HU in mass density (g/cm^3). The phantom was acquired on the SPECT-TC system and the different well-known density materials were related to the HU. The values are reported in Table 5 as well as the fitting curve is shown in Figure 10 (two different curves where employed when HU is < 1 or > 1). From the density g/cm^3 the lesion mass is obtained multiplying the density to the volume.

HU	g/cm³
-986	0.00005
-709	0.281
-531	0.463
-77	0.937
-42	0.957
1	1
29	1.049
93	1.077
220	1.105
224	1.06
431	1.275
779	1.467
1161	1.691
4000	2.98
HU < 1	g/cm³ = 0.001 HU +1.0044
HU > 1	g/cm³ = 0.00005 HU +1.0661

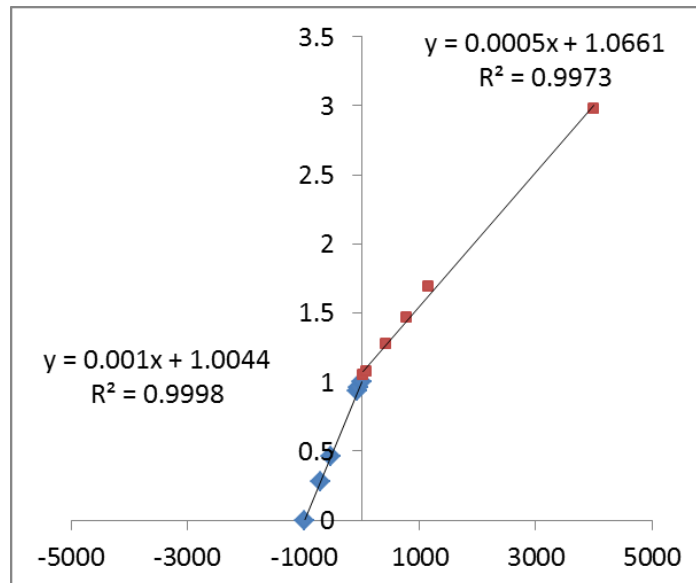Table 6: Relation between the density and the HU of different materials.

Figure 10: Fitting curve for the relation density-HU for two different HU range of values (HU<1 or HU>1).

Lesion Mean Dose

The lesion mean dose is then obtained with the Equation [2] where the S factor is calculated from the lesion mass with the above-reported equations.

$$\text{Dose [mGy]} = S \text{ [mGy/MBq h]} \times \tilde{A} \text{ [MBq} \cdot \text{h]}$$

For example, for the lesion reported in Fig. 7, the mean dose was obtained equal to 84,5 Gy, all the data of volume and mass are reported in Tab. 7.

Lesion volume (cm^3)	28,12
Lesion density (g/cm^3)	1,08
Lesion mass (g)	30,26
S (mGy/MBq h)	3,98
Cumulated activity [MBq h]	21212
Mean lesion Dose = 84,5 Gy	

Table 7: Calculated data for the same lesion of Fig. 9, with at the end the value of the mean dose to the lesion.

Validation of the 3D in-house dosimetric software

Phantom dosimetry

In Table 8 results of volumes (obtained with the threshold 3D segmentation method), the cumulated activities and the mean doses in the verification phantom are reported. The theoretical expected value is compared to the calculated value obtained analysing the phantom acquisitions with the 3D software (MatLab). The percentage difference is shown in brackets.

VOI	Volume [cm^3]		Cumulated activity [MBq h]		Mean Dose [Gy]	
	Theoretical	Calculated	Theoretical	Calculated	Theoretical	Calculated
Cylinder	130.0	130.3 (0%)	365923	329462 (-10%)	358	318 (11%)
Sphere 1	11.5	11.5 (0%)	28073	23613 (-16 %)	311	328 (5%)
Sphere 2	5.6	5.6 (0%)	15912	12910 (-19 %)	323	259 (20 %)
Sphere 3	2.7	2.6 (-4%)	7158	7653 (+7%)	316	333 (+5%)
Sphere 4	1.1	0.5 (-45%)	3203	6673 (+100%)	326	671 (+105%)

Table 8: Results from the phantom verification in terms of volume, cumulated activity and mean dose to the lesion. Calculated data (obtained with the in-house software) are compared with the theoretical value.

The higher variations were found for the smallest sphere (Sphere 4: 1.1 cc) where the 3D software overestimated the dose due to the lower volume calculated by the 3D software when the VOI was contoured. This dimension is below the spatial resolution and for this reason lesions smaller than 2.5 cm^3 were not evaluated.

In Figure 11 the theoretical activity decay curve inside the cylinder is reported and compared to the activity curve data obtained by the 3D MatLab software (a monoexponential fit was applied).
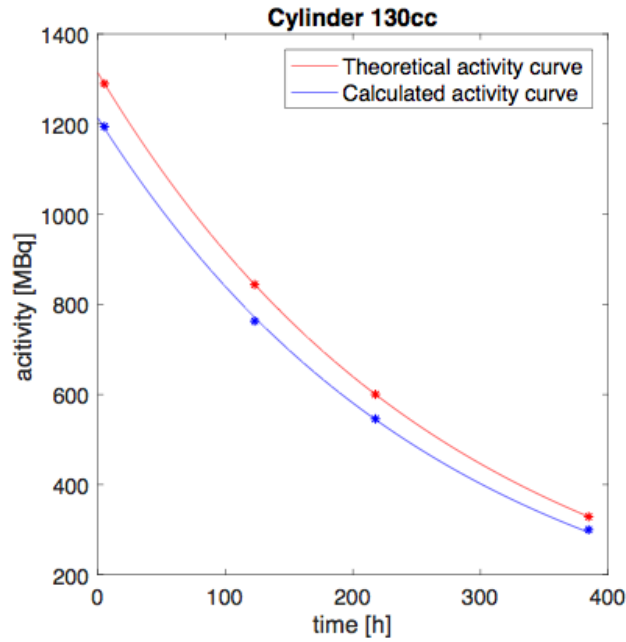
Figure 11: Theoretical activity decay curve (red line) inside the 130 ml cylinder compared to the activity curve data obtained by the 3D MatLab software (blue line) The overall difference in the cumulated activity was about 11 % (see Table 8).

Patients dosimetry

In the following Tables 9-14, results from lesion dosimetry of patients are reported. Volumes, cumulated activities and mean doses to the lesions calculated with standard method were compared to results obtained with 3D software. A whole-body image is also shown as well as lesion type. In brackets the percentage difference is reported (the standard method results were set as a reference value).

Patient # 1						
Female, 42 years, Administered activity = 5552 MBq date 24/10/2016						

WB ANTERIORE
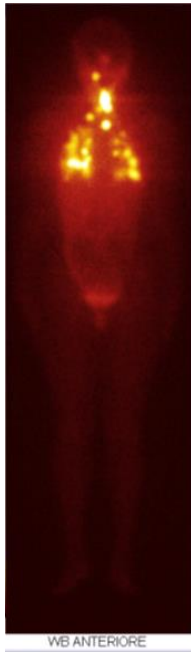
Lesion	Volume [cm³]		Cumulated activity [MBq h]		Mean Dose [Gy]	
	Theo	Calc	Theo	Calc	Theo	Calc
Lymphnod	6.15	6.17 (0%)	9114	8502 (-7%)	160	150 (-7%)
Lymphnod	4.36	4.33 (-1%)	10431	10598 (2%)	267	275 (3%)
Lymphnod	7.81	7.94 (2%)	898	840 (-7%)	12	12 (0%)
Lung	7.28	7.27 (0%)	4508	4236 (-6%)	115	121 (5%)
Lung	5.2	5.2 (0%)	1259	1219 (-3%)	56	55 (-2%)
Lung	5.69	5.55 (-3%)	1596	1541 (-4%)	76	67 (-13%)
Lung	18.32	18.41 (0%)	3081	3108 (1%)	45	52 (13%)
Lung	7.82	7.82 (0%)	1515	1419 (-7%)	80	75 (-7%)

Table 9: Results for patient #1

Patient # 2

Female, 71 years, Administered activity = 7209 MBq   date 30/01/2017
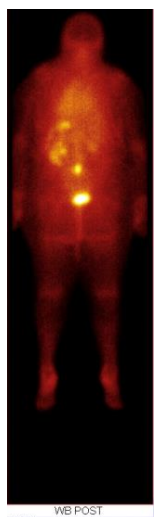
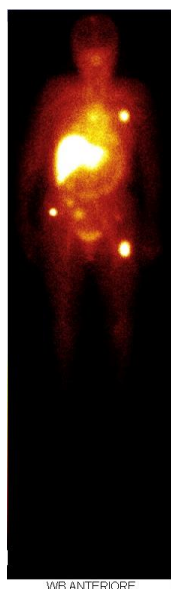| Lesion	Volume [cm³]		Cumulated activity [MBq h]		Mean Dose [Gy]	
	Theo	Calc	Theo	Calc	Theo	Calc
Vertebra	14	13.8 (-1%)	3917	4057 (3%)	25.5	27.8 (8%)

Table 10: Results for patient #2

Patient # 3

Female, 58 years, Administered activity = 3716 MBq   date 19/12/2016

WB ANTERIORE

Lesion	Volume [cm³]		Cumulated activity [MBq h]		Mean Dose [Gy]	
	Theo	Calc	Theo	Calc	Theo	Calc
Bone	7.7	7.7 (0%)	12717	12678 (0%)	174	177 (2%)
Bone	3.95	3.95 (0%)	3993	4001 (0%)	103	105 (2%)
Bone	9.5	9.5 (0%)	7159	7147 (0%)	82	81 (-1%)
Bone	5.1	4.9 (-4%)	2423	2420 (0%)	45	45 (0%)
Bone	4.2	4.22 (0%)	4142	4118 (1%)	101	105 (4%)
Bone	4.9	4.82 (2%)	3323	3231 (3%)	73	70 (4%)

Table 11: Results for patient #3

	Patient # 4						
Female, 63 years, Administered activity = 5596 MBq date 13/03/2017							

WB ANT

Lesion	Volume [cm³]		Cumulated activity [MBq h]		Mean Dose [Gy]	
	Theo	Calc	Theo	Calc	Theo	Calc
Bone	193.5	193.7 (0%)	63625	64735 (2%)	40	40 (0%)
Bone	11.33	11.29 (0%)	12807	13579 (6%)	121	129 (6%)
Bone	85	84 (-1%)	92690	95184 (3%)	128	131 (2%)
Bone	6.7	6.7 (0%)	1425	1671 (15%)	21	26 (19%)
Bone	5.5	5.5 (0%)	5059	4916 (-3%)	101	96 (-5%)

Table 12: Results for patient #4

<table>
<tr><td colspan="8" align="center">**Patient # 5**</td></tr>
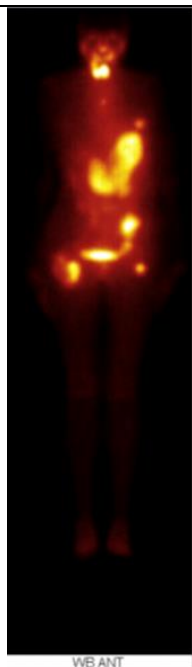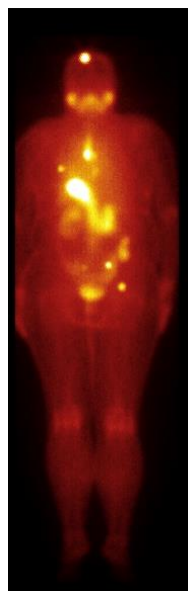<tr><td colspan="8" align="center">Female, (54) years, Administered activity = 5594 MBq   date 18/06/2018</td></tr>
</table>

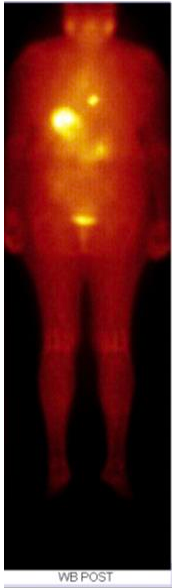| Lesion	Volume [cm³]		Cumulated activity [MBq h]		Mean Dose [Gy]	
	Theo	Calc	Theo	Calc	Theo	Calc
Bone	9	9 (0%)	7167	7157 (0%)	74	78 (5%)
Bone	10.4	10.6 (2%)	1260	1279 (1%)	13	13 (0%)
Bone	6.1	6.25 (2%)	1280	1269 (-1%)	25	24 (-4%)
Bone	10.1	10.2 (1%)	1789	1801 (1%)	19	18.7 (-2%)
Bone	10	9.9 (0%)	1283	1285 (0%)	14	14 (0%)

Table 13: Results for patient #5

Patient # 6

Female, 71 years,

Administered activity 1st treatment= 9286 MBq   date 29/05/2017

2nd treatment= 11145 MBq date 30/04/2018

WB POST

Lesion	Volume [cm³]		Cumulated activity [MBq h]		Mean Dose [Gy]	
	Theo	Calc	Theo	Calc	Theo	Calc
1st treat	29.3	28.1 (-4%)	22457	21212 (-6%)	85	84 (-1%)
2nd treat	20.3	20.9 (3%)	7542	8024 (6%)	41	42 (2%)

Table 14: Results for patient #6

Statistics on phantom and patient results

The validation of the 3D MatLab software with the previously used standard method gives good results in the case of the phantom (percentage dose difference mean ± 1dev.st 6.7 ± 14.0 %) excluding the last sphere present due to its volume, smaller than the resolution of the SPECT device. Also considering the results for patient lesion dosimetry, a good agreement in terms of cumulated activity (percentage difference mean ± 1dev.st 0.3 ± 4.7 %) and absolute dose (percentage difference mean ± 1dev.st -1.0 ± 6.4 %) was found. Box-plot diagram for the theoretical and calculated dose and cumulated activity for all the patients of Tables 9-4 are reported in Figure 12 (a) and (b).
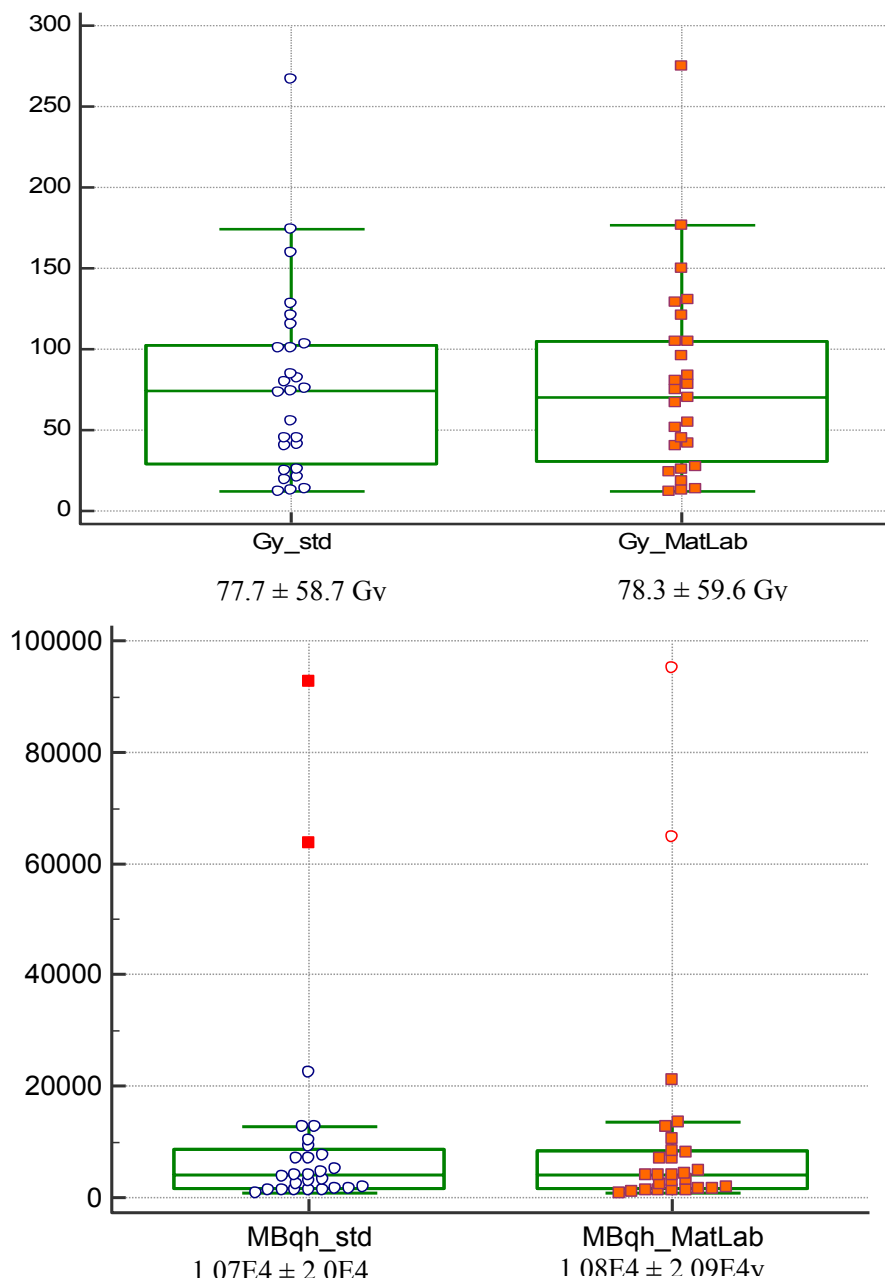

Figure.12 Box Plot for dose results (a) and for cumulated activity (b)

T-test for paired samples was applied both for dose and cumulated activity comparisons on patients and phantom results. *p-values* are reported in Table 15 and do not show statistical differences.

Patient dosimetry	
Dose (p-value)	0.4758
Cumulated Activity (p-value)	0.4019
Phantom dosimetry	
Dose (p-value)	0.4563
Cumulated Activity (p-value)	0.2959

Table 15: Statistic tests to compare dose and activity results obtained with standard and Matlab dose calculation methods.

Discussion

At present, commercial software for internal dosimetry do not take into consideration ^{131}I patients and there are not open source versions available. In literature, some studies on internal dosimetry are present but designed only for PET images [13]. The importance to standardize the dosimetric calculation approach leads to the development of in-house software, able to provide the values of dose to the lesions in metastatic thyroid patients, treated with ^{131}I for metastatic thyroid cancer.

The main aim of the new software is to minimize the operator-dependence, processing the SPECT-CT images automatically. Most of the efforts were devoted to the registration of the SPECT reconstructed image and the correspondent CT. The software implements during the calculation the gamma camera parameters, obtained by a calibration process. One of the critical points of the process is the contouring of each lesion on the 4 different acquisition: it should be well defined the volume of the lesion in the initial clinical phase to obtain precise results. In case of difficult identification of the lesion, the error in the volume definition will affect considerably the dose calculation. A strong synergy with the medical staff is fundamental to avoid incorrect values of dose to the tumour. Once the lesion volume is well identified, the 3D software automatically contour on the 4 SPECT-TC acquisitions the lesion, obtaining counts converted into cumulated activity and finally in mean dose.

The curve fitting process of the activity-time function is another crucial point of the study, due to its fundamental role in the calculation of the final mean dose to the tumor. In this version of the software, the possibility to try different fit models allows a more tailored choice of the activity curve function.

The validation of the 3D MatLab dose software was performed on phantom and patients acquisitions to test the robustness of the dose calculation tool. The good agreement both in terms of cumulated activity and dose confirms the reliability of the in-house software that will be employed for the patient dose calculation.

At present, only a few numbers of patients were available for the validation, but the statistic could be increased in future. Due to the high flexibility of the 3Dsoftware it could be rapidly adapted to other isotopes (i.e. Lu177) but new calibration factors will be needed and given as input to the dose calculation tool.

Conclusion

The present paper demonstrates the efficacy of an in-house dosimetry software, designed to calculate the dose to the lesion in case of metastatic thyroid patients treated with high ^{131}I activity. To validate the robustness of the software, a comparison in terms of dose and cumulated activity was performed both on a phantom and on six real patients with reference results from the standard dose calculation, giving a good agreement. The employment of the dosimetry software could be a promising alternative to dose calculation, granting a standardization of the procedure with limited operator-dependence.

Reference

[1] Willowson et al., *Quantitative SPECT reconstruction using CT-derived corrections*, PMB, 2008, 53:3099-3112, doi: 10.1088/0031-9155/53/12/002

[2] Loevinger R, Budinger T, Watson E, *MIRD Primer for Absorbed Dose Calculations*, Society of Nuclear Medicine, 1988.

[3] DewarajaYK et al., MIRD pamphlet No. 23: *Quantitative SPECT for patient-specific 3-dimensional dosimetry in internal radionuclide therapy*, J Nucl Med, 2012, 53(8):1310-25, doi: 10.2967/jnumed.111.100123.

[4] Lee JJ et al, *Maximal safe dose of I-131 after failure of standard fixed dose therapy in patients with differentiated thyroid carcinoma,* Ann Nucl Med, 2008, 22:727-734, doi: 10.1007/s12149-007-0179-8.

[5] Giostra A1, Richetta E, Pasquino M, Miranti A, Cutaia C, Brusasco G, Pellerito RE, Stasi M., *Red marrow and blood dosimetry in (131) I treatment of metastatic thyroid carcinoma: pre-treatment versus in-therapy results*, Phys Med Biol., 2016, 61(11):4316-26, doi: 10.1088/0031-9155/61/11/4316.

[6] Miranti A., Giostra A., Richetta E., Gino E., Pellerito RE., Stasi M*., Comparison of mathematical models for red marrow and blood absorbed dose estimation in the radioiodine treatment of advanced differentiated thyroid carcinoma.,* 2015, 60(3):1141-57, doi: 10.1088/0031-9155/60/3/1141.

[7] Maxon H.R., *Quantitative radioiodine therapy in the treatment of differentiated thyroid cancer*, QJ Nucl. Med 1999; 43(4):313-23.

[8] Dorn R. et al., *Dosimetry-guided radioactive Iodine treatment in patients with metastatic differentiated thyroid cancer: largest safe dose using a risk-adapted approach*, J Nucl Med, 2003, 44(3):451-6.

[9] Deandreis D, Rubino C, Tala H, Leboulleux S, Terroir M, Baudin E, et al. *Comparison of empiric versus whole body/blood clearance dosimetry-based approach to radioactive iodine treatment in patients with metastases from differentiated thyroid cancer*, J Nucl Med, 2017, 58(5):717-722. doi: 10.2967/jnumed.116.179606.

[10] Klubo-Gwiezdzinska J. et al, *Efficacy of dosimetric versus empiric prescribed activity of 131I for therapy of differentiated thyroid cancer*, J Clin Endocrinol Metab, 2011, 96(10):3217-25. doi: 10.1210/jc.2011-0494.

[11] Nagarajah J. et al., *Iodine Symporter Targeting with 124I/131I Theranostic*, J Nucl Med, 2017, 58(Suppl 2):34S-38S. doi: 10.2967/jnumed.116.186866.

[12] Mandel S.J., *Radioactive iodine and the salivary glands,* Thyroid. 2003, 13(3):265-71.

[13] Sgouros G. et al., *Patient-specific dosimetry for 131I thyroid cancer therapy using 124I PET and 3-dimensional-internal dosimetry (3D-ID) software,* J Nucl Med, 2004, 45(8):1366-72.